

# X-ray Study of Hot Gas in Groups of Galaxies

Umeyo Morita

*Department of Physics, Tokyo Metropolitan University  
Minami-Osawa 1-1, Hachioji, Tokyo 192-0397, Japan*

Thesis submitted to Tokyo Metropolitan University  
for the Degree of Doctor of Science (Physics)  
November 2006



## Abstract

We present results of X-ray observations of two groups of galaxies, a spiral-only group HCG 80 ( $z = 0.03$ ), observed with Chandra, and an elliptical dominant group HCG 62 ( $z = 0.01$ ), studied with Chandra and XMM-Newton. For HCG 80, we searched for diffuse X-ray emission from the intragroup medium (IGM); however, no significant emission was detected. We placed a tight upper limit on the X-ray luminosity of the diffuse gas as  $L_X < 6 \times 10^{40}$  erg s $^{-1}$ , which is about a hundred times lower than the typical luminosity of elliptical dominant groups. On the other hand, X-ray emission from three of the four member galaxies were detected the high angular resolution ( $0.5''$ ) of Chandra. In particular, we discovered huge halo emission from HCG 80a that extends on a scale of  $\sim 30$  kpc perpendicular to the galactic disk, whose X-ray temperature and luminosity were measured to be  $\sim 0.6$  keV and  $\sim 4 \times 10^{40}$  erg s $^{-1}$  in the 0.5–2 keV band, respectively. It is most likely to be an outflow powered by intense starburst activity.

In the elliptical dominant group HCG 62, there are two X-ray cavities at about  $30''$  northeast and  $20''$  southwest of the central galaxy in the Chandra image. The energy spectrum shows no significant change in the cavity compared with that in the surrounding region. We studied radial distributions of temperature and metal abundance with joint spectral fit for the Chandra and XMM-Newton data, and two temperatures were required in the inner  $r < 2'$  (35 kpc) region. The sharp drop of temperature at  $r \sim 5'$  implies the gravitational mass density even lower than the gas density, suggesting the gas may not be in hydrostatic equilibrium. Fe and Si abundances are 1–2 solar at the center and drop to about 0.1 solar at  $r \sim 10'$ . O abundance is less than 0.5 solar and shows a flatter profile. Observed metal distribution supports the view that iron and silicon are produced by type Ia supernova in the central galaxy, while galactic winds by type II supernova have caused wider distribution of oxygen. The supporting mechanism of the cavity is discussed. Pressure for the sum of electrons and magnetic field is too low to displace the hot group gas, and the required pressure due to high energy protons are nearly 700 times higher than the electron pressure. The upper limit of the X-ray luminosity of the central active galactic nucleus is 1000 times lower than the necessary energy supply to support the cavity. This leaves the origin of the cavities as a puzzle, and we discuss other possible origins.

It was confirmed that there was no significant diffuse X-ray emission in the spiral-only group HCG 80, in contrast to the high luminosity ( $\sim 4 \times 10^{42}$  erg s $^{-1}$ ) of the elliptical dominant group HCG 62. These two systems are considered to be in a very different stage of the group formation process: HCG 80 in a early stage and HCG 62 in an evolved phase. The group environment would cause enhanced starformation activity through galaxy-galaxy interactions, as observed in HCG 80. The metallicity structure in HCG 62 further indicates that a significant fraction of metals are supplied by the central elliptical galaxy. We also found in HCG 62 that

the cavity formation is strongly related with the activity of the central elliptical galaxy, whose precise mechanism is unclear yet. Therefore, elliptical galaxies in the center of groups play an important role in supplying energy and heavy elements in the central region of the groups.

# CONTENTS

<b>1</b>	<b>Introduction</b>	<b>5</b>
<b>2</b>	<b>Review</b>	<b>9</b>
2.1	Group of Galaxies . . . . .	9
2.2	Galaxies . . . . .	10
2.2.1	Classifications of galaxies . . . . .	10
2.2.2	Spiral galaxies . . . . .	11
2.2.3	Elliptical galaxies . . . . .	12
2.2.4	cD galaxies . . . . .	12
2.3	X-ray Gas in Groups . . . . .	12
2.3.1	Existence of intragroup medium . . . . .	14
2.3.2	Chemical properties . . . . .	16
2.3.3	$L_X$ - $kT$ relation . . . . .	19
2.4	X-ray Emission Other Than Diffuse Hot Gas . . . . .	19
2.4.1	X-ray emission from discrete sources . . . . .	19
2.4.2	Hard X-ray emission . . . . .	20
2.5	Galaxy Interaction . . . . .	22
2.5.1	Starbursts . . . . .	22
2.5.2	Cavities . . . . .	22
2.6	X-ray Gas Distribution . . . . .	25
2.7	Mass Distribution . . . . .	26
2.8	HCG 80 . . . . .	27
2.9	HCG 62 . . . . .	27
<b>3</b>	<b>Instrumentation</b>	<b>29</b>
3.1	Chandra X-ray Observatory . . . . .	29
3.1.1	Overview of the Chandra Satellite . . . . .	29
3.1.2	High Resolulusion Mirror Assembly (HRMA) . . . . .	30
3.1.3	Advanced CCD Imaging Spestrometer (ACIS) . . . . .	31
3.2	XMM-Newton . . . . .	32

3.2.1	Overview of the XMM-Newton Satellite . . . . .	32
3.2.2	X-ray telescope . . . . .	33
3.2.3	European Photon Imaging Camera (EPIC) . . . . .	35
3.3	Compare Chandra with XMM-Newton . . . . .	36
<b>4</b>	<b>HCG 80</b>	<b>39</b>
4.1	Chandra Observation of HCG 80 . . . . .	39
4.2	Data Reduction . . . . .	39
4.3	Source Detection in the ACIS-S3 Field . . . . .	41
4.4	X-Ray Morphologies of Member Galaxies . . . . .	42
4.4.1	HCG 80a . . . . .	42
4.4.2	HCG 80b . . . . .	45
4.5	Hardness Ratio Analysis . . . . .	46
4.6	X-Ray Spectra of Member Galaxies . . . . .	47
4.7	Constraints on the Hot Diffuse Emission . . . . .	49
4.8	Nucluous/Starburst Activities of Member Galaxies . . . . .	50
4.8.1	$L_X$ - $L_B$ relations . . . . .	50
4.8.2	Starburst Activity in HCG 80a . . . . .	51
4.9	Diffuse Hot Gas in HCG 80 . . . . .	54
<b>5</b>	<b>HCG 62</b>	<b>57</b>
5.1	Chandra and XMM-Newton Observations of HCG62 . . . . .	57
5.2	Data Reduction . . . . .	57
5.2.1	Chandra . . . . .	57
5.2.2	XMM-Newton . . . . .	59
5.2.3	Background estimation . . . . .	59
5.3	X-ray Image . . . . .	61
5.3.1	Chandra image . . . . .	61
5.3.2	XMM-Newton image . . . . .	63
5.3.3	Surface brightness profile . . . . .	64
5.4	X-ray Cavity . . . . .	67
5.4.1	Flux depression & temperature map . . . . .	67
5.4.2	Spectral comparison between cavity & non-cavity regions . . . . .	69
5.4.3	Hollow sphere model . . . . .	71
5.5	Radial Profiles of Temperature & Abundance . . . . .	73
5.5.1	Consistency between Chandra & XMM-Newton . . . . .	73
5.5.2	Mekal vs APEC model & notes on abundance . . . . .	74
5.5.3	Deprojection analysis . . . . .	75
5.5.4	Temperature profile . . . . .	76

5.5.5	Abundance profile . . . . .	78
5.6	Mass Profiles . . . . .	80
5.6.1	Formulation of two-phase gas . . . . .	80
5.6.2	Dark matter and gas mass . . . . .	83
5.6.3	Stellar mass . . . . .	84
5.7	ICM properties . . . . .	85
5.8	Supporting mechanisms of X-ray cavities . . . . .	87
5.8.1	Characteristics in X-ray, optical, and radio . . . . .	87
5.8.2	Gas pressure & non-thermal pressure . . . . .	88
5.8.3	Time scales . . . . .	89
5.8.4	Energetics . . . . .	90
5.8.5	Difficulties in non-thermal pressure support by jets . . . . .	91
5.8.6	Another supporting mechanism — hot gas clump — . . . . .	92
5.8.7	Another formation scenario — galaxy motion — . . . . .	93
<b>6</b>	<b>Summary and Conclusion</b>	<b>95</b>
6.1	HCG 80 . . . . .	95
6.2	HCG 62 . . . . .	95
6.3	Hot Gas in Groups of Galaxies . . . . .	96
<b>A</b>	<b>Energy spectra for HCG 62</b>	<b>97</b>
A.1	1- $T$ results . . . . .	97
A.2	2- $T$ results . . . . .	99
<b>B</b>	<b>Soft background estimation</b>	<b>101</b>
<b>C</b>	<b>Deprojection</b>	<b>105</b>
<b>D</b>	<b>The ratio of Si abundance</b>	<b>107</b>



# Chapter 1

## Introduction

The majority of galaxies are found to reside in groups of galaxies (Tully 1987), and the intragroup medium may dominate the total baryon density of the local universe (Fukugita et al. 1998). In many cases, the groups are filled with hot ( $0.3 \sim 1.8$  keV), low-density ( $\sim 10^{-3} \text{ cm}^{-3}$ ) gas, and the X-ray emission is extended often beyond the optical extent of the group. The detection of extended X-ray emission has at least shown that a number of groups are gravitationally bound systems. The X-ray hot gas also contains a large amount of metals, so that, it offers important information in examining the process of the metal enrichment over  $10^{10}$  years since the universe has begun.

There are 3 scientific aims in this thesis study, which involves detailed X-ray observations of 2 groups of galaxies, HCG 80 and HCG 62. The first purpose is the detailed X-ray study of a spiral dominant group. The previous survey study from ROSAT showed that the group-wide hot gas is almost exclusively seen in groups which contain at least one elliptical galaxy (§ 2.3). Later, a couple of reports on the detection of extended X-ray emission from spiral-only groups were given, however we need to explore other groups with high sensitivity to establish the origin of the hot gas. For this purpose, using Chandra X-ray Observatory, we observed HCG 80 which is another group consisting of only spiral galaxies. This observation will also show us the activities in individual galaxies in the group environment. The galaxy density is extremely high in compact groups with a typical separation of  $\sim 20$  kpc. Close encounters of galaxies may drive starformation activities and enhance metal production, which eventually leads to the metal enrichment of intergalactic space through outflows of the hot gas. Previous observations suggested a causal link between the starburst activity and the galaxy interactions (Kennicutt 1998). Since in clusters of galaxies the intracluster medium is too bright and direct study of individual galaxies are rather difficult, groups of galaxies give us the best opportunity to look into the activities of galaxies.

The second aim is the detailed study of metal distribution in the intragroup medium. Groups of galaxies can be regarded as a bridge which connects galaxies and clusters of galaxies, and metallicity information about groups is very important to know the injection process from in-

dividual galaxies and to know how intergalactic space has been metal enriched. The observation of metal content in groups was initiated by ASCA, and it is known that a large amount of metals need to be produced in the galaxy formation epoch and the subsequent supernova activities, since the current supply from the stellar mass loss is unable to explain the metal content (Arnaud et al. 1992). The gas temperatures characteristic for groups are cooler ( $\sim 1$  keV) than typical clusters, and the energy spectrum shows many strong emission lines. Detailed study of metallicity distribution in bright group of galaxies will give us important information about the metal production and enrichment processes (§ 2.3).

The third aim is the study of the origin of non-thermal and non-gravitational energy in groups. The observed X-ray luminosities of clusters and groups of galaxies show strong correlation with the gas temperature, whose slope disagrees with the self-similar cluster formation picture. The observed slope for groups is even steeper than those for clusters, implying that the hot gas in groups of galaxies are relatively more heated than in clusters by some non-gravitational processes. This indicates that groups of galaxies are key objects in understanding the problem of non-gravitational heating of the extended hot gas. Another striking gas feature connected with the non-gravitational energy input is the X-ray cavities. These are X-ray holes near the bright central galaxies often overlapping with radio lobes. Clearly, non-thermal pressure is strong enough to displace the hot gas. A detailed X-ray study of cavities and temperature structures in bright groups will give us new insight about the scale and strength of non-thermal energy input in groups and clusters (§ 2.4).

In this thesis, I selected two groups of HCG 80 (§ 2.8) and HCG 62 (§ 2.9). Table 1.1 summarizes their properties, comparing with other well-studied groups of HCG 57 and HCG 16. The groups of galaxies play a connecting role for galaxies and clusters of galaxies in many respects, and can be regarded as the key objects in the hierarchical structure of the universe. The present research will bring us new X-ray features about the groups of galaxies and will significantly raise the importance of their study in understanding the evolution of the universe.

Throughout this thesis,  $\Omega_\Lambda = 1 - \Omega_M = 0.73$  and  $h_{70} \equiv H_0/(70 \text{ km s}^{-1} \text{ Mpc}^{-1}) = 1$  are

Table 1.1: Properties of four well-studied spiral dominant group:  $kT$  indicates approximate temperature when a thermal spectrum is assumed, and  $L_X$  is the bolometric luminosity of the diffuse emission only.

name	$z$	$f_{\text{spiral}}$	$kT$ (keV)	Log $L_X$ (erg/s)
HCG 57	0.0304	0.43	1.1	41.92
HCG 16	0.0131	0.86	0.4	40.74
HCG 80	0.0299	1.00	0.8	41.92
HCG 62	0.0145	0.47	1.0	42.69

assumed. The quoted errors indicate the 90% confidence range, and the solar abundance ratio of Anders & Grevesse (1989) is implied, unless otherwise stated.



# Chapter 2

## Review

### 2.1 Group of Galaxies

Groups of galaxies are smaller systems than clusters of galaxies, with a typical group containing only a few luminous galaxies, and have a scale of  $250 \sim 500$  kpc. They are also mainly identified on optical plates. At present, the hierarchical clustering scenario is widely supported, as it is naturally expected from the cold dark matter model. Also, the fact that the galaxies at redshifts of  $\sim 5$  have been observed, whereas the most distant observed clusters are at  $z \sim 1$ , indicating that the smaller systems have been formed earlier. According to the bottom-up scenario, large-scale structures of the universe have been formed from infinitesimally small density perturbations at the early universe through the gravitational interaction. A number of numerical simulations for the structure formation show hierarchical clustering of the hot gas and dark matter, and indicate that the clusters are formed through subcluster mergers and/or acquisition of groups of galaxies. Groups should thus provide useful probes of structure formation in the universe, yet their physical nature is still highly unclear [see Hickson (1997) and Mulchaey (2000) for reviews].

Hickson (1982) cataloged 100 compact groups (Hickson's Compact Groups; HCGs), which form one of the best studied catalogs among the groups searched by Palomar Observatory Sky Survey red points. A group is called "compact" when there are several galaxies within a limited radius (Hickson 1982), and called "loose" when there are not. According to Hickson (1982), a compact group is defined by the following criteria:  $N \geq 4$ ,  $\theta_N \geq 3\theta_G$ ,  $\bar{\mu}_G < 26.0$ , where  $N$  is the total number of galaxies within 3 mag of the brightest one,  $\bar{\mu}_G$  is the total magnitude of these galaxies per arcsec<sup>2</sup> averaged over the smallest circle (angular diameter  $\theta_G$ ) that contains their geometric centers, and  $\theta_N$  is the angular diameter of the largest concentric circle that contains no other galaxies within this magnitude range or brighter. The radius is about 100 kpc. The short crossing times implied for HCGs suggest either they are chance alignments of unrelated galaxies within looser systems (Mamon 1986; Walke & Mamon 1989) or short-lived ( $\sim 1$  Gyr) bound configurations within loose groups (Diaferio et al. 1994; Governato et al. 1996).

The observation of clusters/groups began in the optical band historically. We can understand

this immediately, since it is defined by the distribution of member galaxies which are identified in the optical band. However, the discovery that many groups are X-ray sources has provided considerable new insight. X-ray observations indicate that about half of all poor groups are luminous X-ray sources. The diffuse X-ray emission can be interpreted in the following way. For example, we assume a group which is concentrated in a sphere of radius  $\sim 250$  kpc with a mass of  $10^{13} M_{\odot}$ . If this system is under hydrostatic equilibrium, the kinetic energy is approximately equal to the gravitational potential energy. This gives an emission in the typical X-ray energy band, if we calculate the temperature corresponding to this energy. X-ray analysis provides a powerful tool to measure the temperature, the metal abundance, and the gravitational mass in groups.

In many cases, the X-ray emission is extended, often beyond the optical extent of the group. The spatial and spectral properties of the X-ray emission suggest the entire volume of a group is filled with hot, low-density ( $\sim 10^{-3} \text{ cm}^{-3}$ ) gas. The derived gas temperatures are in the range  $0.3 \sim 1.8$  keV, which is roughly what is expected given the range of observed velocity dispersions for groups (Ponman et al. 1996; Mulchaey et al. 1996; Mulchaey & Zabludoff 1998; Helsdon & Ponman 2000). X-ray hot gas component is referred to as the intragroup medium, in analogy with the diffuse X-ray emitting intracluster medium found in rich clusters (Forman & Jones 1982). The total kinetic energy contained in a group becomes  $\sim 10^{61-62}$  erg, so that it is one of the most energetic objects in the universe.

## 2.2 Galaxies

### 2.2.1 Classifications of galaxies

The group of galaxies contain spiral and elliptical galaxies, so their classifications are briefly mentioned here. Galaxies are found in a wide range of shapes, sizes and masses but can usefully be divided into several types according to how the total amount of light is divided between two components, the bulge and the disk.

The bulge dominates the central portions of galaxies and is distinguished by its stellar populations and dynamics. The distribution of bulge stars are close to spherically symmetric, and although they have large radial velocities comparable to their orbital velocities, they are supported against gravity through stellar “pressure”. The stars are collectively called as Population II system or a halo population. The Population II stars have aged sufficiently and are believed to have been formed at the early stage of the galaxy formation. This old population contains little amount of heavy elements by comparison with the Sun.

The disk is a flattened structure in which the stars move in very nearly circular orbits. The disk is associated with active star formation (young massive stars) and its associated debris (interstellar dust and molecular clouds), and classified as Population I or a disk population.

The family of galaxies formed by adding bulges and disks in different proportions is called

the Hubble sequence (figure 2.1). At the start of the sequence, it consists of elliptical galaxies. These galaxies have no discernible disks and are usually classified on the basis of axial ratio of their isophotes: E1 to E6, with the latter denoting a major-to-minor axis ratio of 6. The other major class, spiral galaxies, are named for the spiral patterns often evident in their disks, and are divided into three classes Sa, Sb, and Sc, in the order of increasing prominence of both the disk and the spiral arms. At the junction of the sequence, comes a class of galaxies known as lenticular galaxies or S0. After the ellipticals the Hubble diagram bifurcates into two branches and they are designated according to whether or not they are barred.

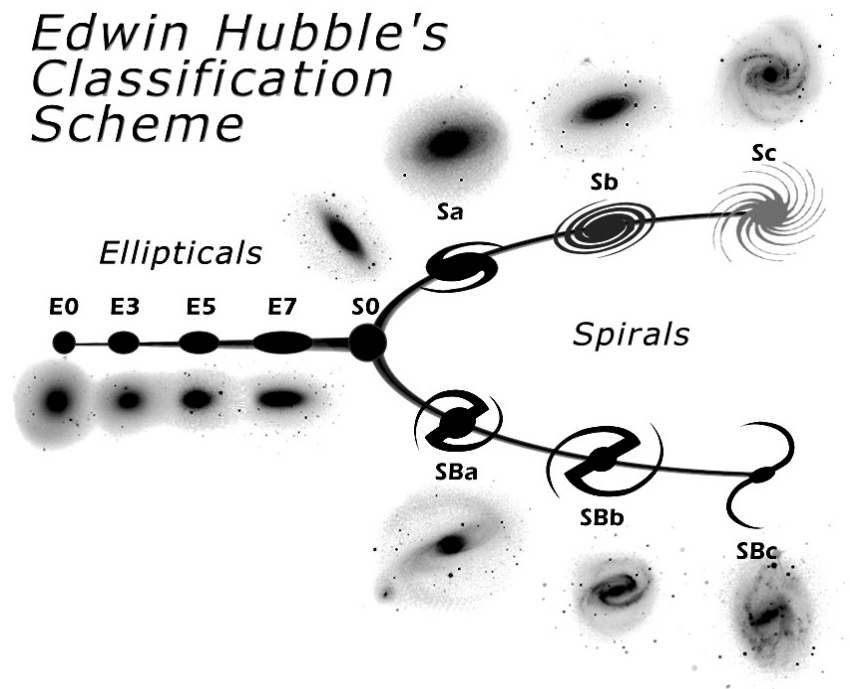


Fig. 2.1: Hubble tuning-fork diagram.

Because Hubble originally thought of his sequence as being an evolutionary path, ellipticals and S0's can be called as early-type galaxies, and spirals as late-type galaxies. Population I and II stars are also called early and late spectral types, so that early-type galaxies are dominated by late-type stars and vice versa.

### 2.2.2 Spiral galaxies

Many galaxies are examined in X-rays, in particular the near-by galaxies in detail. Chandra image of M31 (Andromeda Nebula), which is the nearest spiral galaxy in the distance of 600 kpc. In this galaxy, 204 X-ray source in total was found. The energy spectrum which represents bright sources can be fit by a power-law model with photon index of 1.8 well, and this is similar to that of the low mass binary systems. The spectrum is indeed comparable to the expected spectrum from our galaxy, in which X-ray luminosities of the low mass binary systems are generally higher

than those of high mass binary systems. The spectral feature also confirms that individual X-ray stars are brighter than the interstellar medium (ISM), and star formation activity is extremely low, although M31 is a large spiral galaxy.

In other spiral galaxies, IC342 and M33, many discrete sources indicate  $L_X > 2 \times 10^{38}$  ergs<sup>-1</sup>. These are called ultraluminous X-ray sources, and are thought to be binary systems including black holes.

### 2.2.3 Elliptical galaxies

The elliptical galaxies are regarded as systems in which star formation activities are finished, because they have little ISM and many old stars in comparison with the spiral galaxies as far as optical observations are concerned. They are often found in high galaxy density systems such as groups and clusters, and there are few examples of isolated systems. Therefore, elliptical galaxies may have been formed through mergers of spiral galaxies. The typical mass of a bright elliptical galaxy is about  $\sim 10^{11} M_\odot$ .

An evidence which shows that extensive star formations have occurred in the formation period of elliptical galaxies is the X-ray hot gas. This is typical for elliptical galaxies, and has been detected by X-ray observations for the first time. The widely extended X-ray halos are observed around elliptical galaxies. Such hot ISM is the product of supernova explosions in galaxies mixed with the gas from stellar mass loss heated by the stellar motion. The temperature of the gas is 0.5-1 keV, and this is almost equal to the depth of the gravitational potential of elliptical galaxies. Thus, elliptical galaxies produce a large amount of the hot gas (about 30% of the stellar mass) since the galaxy formation. However, most of the hot gas has escaped or has been stripped in cluster space, and contribute to the metal enrichment in the hot gas in groups and clusters. As a result, the mass of the hot gas with the elliptical galaxy is only about 5% of the stellar mass.

### 2.2.4 cD galaxies

cD galaxies (central dominant galaxies) are very bright and huge elliptical galaxies in the center of clusters and groups. The mass of cD galaxy is  $10^{12} - 10^{13} M_\odot$ , 10-100 times heavier than the normal galaxies. They also exhibit stellar halos extending out to 10-100 pc. Radio galaxies are often associated with cD galaxies, and cosmic jets are also seen in the radio through  $\gamma$ -ray bands. The galaxy M87 in the Virgo cluster is a typical cD galaxy. Generally, the central regions of clusters and groups tend to contain elliptical galaxies than spiral galaxies.

## 2.3 X-ray Gas in Groups

Diffuse X-ray emission from spiral dominant groups is usually much fainter than elliptical dominant groups. Whereas the bulk of ISM in spiral galaxies is in the form of HI and H<sub>2</sub>, the

ISM in ellipticals consists primarily of hot ( $T > 10^6$  K) plasma. This plasma produces X-rays by a combination of thermal bremsstrahlung, radiative recombination, and line emission from highly ionized trace elements. There are several models which calculate X-ray spectra from thin-thermal plasma, such as the MEKAL model (Kaastra 1992; Liedahl et al. 1995; Mewe et al. 1985; Mewe et al. 1986).

The emissivity of the free-free emission at a frequency  $\nu$  from a hot plasma with an electron temperature of  $T_g$  is given by

$$\epsilon_\nu = \frac{2^5 \pi e^6}{3 m_e c^3} \left( \frac{2\pi}{2 m_e k} \right)^{1/2} n_e \sum_i Z_i^2 n_i g_{ff}(Z, T_g, \nu) \times T_g^{-1/2} \exp(-h\nu/kT_g) \quad (2.1)$$

$$= \Lambda(T, Z, \nu) n_e^2 \quad (2.2)$$

where  $Z_i$  and  $n_i$  are the charge and number density of the element  $i$ , respectively, and  $n_e$  is the electrons number density (Rybicki & Lightman 1979). The Gaunt factor is a correction factor for quantum mechanical effects and is approximately  $g_{ff} \sim 0.9(h\nu/kT)^{-0.3}$ . The emissivity in a given bandpass,  $\nu_1 < \nu < \nu_2$ , is then

$$\epsilon^{ff} = \int_{\nu_1}^{\nu_2} \epsilon_\nu^{ff} d\nu \quad (2.3)$$

$$= \Lambda(T, Z) n_e^2. \quad (2.4)$$

The formula  $\Lambda(T, Z)$  is the cooling function, with  $T$  and  $Z$  representing the plasma temperature and the heavy element abundance, respectively. The contribution of the bremsstrahlung continuum to  $\Lambda$  increases as  $\propto T^{1/2}$ .

Emission of atomic lines becomes significant when the ICM temperature falls below a few keV. Since the temperature of the ICM is of the same order as the K-shell ionization potentials of heavy elements such as O, Ne, Mg, Si, S and Fe, these elements become mainly He/H-like ions and are completely ionized. These ions are collisionally excited, and then emit their resonance K-lines. In lower temperature clusters and groups, in which Fe ions are not only He-like but also of a low ionization status, the spectrum exhibits resonance L-lines at  $\sim 1$  keV. We show predicted X-ray spectra for various temperature in figure 2.2.

The emission lines and continuum spectra from the ionization equilibrium plasma have been calculated by various authors, e.g. Raymond & Smith (1977), Kaastra & Mewe (1993), and so on. In this thesis, we use the MEKAL code, which is based on the model calculations of Mewe et al. (1986); Kaastra & Mewe (1993) with Fe L calculations by Liedahl et al. (1995), in the XSPEC data analysis Package.

In calculating the emission models, the abundances of heavy elements ( $Z$ ) is usually specified. A basis of  $Z$  is solar abundances ( $Z_\odot$ ), thus the ratio of the number of an atom for hydrogen (number abundance) is used. In this thesis, I use the solar abundances (the ratio to hydrogen) given by Anders & Grevesse (1989), listed in table 2.1.

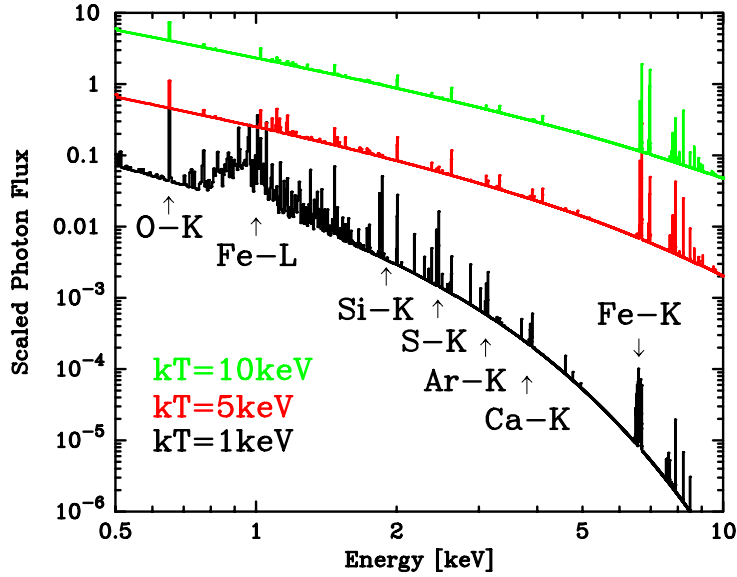


Fig. 2.2: Calculated X-ray spectra from optically thin hot plasma with various temperatures. The MEKAL plasma emission code is used, assuming a metal abundance of 0.3 solar. Vertical scale is arbitrary.

Table 2.1: Definitions of the solar abundances by number (Anders & Grevesse 1989).

element	number	element	number	element	number
H	1.00	Na	2.14e-6	Ar	3.63e-6
He	9.77e-2	Mg	3.80e-5	Ca	2.29e-6
C	3.63e-4	Al	2.95e-6	Cr	4.84e-7
N	1.12e-4	Si	3.55e-5	Fe	4.68e-5
O	8.51e-4	S	1.62e-5	Co	8.60e-8
Ne	1.23e-4	Cl	1.88e-7	Ni	1.78e-6

### 2.3.1 Existence of intragroup medium

A much more complete study of the HCGs was presented by Ponman et al. (1996). This survey combined pointed ROSAT PSPC observations with ROSAT All-Sky Survey data to search for diffuse gas in 85 HCGs. He detected extended X-ray emission in 26% (22 of 85 groups) of the systems studied and inferred that 75% of the HCGs contain a hot intragroup medium. Among the 109 galaxy groups observed with the ROSAT PSPC, extended X-ray emission has been detected in at least 61 groups. No diffuse emission was detected in 12 groups with only spiral members (Mulchaey et al. 2003). Recently the GEMS project constructed a large sample containing 60 groups based on the optical and ROSAT PSPC catalogues (Osmond & Ponman 2004). The X-ray emission was detected for three of the five spiral-only groups; however, due to the limited quality of the data, the origin of the emission was not directly constrained,

but was classified into hot halos of the individual galaxies based on their threshold in the spatial extent of  $< 60$  kpc. They suggested, based on the anti-correlation between the spiral fraction and the X-ray luminosity, that the presence of detectable hot diffuse gas is strongly related to the galaxy morphology (figure 2.3). The possible absence of diffuse X-rays in the spiral-only groups would thus imply that either the bound group should contain at least one early-type galaxy, or the X-ray emission is preferentially suppressed in the spiral-only groups for some reason.

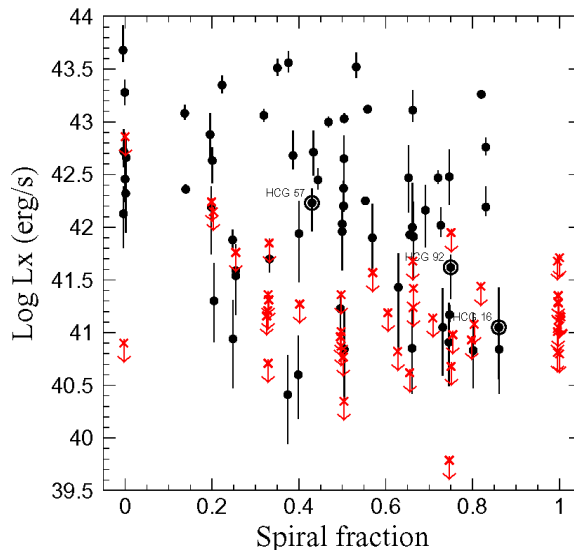


Fig. 2.3: The relation between the spiral fraction  $f_{sp}$  and the X-ray luminosity  $L_X$  (Mulchaey et al. 2003). The red crosses represent the upper limit. Spiral only groups are  $f_{sp} = 1$ .

To further explore the nature of the diffuse emission from the groups of galaxies, higher quality X-ray data are required. In particular, a high spatial resolution is crucial to separate the emission associated with individual galaxies from the diffuse component. Chandra and XMM-Newton are the most suitable satellites for this purpose, yet there have so far been few available observational results. Belsole et al. (2003) recently reported on the detection of diffuse X-ray emission from HCG 16 ( $z = 0.013$ ) with the XMM-Newton EPIC cameras. The temperature and the luminosity were measured to be  $0.49 \pm 0.17$  keV and  $5.0 \times 10^{40} h_{70}^{-2}$  erg s $^{-1}$ , respectively. The result obeys the  $L_X - T$  relation obtained for brighter galaxy groups, though it is located at the extreme faint end, from which they suggested that HCG 16 is a bound system.

The X-ray emission tends to be suppressed in spiral-dominated groups (Osmond & Ponman 2004), with a possible exception of HCG 57, from which Fukazawa et al. (2002) detected extended thermal X-ray emission with ASCA (figure 2.4). Despite large observational errors, these facts are likely to indicate a close link between galaxy evolution and the properties of the intragroup medium.

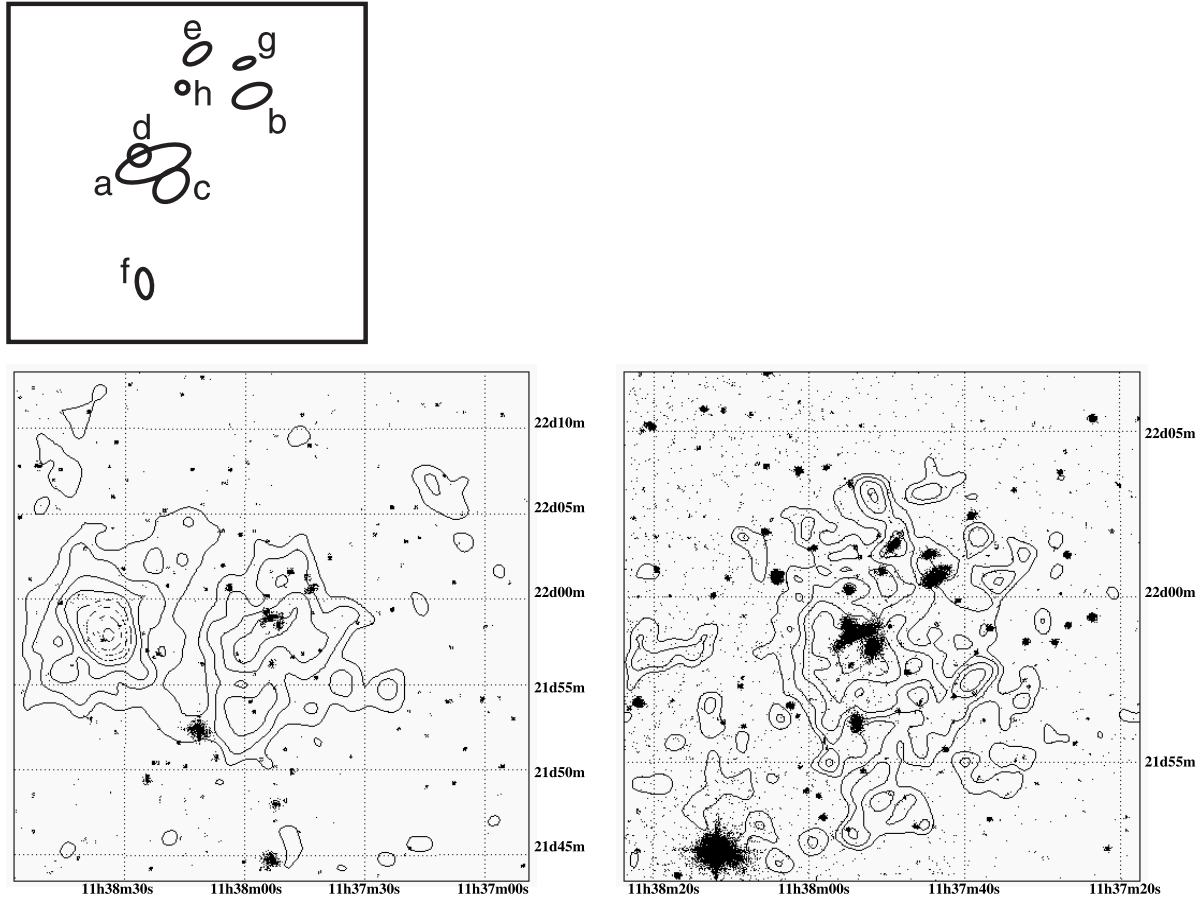


Fig. 2.4: X-ray images (contours) of the HCG 57 obtained with the GIS (left) and SIS (right), overlaid on the optical image (Fukazawa et al. 2002). The top panel indicates the galaxy position (referred to Hickson (1993)). The bottom panels are images in 0.6-2.0 keV.

### 2.3.2 Chemical properties

#### Supernova explosion

Stars which have mass  $> 8M_{\odot}$  cause supernova explosions, when they can not be supported by the heat of nuclear fusion. On the other hand, lower mass stars, compare to them, become white dwarfs. Supernova explosions cause rapid nuclear fusions by a high temperature and pressure, and the heavy elements are scattered into ISM. Such heavy elements are captured by stars of the next generation, thus study of the ISM chemical properties is very important to look into the metal circulations in galaxies. Actually, elements constituting a material on the earth and our body have been composed by star in galaxies formerly.

For supernovae, there are two kinds of explosions, which are Type-Ia (SN Ia) and type-II SNe (SN II). SN Ia continues supplying Fe and Ni for a long time, and SN II occurred mainly in the starburst period after the galaxies formation and produced  $\alpha$  elements (O, Ne and Mg). SN Ia is believed to occur as a result of the accretion of material from a companion to a white

dwarf (old, degenerate low-mass stars) in a close binary system. It is thought to explode beyond the Chandrasekhar mass ( $\sim 1.4 M_{\odot}$ ), after gas is accumulated from a primary star in a binary system to the white dwarf. SN Ia continues occurring at the almost constant period over the age of the universe rather than only the galaxy formation period.

While SN II arise from young stars with initial mass  $> 8M_{\odot}$ , whose cores collapse gravitationally once they have exhausted all the star's fuel. At this time, neutron stars and black holes are produced. Most of this energy  $\sim 10^{53}$  erg are emitted as a neutrino, and energy of approximately 1% is used for an explosion. Just after the galaxy formation, a large number of heavy stars are produced, and it is thought that they cause SN II for a period of  $10^{8-9}$  yr.

### Metal formation

Whereas elements from He to Be are mainly produced by the nucleosynthesis just after the Big Bang, elements such as O, Ne, Mg, Si and Fe are produced by stars and supernovae. How were these elements distributed over the galaxies and clusters widely? The answer will be given by the study of chemical properties of groups and clusters of galaxies. This will also tell us the star formation history and the past supernova activity of galaxies. In particular, X-ray hot gas contains a large amount of metals. These are originated from interstellar medium which was enriched by supernova explosions and stellar mass loss. Then the gas escaped or was stripped from the galaxies (by galactic winds or by ram pressure strippings) and transferred into the intergalactic gas. The observation of metal content in clusters and groups was initiated by ASCA, which discovered that cD galaxies such as M 87 produced already a large quantity of metals. The metals were produced in the galaxy formation epoch, as well as the current supply from the stars where elements are seen now (figure 2.5; Arnaud et al. (1992)). Therefore, in the process of evolution of the universe, the star formation activity and the metal production should have occurred in a wide scale.

X-ray gas in elliptical dominant galaxy groups often contains heavy elements abundantly. It offers important information in examining the process of the metal enrichment over  $10^{10}$  years. Since gravitationally large systems have all the elements which stars and galaxies have produced since the universe has begun. Moreover, with the gas temperatures characteristic for groups ( $\sim 1$  keV), strong emission lines are expected from many of the  $\alpha$ -elements. In figure 2.6, the energy spectra of the center of NGC 4636 group observed with ASCA and with RGS on XMM-Newton are shown.

Detailed studies on the metal distribution in clusters and groups have been carried out using ASCA, BeppoSAX, Chandra and XMM-Newton. Distribution of iron and silicon indicate strong central concentration in clusters and groups characterized by bright central galaxies, and the excess iron mass is found to correlate with the luminosity of the cD galaxy as shown in figure 2.5 (De Grandi et al. 2004). This indicates that iron and silicon (main products from type Ia supernova; SN Ia) trace the enhanced star-formation activity in bright galaxies. On the other

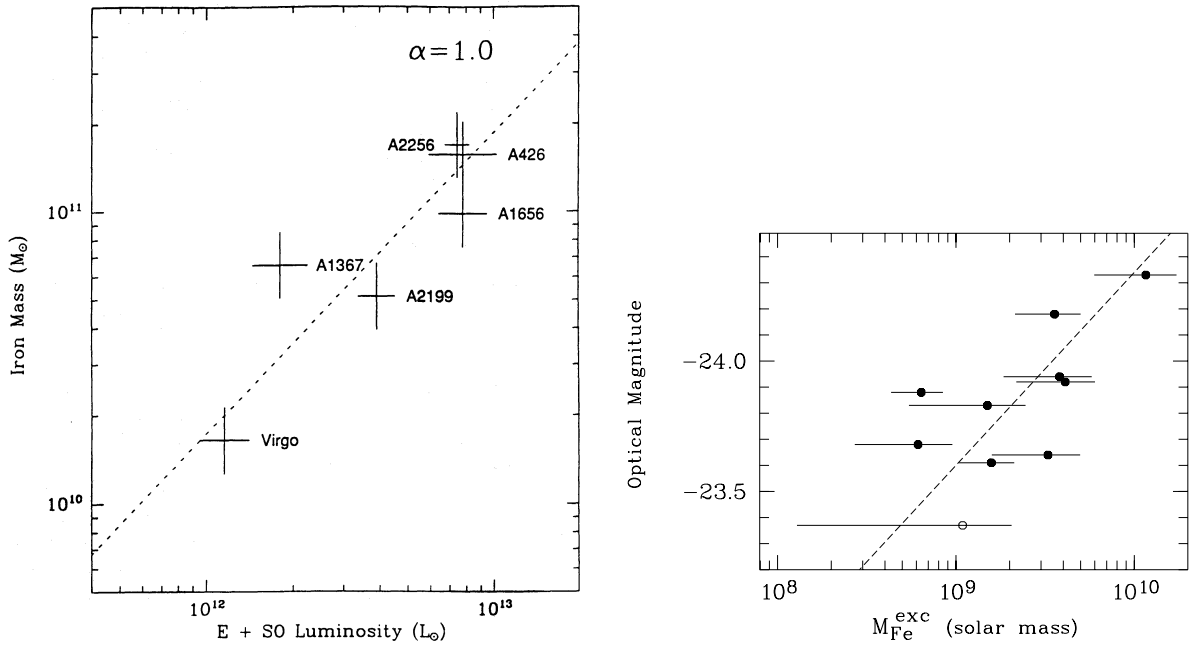


Fig. 2.5: Left: The sum of the luminosities of E and S0 galaxies for the iron mass for the clusters with measures iron abundance, gas mass and luminosity (Arnaud et al. 1992). Right: BCG optical magnitude as a function of iron mass excess. Open circle marks the binary cluster A2142 (De Grandi et al. 2004). Dashed line is the best-fitting power law excluding A2142.

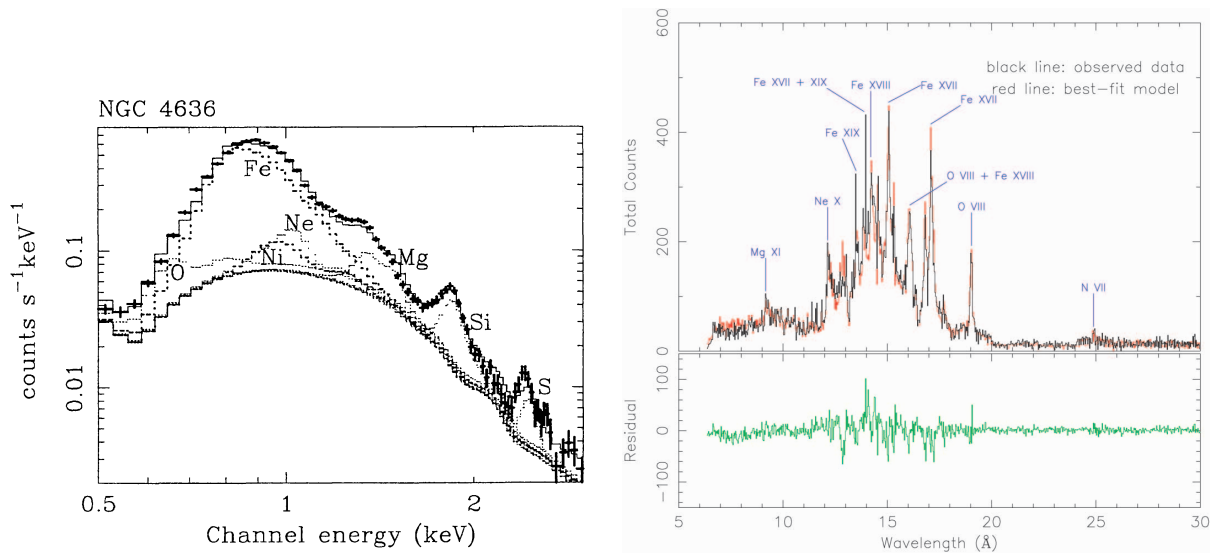


Fig. 2.6: Left: the energy spectra of NGC 4636 with ASCA (Matsushita et al. 2000). Right: same as left but with XMM-Newton RGS (Xu et al. 2002).

hand, distribution of oxygen (i.e. type II supernova product; SN II) is not well understood. Matsushita et al. (2003) showed that oxygen distribution around M 87 is flatter than those of iron and silicon, with the level about half as much as the others. Such low oxygen abundances are also derived in the centers of other clusters and groups (Buote et al. 2003b; Xue et al. 2004). For the study of oxygen distribution, low temperature systems such as groups of galaxies are suitable targets.

### 2.3.3 $L_X$ - $kT$ relation

In the previous ROSAT observations, Mulchaey & Zabludoff (1998) found that a single luminosity–temperature relationship could describe groups and clusters ( $L_X \propto T^{2.8}$ ). However, both Ponman et al. (1996) and Helsdon & Ponman (2003) found much steeper relationships for groups compared to that of clusters of galaxies, which is noticeable for low temperature ( $kT \lesssim 1$  keV) systems ( $L_X \propto T^{8.2}$  and  $L_X \propto T^{4.9}$ , respectively). Figure 2.7 suggests that the deviation of the cool groups from the cluster relationship is indeed significant. The preheating effect, non-gravitational heating, is suggested to be responsible for the steepening in groups (e.g., Ponman et al. 1996; Helsdon & Ponman 2003). In particular, it has been proposed that spiral galaxies play a comparable role to early types in gas heating. However, it is also possible that the low X-ray luminosities of the groups is due to an escape of the hot gas from the system, and further investigations are needed to clarify the origin of this steep relation.

## 2.4 X-ray Emission Other Than Diffuse Hot Gas

### 2.4.1 X-ray emission from discrete sources

In the center of clusters and groups, there are point-like sources such as active galactic nuclei (AGNs) and low mass X-ray binaries (LMXBs) contained in the individual member galaxies. The spiral galaxies characterized by extremely bright cores are called Seyfert galaxies, which are typical AGNs within  $z < 0.1$ . AGNs are believed to have black holes with a mass of  $10^{6-8} M_\odot$ , producing intense jets and outbursts in various energy bands. AGNs are usually the brightest objects in the sky in many wavelengths, from radio to  $\gamma$ -ray. The luminosities often go up to  $\sim 10^{45}$  erg s<sup>-1</sup>. Most of the X-ray bright AGNs can be identified as point like sources, associated with galaxies. Their spectra are hard, and can be generally represented with power-law models with photon indices  $\Gamma = 1 \sim 2$ .

The jet emits radio as well as X-rays, and the multi-wavelength studies have performed extensively. Energy spectra of the jets are also fitted with power-law models, and the emission is likely to be synchrotron radiation with self-Compton components. There are evidences that the jets have relativistic velocities. Near black hole or in the jet, there should be an efficient mechanism to accelerate particles, however the detailed mechanisms are still unclear. In addition, it is not understood whether the jets mainly consist of electrons or protons.

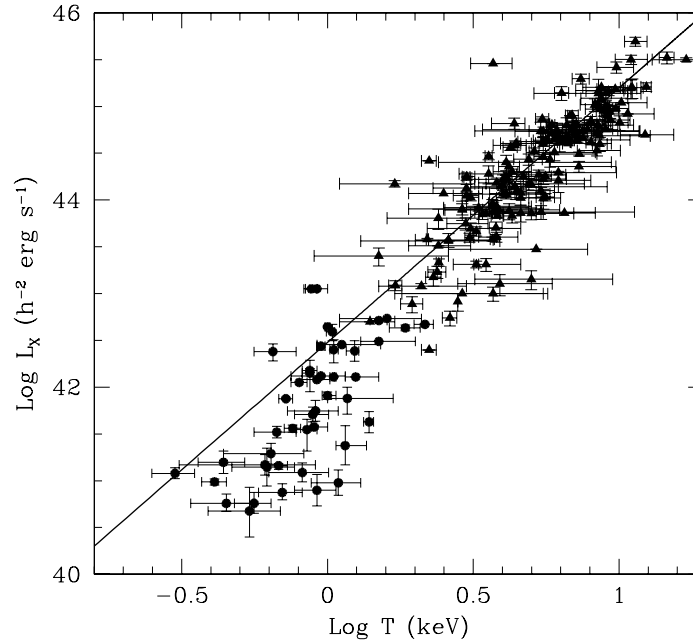


Fig. 2.7: Logarithm of the X-ray temperature versus logarithm of X-ray luminosity for a sample of groups (circles) and clusters (triangles). The group data are taken from the literature compilation of Xue & Wu (2000), with the addition of the groups in Helsdon & Ponman (2000). The cluster data are taken from Wu et al. (1999). The solid line represents the best-fit found by Wu et al. (1999) for the clusters sample (using an orthogonal distance regression method). The observed relationship for groups is somewhat steeper than the best-fit cluster relationship.

LMXBs are the luminous population in normal galaxies, consisting of low mass stars and weakly magnetized neutron stars. The spectra of them are known to be approximated by  $\sim 10$  keV thermal bremsstrahlung emission model (Makishima et al. 1989; Matsushita et al. 1994; Matsumoto et al. 1997). The luminosity of individual LMXBs are fairly low at  $\sim 10^{36-37}$  erg s $^{-1}$ . Matsushita (1998) analyzed X-ray spectra of 27 elliptical galaxies with ASCA, and found that there were hard emission distinct from the ISM emission, which can be attributed to LMXBs. By fitting the former component with a  $\sim 10$  keV bremsstrahlung model, the 2-10 keV luminosity is estimated as,  $L_X(2 - 10 \text{ keV}) = 4.1 \times 10^{39} (L_B/10^{10} L_\odot)$  erg s $^{-1}$ .

#### 2.4.2 Hard X-ray emission

Recently, non-thermal hard X-ray emission has been reported from the Coma cluster by *Bp-poSAX* and *RXTE* satellites as shown in figure 2.8 (Fusco-Femiano et al. 1999; Rephaeli et al. 1999). The emission is observed as a hard excess above the thermal ICM emission, appearing in energies above  $\sim 30$  keV. Together with the diffuse radio halo detected in this cluster, the hard X-rays strongly suggest the existence of high energy particle widely distributed in the intergalactic space.

Given the difficulties with the discrete source and thermal interpretations of the diffuse hard X-ray emission, we regard the nonthermal interpretation to be most promising. One popular scenario for the nonthermal X-ray production is inverse Compton scattering of the CMB photons by relativistic electrons with Lorentz factor  $\gamma \sim 10^3 - 10^4$ , as has been invoked to explain the excess hard X-ray emission from rich clusters (Fusco-Femiano et al. 1999). However, since there are negative reports concerning the existence of the hard X-ray emission, we have to wait for further sensitive studies on this possible component. Thus, it is not clear how much non-thermal pressure is present in the cluster space which should be associated with high-energy particles and magnetic fields.

Thermal emission of the groups is limited to energies below  $\sim 5$  keV, because the temperature of their hot intragroup medium is about 1 keV (Mulchaey et al. 1996; Fukazawa et al. 1996). Therefore, they allow us to search for nonthermal X-ray emission, even with instruments operating below an energy of  $\sim 10$  keV.

From the galaxy group HCG 62, Fukazawa et al. (2001) have detected the excess X-ray emission with a very hard spectrum. The excess emission is spatially extended up to  $\sim 10''$  from the group center as shown in figure 2.8. However, the optical evidence for AGNs in HCG 62 is moderate, and they cannot constrain the intragroup magnetic field in HCG 62 because of the lack of information on the diffuse radio flux.

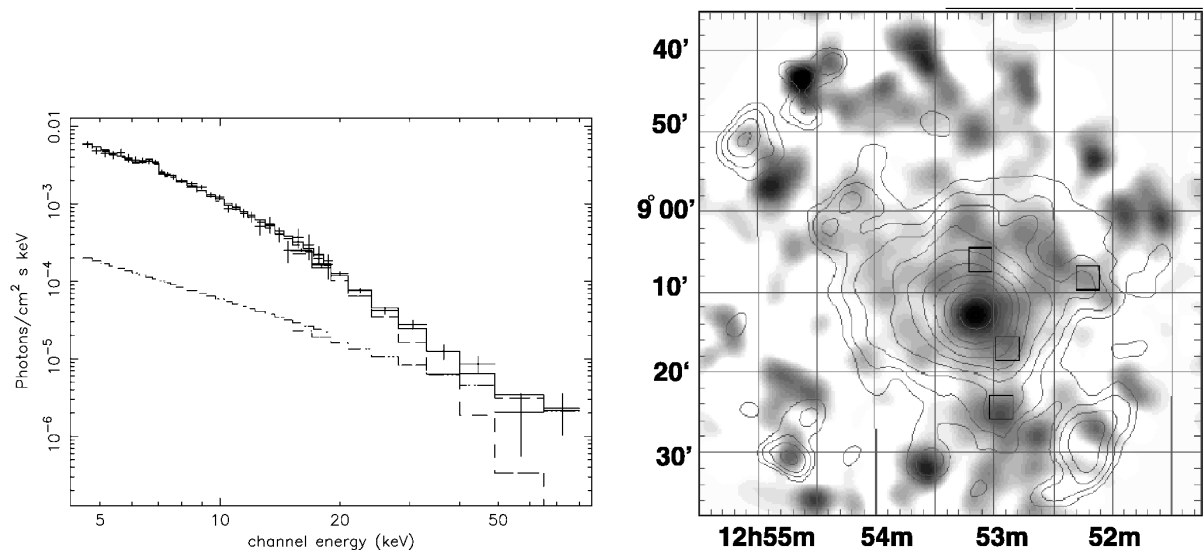


Fig. 2.8: Left: The spectrum of the Coma Cluster by *BeppoSAX* HPGSPC (4.5-20 keV) and PDS data (15-80 keV), with the best-fit model shown with a solid line. The dashed line represents the thermal component (8.5 keV), while the dashed straight line is the nonthermal component with a spectral index of 1.6. Right: Background-subtracted GIS (ASCA) image of HCG 62 in 4.5-8 keV (gray scale, hard band) and 1.0-2.4 keV (contours, soft band). The four squares are positions of the ROSAT point sources that are also detected with the GIS.

## 2.5 Galaxy Interaction

### 2.5.1 Starbursts

In spiral galaxies and irregular galaxies, there are galaxies in which star formations are extremely active, and are called starburst galaxies. The occurrence of supernova explosions is as high as once per ten years, 10 times higher than the level in our galaxy. As a result, compact stars and black holes are produced, and the interstellar matter is heated and galactic winds are generated.

The starburst activities are recognized in the central regions of spiral and irregular galaxies such as M 82 and NGC 253. These are the brightest, the best-studied starburst galaxies in the X-ray band. Previous observations suggested a causal link between the starburst activity and the galaxy interactions [see Kennicutt (1998) for reviews]. Thus, a detailed spatial analysis of individual galaxies with high resolution X-ray image provides a vital clue in constraining the connection between the outflowing gas and the intragroup medium without suffering from the contamination of point sources. The Chandra observations revealed X-ray views of the extended halo emission from the nearby starburst and normal galaxies in the dense environment. For example, the nature of diffuse X-ray emission from NGC 253 and NGC 55, both of which belong to the nearby spiral-only group, the Sculptor group, is considered separately in Strickland et al. (2002) and Oshima (2003). They exhibit observational evidence for galactic outflows from the spirals powered by star-formation activity. Strickland et al. (2004a) and Strickland et al. (2004b) studied ten star-forming disk galaxies with the Chandra X-ray and  $H\alpha$  imaging data. From the correlations between a variety of X-ray quantities with multi-wavelength data, they quantitatively investigated supernova feedback on the galactic scale.

Starburst galaxies are usually brighter in infrared than optical. because starburst galaxies has much dust. From an infrared sky survey, galaxies with extremely high luminosity in infrared (ULIRGs: Ultra Luminous InfraRed Galaxy) were found. It is recognized that these galaxies have either starburst activity or AGN, or both.

The velocity that gas flows out from galaxy is necessary up to  $1000 \text{ km s}^{-1}$  to escape the gravitational potential. Therefore, galaxies are not closed systems, and the gas outflow enriched with heavy elements supply over intergalactic medium. This is very important in studying the origin of elements in the groups and clusters.

### 2.5.2 Cavities

The striking gas features most likely caused by the central galaxies are the X-ray cavities. The cavities are circular regions showing a significant depression of X-ray surface brightness. Nearly 20 cavities have been recognized in clusters and groups with high resolution images taken by ROSAT and Chandra (Birzan et al. 2004, hereafter B04; Dunn & Fabian 2004; Dunn et al. 2005, hereafter D05). They are located typically at 10–30 kpc from the central galaxies, and strong correlation with radio lobes are seen in about 10 systems. Remarkable cases are seen

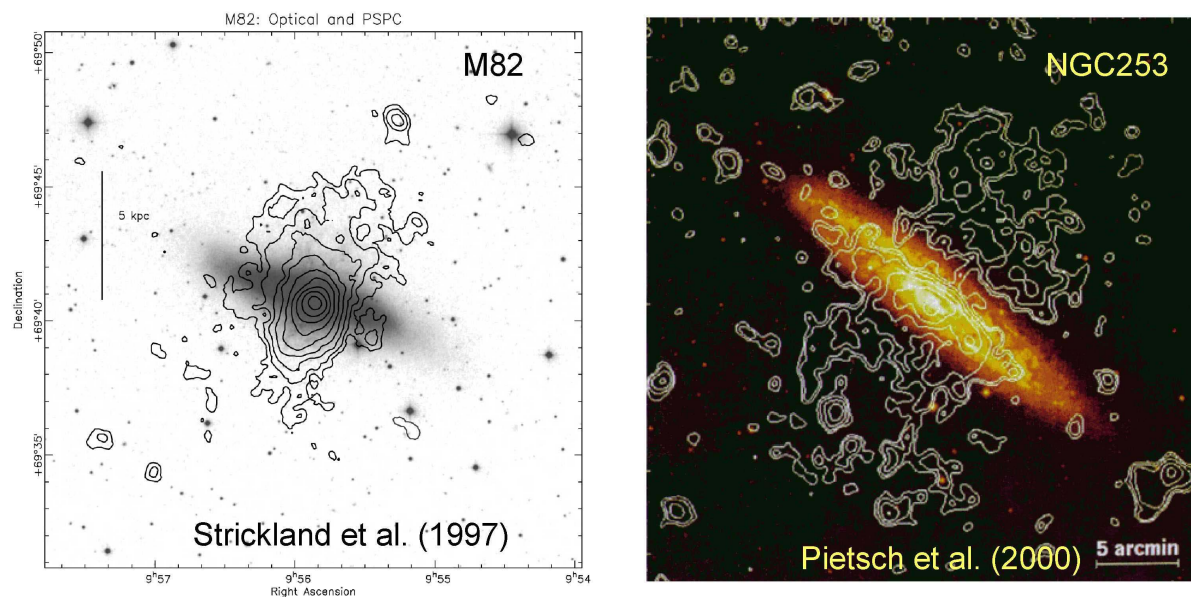


Fig. 2.9: X-ray contour of starburst galaxies as M 82 and NGC 253.

in the Perseus (e.g., Boehringer et al. 1993; Fabian et al. 2000) and Hydra A (e.g. McNamara et al. 2000, figure 2.10) clusters, both showing strong correlation with the 1.4 GHz radio lobes.

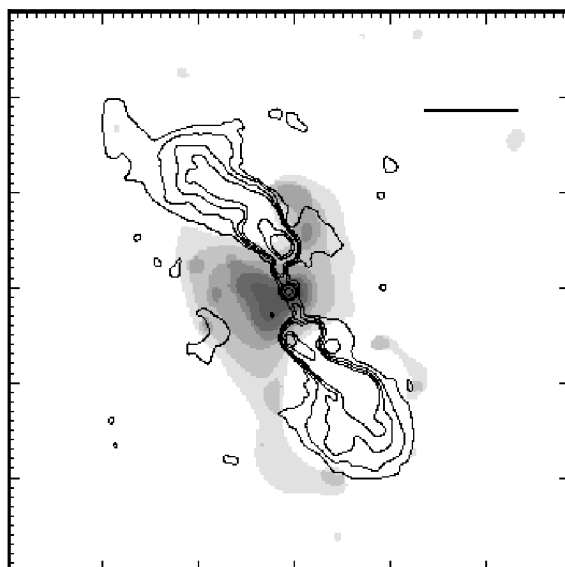


Fig. 2.10: X-ray image of HydraA. The contour represents the radio emission (1.4 GHz).

The center of the Perseus cluster is shown in figure 2.11. The central nucleus is radio galaxy of NGC1275, which is an AGN, and shows soft emission. There are two cavities in the north and south. The temperature map shows no differences around the cavities. In the radio contour, the radio lobe corresponds to the X-ray cavities. Cavities are thought to be produced by jets or

buoyant bubbles which are directly connected with the activity of central radio galaxies. The pressure of the radio lobe (magnetic field and relativistic electron) may expell the hot gas. The energy content of the cavities is estimated to be  $8 \times 10^{58}$  erg, however, its life is  $10^{7-8}$  yr due to synchrotron emission. Thus, the energy must be continuously supplied at a rate of  $10^{44}$  erg  $s^{-1}$  from the nuclear source.

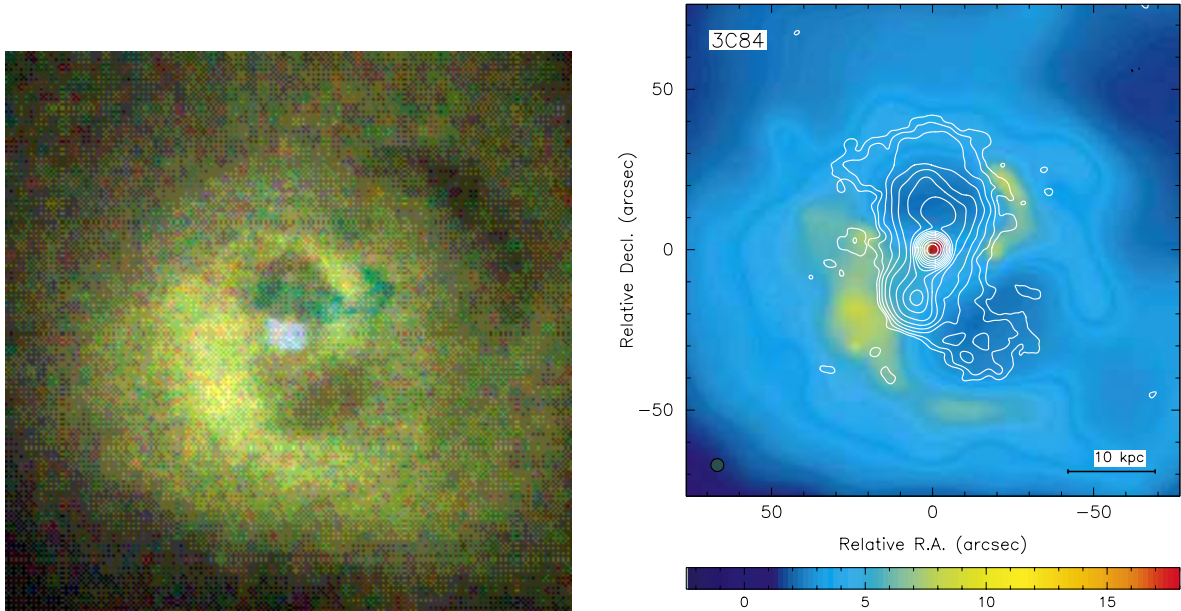


Fig. 2.11: Left: The color image of the center of Perseus cluster. Red of 1.5-1 keV, green of 1-2 keV, and blue of 2-7 keV are composed. Right: X-ray image of Perseus cluster (Fabian et al. 2000). The contour represents the radio emission (1.4 GHz).

Several giant elliptical galaxies with radio lobes, e.g., M84 (Finoguenov & Jones 2001), NGC 4636 (Ohto et al. 2003), are also known as hosting X-ray cavities. The remaining half of the cavities, on the other hand, are not associated with radio lobes, and they are designated as ghost cavities. The one in A 2597 (McNamara et al. 2001) or the outer depressions in the Perseus cluster (Fabian et al. 2000) are the examples.

A subsonic displacement of the gas would create a low density, rising bubble keeping the pressure balance with the surrounding ICM. It appears to be generally correct for cavities that non-thermal pressure originated in relativistic particles and/or magnetic fields in the radio lobe is probably large enough to balance with the surrounding ICM gas pressure (Fabian et al. 2002). This pseudo-pressure balance is justified by the fact that there are no evidence for shock-heated gas around the radio lobes in almost all of the X-ray cavities observed so far, except for MKW 3s (Mazzotta et al. 2002). This general scenario has been modeled theoretically, and has at least qualitatively reproduced the morphology of cavities (e.g., Churazov et al. 2001). Energy density of relativistic electrons inferred from the synchrotron radio emission is almost always smaller

than that required to offset the hot gas by orders of magnitude, and it is discussed that energy density of protons are higher than those due to electrons by factors of 100–1000 (D05). However, there is no direct evidence indicating that such a high energy density is really carried by protons. This situation is the severest in the case of ghost cavities. In this view, it is important to examine ghost cavities in groups of galaxies where the gas is relatively cool and non-thermal effect can be recognized somewhat easily.

## 2.6 X-ray Gas Distribution

The X-ray emitting gas in groups of galaxies are considered to be in hydrostatic equilibrium in the gravitational potential containing dark matter, hot gas, and stars. The density and pressure of the gas,  $\rho_{\text{gas}}$ ,  $p_{\text{gas}}$  and galaxy,  $\rho_{\text{star}}$ ,  $p_{\text{star}}$  are written as

$$p_{\text{gas}} = \rho_{\text{gas}} \frac{kT}{\mu m_p}, \quad p_{\text{star}} = \rho_{\text{star}} \sigma^2. \quad (2.5)$$

Assuming that the galaxies follow the hydrostatic equation of the galaxies,

$$\frac{1}{\rho_{\text{gas}}} \frac{dp_{\text{gas}}}{dr} = \frac{1}{\rho_{\text{star}}} \frac{dp_{\text{star}}}{dr} = -\nabla\phi, \quad (2.6)$$

where  $\mu = 0.62$  is the mean molecular weight, and  $m_p$  is the proton mass. Then, we obtain

$$\rho_{\text{gas}} \propto \rho_{\text{gal}}^\beta \quad (2.7)$$

where

$$\beta \equiv \frac{\mu m_p \sigma^2}{kT}. \quad (2.8)$$

King (1962) has derived an analytic approximation to the isothermal sphere of self-gravitational isothermal collision-less particles. The density profiles of the galaxies have been found to be well approximated with the King profile,

$$\rho_{\text{star}}(r) \sim \rho_{\text{King}}(r) = \rho_{\text{King}}(0) \left[ 1 + \left( \frac{r}{R_c} \right)^2 \right]^{-\frac{3}{2}}, \quad (2.9)$$

where  $r_c$  is a core radius. Then the isothermal gas distribution may be represented as

$$n_{\text{gas}}(r) = n_{\text{gas}0} \left[ 1 + \left( \frac{r}{r_c} \right)^2 \right]^{-\frac{3}{2}\beta}, \quad (2.10)$$

where  $n(r)$  is number density in the radius  $r$ , and  $n_0$  is the value at  $r = 0$ .

Since the emissivity is proportional to  $n^2$ , we obtain the X-ray surface brightness  $S(r)$  at a projected radius  $r$ ,

$$S(r) = \Lambda(T) \int_0^\infty 2n(z, r)^2 dz = \Lambda(T) \int_0^\infty dz \frac{2n_0^2}{\left[ 1 + \frac{r^2+z^2}{r_c^2} \right]^{3\beta}} \quad (2.11)$$

$$= S_0 \left[ 1 + (r/r_c)^2 \right]^{-3\beta+1/2}. \quad (2.12)$$

Here,  $S_0$  is the central surface brightness as

$$S_0 = \frac{n_0^2 \Lambda(T) r_c}{4\sqrt{\pi} (1+z)^4} \frac{\Gamma(3\beta - 3/2)}{\Gamma(3\beta)} \quad (\text{erg cm}^{-2} \text{ s}^{-1} \text{ sr}^{-1}), \quad (2.13)$$

where  $\Lambda(T)$  is the cooling function, using  $norm = \int n^2 dV / (4\pi D_A^2)$  ( $10^{-14} \text{ cm}^{-5}$ ) and flux  $F_X$  in the spectrum fitting with the Mekal model, we obtain

$$\Lambda(T) = \frac{(1+z)^2 F_X}{norm \times 10^{14}} \quad (\text{erg cm}^3 \text{ s}^{-1}). \quad (2.14)$$

Therefore, the central number density is represented as

$$n_0 = \left( \frac{4\sqrt{\pi} (1+z)^2 S_0}{r_c} \frac{norm \times 10^{14}}{F_X} \frac{\Gamma(3\beta)}{\Gamma(3\beta - 3/2)} \right)^{1/2} \quad (\text{cm}^{-3}). \quad (2.15)$$

It has been known that the observed cluster X-ray surface brightness is well fitted by equation 2.10 with  $\beta \sim 0.6 - 0.7$  (Jones & Forman 1984). However recent observational studies of the clusters with *Chandra* and *XMM-Newton* observation reveal that a number of clusters could not be represented by the simple  $\beta$  profile.

Recent  $N$ -body simulation on the formation of clusters in a cold dark matter (CDM) universe has shown that, instead of a King profile with a central core, profile with central cusp is found (Navarro et al. 1996; Navarro et al. 1997), hereafter NFW profile. It is represented as

$$\rho(r) = \frac{\rho_0}{(r/r_s)(1+r/r_s)^2}, \quad (2.16)$$

where  $\rho_0$  and  $r_s$  are the characteristic density and length, respectively.  $\rho_0$  is related to the critical density of the universe  $\rho_{\text{crit}}$  and characteristic density  $\delta_c$  through  $\rho_s = \delta_c \rho_{\text{crit}}$ . Compare with the flat core of the King profile, the NFW profile has a core with  $\propto r^{-1}$  dependence. However, there are some observational results which cannot be explain by the NFW profile (Ikebe et al. 1996). Thus, the actual profile of the dark matter density is still under discussion. The  $\beta$  model still works as a reasonable description of the gas density profile.

## 2.7 Mass Distribution

Groups have the velocity dispersion ranging from  $100 \sim 400 \text{ km s}^{-1}$ , and a total mass of several times  $10^{13} M_\odot$  within  $\sim 250 \text{ kpc}$ , which is dominated by the dark matter.

Since the collision time scale for ions and electrons in the intracluster gas is much shorter than the time scales of the heating or cooling, we can treat the gas as a fluid (Sarazin 1988). In general, the time required for a sound wave in the intracluster gas to cross a cluster (sound crossing time) is shorter than the probable age of a cluster. Therefore we can assume that the gas is under a hydrostatic equilibrium, so that the pressure gradient is balanced with the gravitational force as,

$$\nabla P_{\text{gas}} = -\mu m_p n_e \nabla \phi. \quad (2.17)$$

Since the ICM density is quite low, the gas pressure can be expressed as

$$P_{\text{gas}} = n_{\text{gas}} kT = \frac{\rho_{\text{gas}}}{\mu m_{\text{p}}} kT, \quad (2.18)$$

where  $k$  is the Boltzman constant, and  $\rho_{\text{gas}}$  is the gas mass density,  $\rho_{\text{gas}} = 1.92\mu m_{\text{p}} n_{\text{e}}$ . When we assume a spherical symmetry and the hydrostatic equilibrium, the total integrated gravitational mass,  $M_{<R}$ , (i.e. the dark matter + galaxies + hot gas) within the 3-dimensional radius of  $R$  is given by

$$M_{<R} = -\frac{R^2}{\rho_{\text{gas}} G} \frac{dP_{\text{gas}}}{dR}, \quad (2.19)$$

using the equation (2.17), in which  $G$  is the gravitational constant. The differential mass density,  $M(R)$ , is given by

$$M(R) = \frac{1}{4\pi R^2} \frac{dM_{<R}}{dR}. \quad (2.20)$$

## 2.8 HCG 80

There are two well-studied spiral *dominant* groups, HCG 16 (Belsole et al. 2003) and HCG 57 (Fukazawa et al. 2002). However, intragroup medium and the gas associated with the galaxies are not separated yet, due to the low spatial resolution. Furthermore, they are not spiral *only* groups. The observation of spiral only group with high spatial resolution is needed to definitely confirm the role of spiral galaxies in groups. Therefore, a spiral-only group of galaxies, HCG 80, was observed for the first time in X-ray with Chandra, which has the finest angular resolution ( $\sim 1''$ ) than ever.  $1'$  corresponds to 36.1 kpc at the group redshift  $z = 0.0299$ .

This group is one of the most promising candidates, among the known spiral-only groups, for the positive detection of diffuse X-rays for the following reasons: (1) The high line-of-sight velocity dispersion of  $\sigma_{\text{v}} = 309 \text{ km s}^{-1}$  implies a large gravitational potential; accordingly high X-ray luminosity and temperature of  $L_{\text{X}} \sim 8.4 \times 10^{41} h_{70}^{-2} \text{ erg s}^{-1}$  and  $kT \sim 0.8 \text{ keV}$  are expected from the  $\sigma_{\text{v}} - L_{\text{X}}$  and  $\sigma_{\text{v}} - T$  correlations (Ponman et al. 1996). The expected luminosity is close to the  $3\sigma$  upper limit from the previous ROSAT PSPC observation,  $L_{\text{X}} = 7.6 \times 10^{41} h_{70}^{-2} \text{ erg s}^{-1}$  (Ponman et al. 1996). (2) A compact galaxy distribution (4 members within  $1.7'$  diameter) has led to a judgment that the HCG 80 galaxies are accordant members (Arp 1997; Sulentic 1997). (3) Two of the galaxies are classified as Im (table 4.1), which may indicate the galaxy-galaxy interaction in the group.

## 2.9 HCG 62

In order to examine the production process of heavy elements in the intragroup gas, which flowed out of galaxies as a result of star formation of individual galaxy, I analyzed X-ray data for the group of galaxies, HCG 62, which contains an elliptical galaxy in the center. Since bright

elliptical galaxies are known to hold a large amount of heavy elements, they are very important in investigating the history of metal enrichment. HCG 62 is suitable for the abundance analysis, because it is one of the nearest Hickson compact galaxy groups (Hickson et al. 1989) and the brightest group of galaxies in the X-ray band.  $1'$  corresponds to 17.8 kpc at  $z = 0.0145$ . It was observed by both Chandra and XMM-Newton, enabling an analysis in detail with high spatial resolution and with wide field coverage. Moreover, Vrtilik (2001) and Vrtilik et al. (2002) discovered two cavities in HCG 62, based on the high resolution image of Chandra.

The group consists of 63 galaxies (Mulchaey et al. 2003) within a radius of  $50'$  (900 kpc), while the central region is dominated by 4 galaxies. The galaxy distribution is shown in figure 2.12. The extended X-ray emission of HCG 62 was first discovered by Ponman & Bertram (1993) with ROSAT PSPC. Based on the ASCA observation, Fukazawa et al. (2001) detected excess hard X-ray emission (figure 2.8 right), and Finoguenov & Ponman (1999) reported strong central concentration of iron.

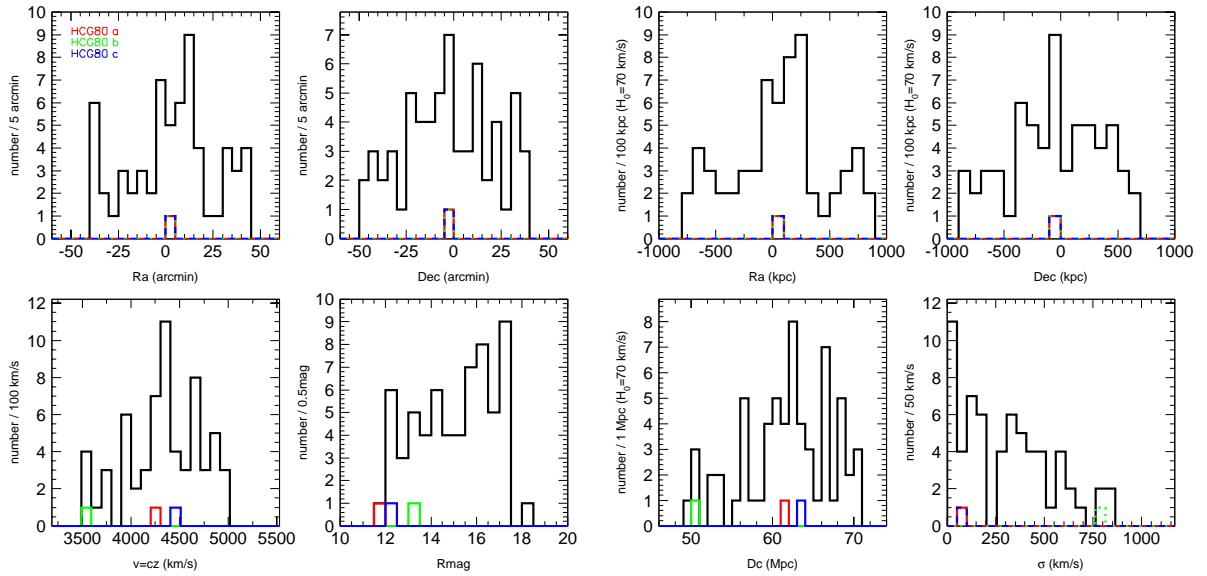


Fig. 2.12: Galaxy distribution of HCG 62. HCG 62a, HCG 62b and HCG 62c are indicated in red, green and blue, respectively.

# Chapter 3

## Instrumentation

### 3.1 Chandra X-ray Observatory

#### 3.1.1 Overview of the Chandra Satellite

*Chandra* was launched on the Space Shuttle Columbia on July 23, 1999. The orbit of the satellite is elliptical with the perigee altitude of 10,000 km, the apogee altitude of 140,000 km. The orbital period is about 64 hours, which is allowing uninterrupted observing intervals of more than 48 hours.

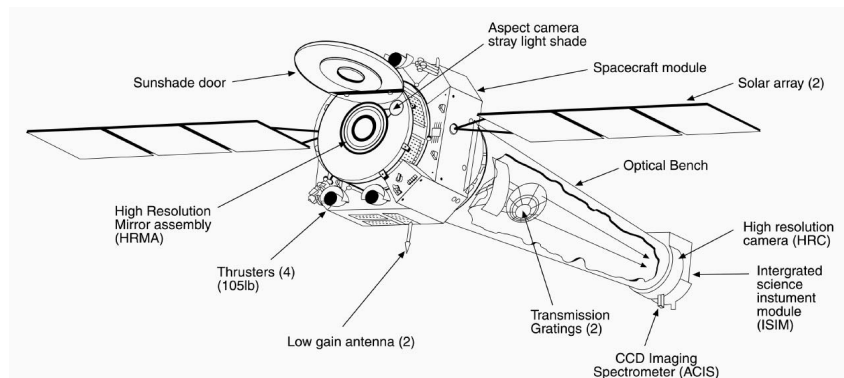


Fig. 3.1: The schematic view of the *Chandra* satellite

The most vivid characteristic of *Chandra* is higher angular resolution than all the previous X-ray satellites. The *Chandra* telescope, “High Resolution Mirror Assembly (HRMA)”, consists of 4 mirrors of Wolter type 1 geometry formed by glass, and achieved the angular resolution of  $0.''5$ . The satellite attitude is controlled and determined by “Pointing Control and Aspect Determination (PCAD)” system with the higher accuracy than angular resolution.

*Chandra* has two focal plane instruments: a microchannel plate, named “High Resolution Camera (HRC)”, and a X-ray CCD camera, “Advanced CCD Imaging Spectrometer (ACIS)”. *Chandra* also has two gratings: “High-Energy Transmission Grating (HETG)”, and “Low-Energy

Transmission Grating”. To protect the instruments from the particle radiation damage, *Chandra* is equipped with a charged-particle detector, the “Electron, Proton, Helium INstrument (EPHIN)”. The schematic view of the satellites is shown in figure 3.1. The detailed properties of the instruments are mentioned in following subsections.

### 3.1.2 High Resolulusion Mirror Assembly (HRMA)

The *Chandra* telescope has four pairs of Wolter Type-I mirrors, which were fabricated from Zerodur glass, polished, and coated with iridium on a binding layer of chromium as figure 3.2. The outer diameters of mirrors are 1.23, 0.99, 0.87, and 0.65 meter, and the focal length is 10.066 meter.

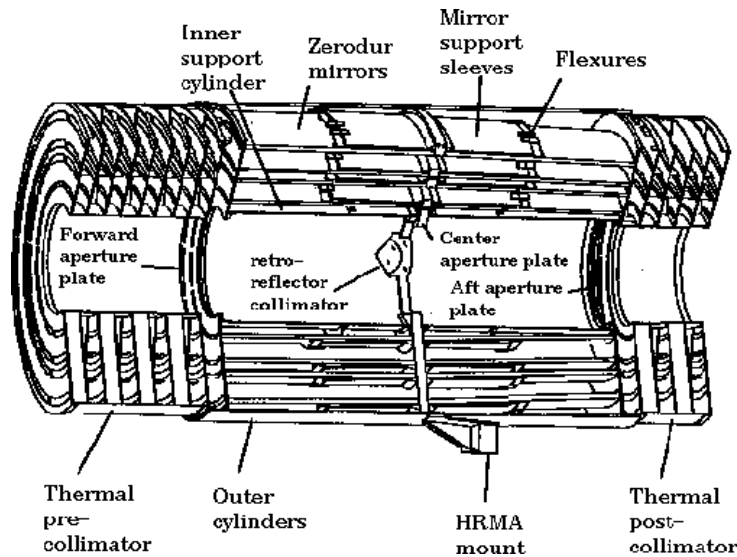
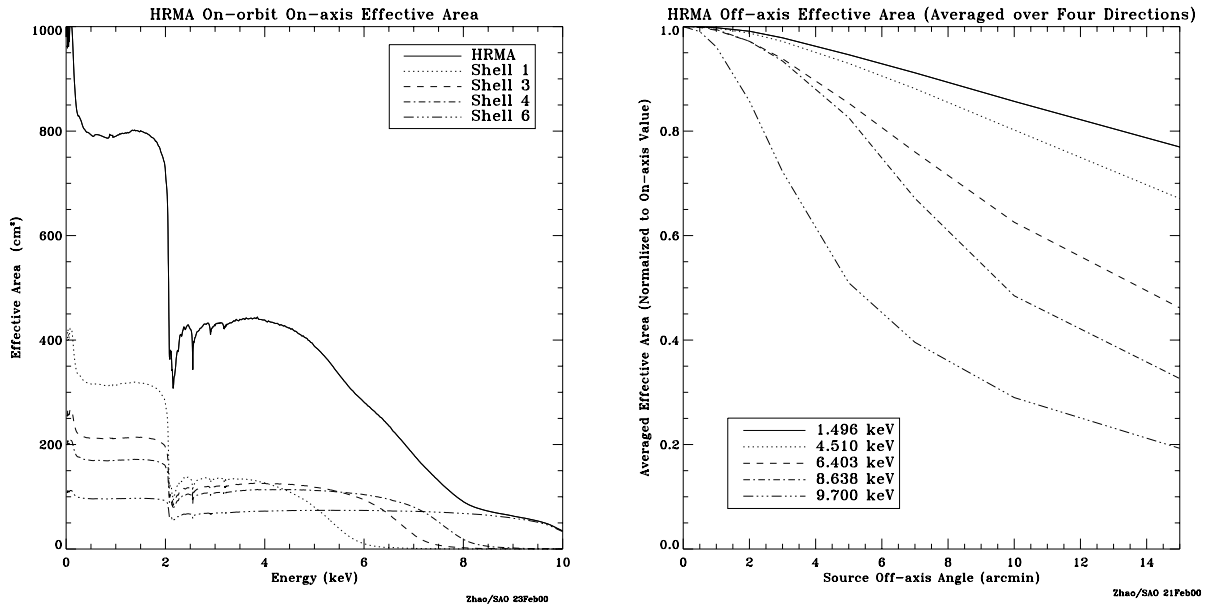


Fig. 3.2: HRMA mirrors

Figure 3.3a, b show the effective area of HRMA in relation to X-ray energy and off-axis angle, respectively. On-axis effective area is about  $800 \text{ cm}^2$  at 0.25 keV, and declines to  $400 \text{ cm}^2$  at 5.0 keV,  $100 \text{ cm}^2$  at 8.0 keV. The effective area also decreases as source position departs from on axis.

The point-spread function (PSF) is very sharp, and most of X-ray photons are collected within  $1''$ -radius region (figure 3.4). The encircled energy function of HRMA is shown in figure 3.5a. At 4.51 keV, the 50% photons are included in about  $0''.35$ -radius, which is called the encircled energy radius. The encircled energy radius increase, or PSF becomes broad, at the larger off-axis angle. Encircled energy radius is shown in figure 3.5b. The diameter, which encircles 50% energy, is called Half Power Diameter (HPD).

The central  $29'$  diameter region of the field of view is free from stray light, because baffles prevent non-reflected or singly reflected X-rays. Then, there is no ghost image.



(a) Effective area vs. X-ray energy

(b) Effective area vs. off-axis angle

Fig. 3.3: The HRMA effective area versus X-ray energy (left; a) and off-axis angle (right; b). In the left panel, shell 1, 3, 4, 6 indicate the mirror layers from outside to inside.

### 3.1.3 Advanced CCD Imaging Spectrometer (ACIS)

The Advanced CCD Imaging Spectrometer (ACIS) is comprised of ten  $1024 \times 1024$  pixel CCDs;  $2 \times 2$  array of ACIS-I (I0–I3) for imaging and  $1 \times 6$  array of ACIS-S (S0–S5) for imaging and grating spectroscopy. The pixels are  $24 \mu\text{m}$  ( $\sim 0''.5$ ) square. Two CCDs (S1 and S3) are back-illuminated (BI) and the others are front-illuminated (FI). The CCD chips of ACIS-I and ACIS-S are tilted to follow the HRMA focal surface and the HETG focal surface, respectively.

ACIS has many observing modes to apply variety observations, but we use only Timed-Exposure mode with the readout time of 3.24 s. X-ray events are extracted by the same way as *ASCA* or grade method. Though grade identification number is different from that of *ASCA*, X-ray events which are equivalent to *ASCA* grade 0, 2, 3, 4, 6 are used in standard analysis.

The quantum efficiency of ACIS is shown in figure 3.6. Low-energy X-rays are largely absorbed by Optical Blocking Filter (OBF) and the gate structure of the CCD chips. Since BI chips have the gate at the opposite side to HRMA, the quantum efficiency of BI CCDs are larger than those of FI CCDs in low-energy band. By the increase of CTI, the quantum efficiency becomes smaller at the farther side from the readout.

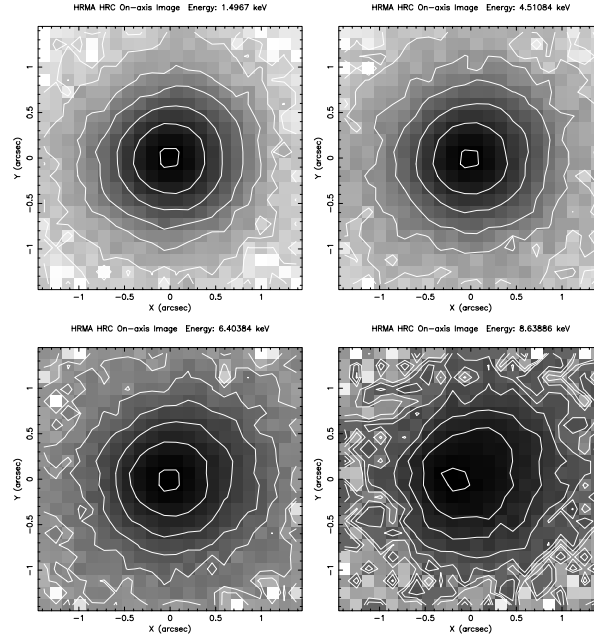
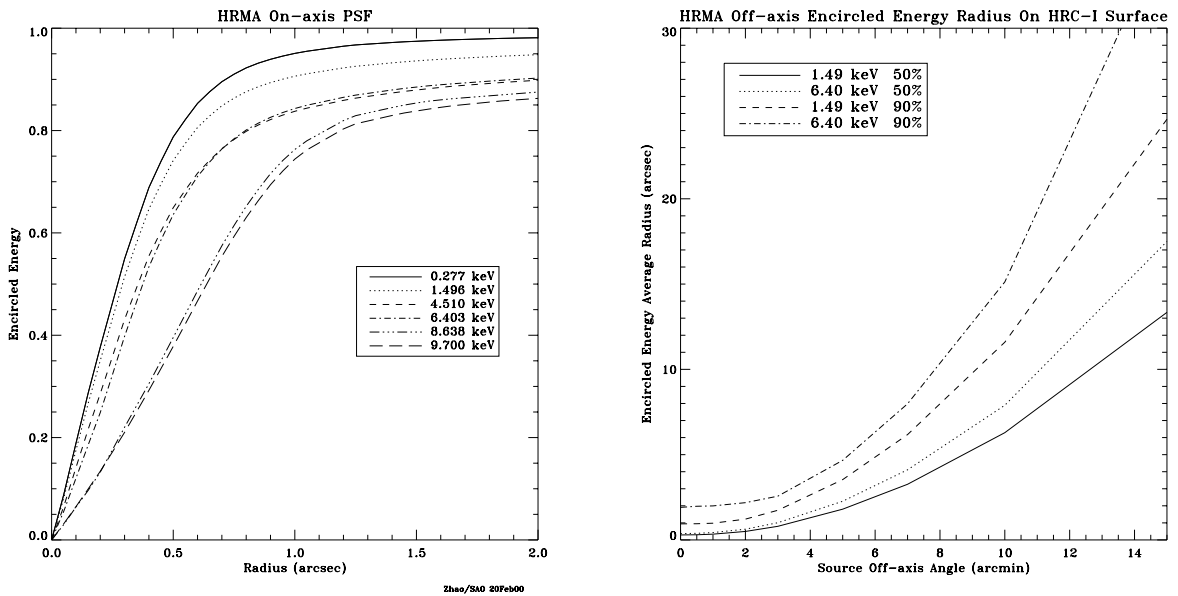


Fig. 3.4: Simulated on-axis images with the energies of 1.49, 4.51, 6.40, and 8.63 keV. Surface brightness contours are logarithmic and spaced in factors of 3. The innermost contour is at 90% of the peak brightness. The 8.6 keV image core is off-center due to the shell misalignment.



(a) Encircled energy function

(b) Encircled energy radius

Fig. 3.5: Encircled energy radius of HRMA

## 3.2 XMM-Newton

### 3.2.1 Overview of the XMM-Newton Satellite

The ESA (European Space Agency) X-ray satellite *XMM-Newton* was launched on 10 December 1999 from Kourou (French Guiana), by the Ariane-V rocket Jansen et al. 2001. It was placed

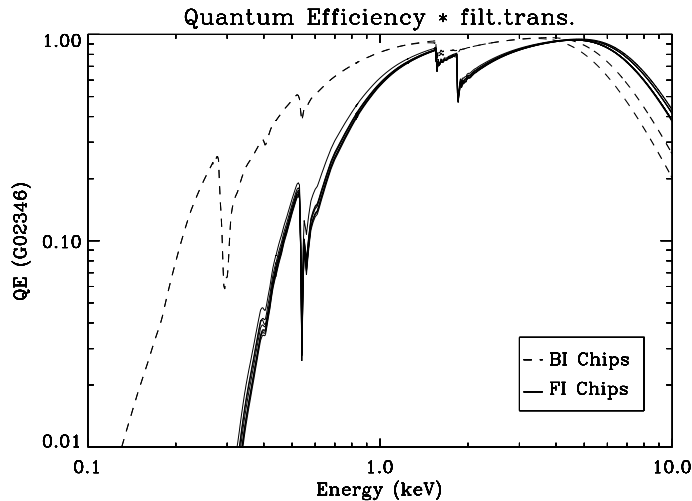


Fig. 3.6: The quantum efficiency of the ACIS CCDs. Note that values are including the transmission rate of the OBF.

into a highly eccentric orbit, with an apogee of about 115,000 km, a perigee of about 6,000 km, and an orbital inclination of  $33^\circ$ , which provides the best visibility in the southern celestial sky. Although the orbital period is 48 hours, the exposure available for scientific data analysis is limited to 39 hours (140 ksec) per orbit. This is because observations are not carried out when the satellite altitude is less than 46,000 km, where the radiation background related to the Earth's magnetosphere is severe.

Table 3.1: Basic performance of the EPIC detectors

	EPIC-MOS	EPIC-pn
Illumination method	Front illuminated	Back illuminated
Pixel size	40 $\mu\text{m}$	150 $\mu\text{m}$
	1.1''	4.1''
Field of view (FOV)	30'	30'
PSF (FWHM/HEW)	5''/14''	6''/15''
Spectral resolution	$\sim 70$ eV	$\sim 80$ eV
Timing resolution	1.5 ms	0.03 ms
Bandpass	0.15-12keV	0.15-15keV

### 3.2.2 X-ray telescope

*XMM-Newton's* three XRTs are co-aligned with an accuracy of better than about 1 arcmin. Each of the three telescopes consists of 58 Wolter type-I mirrors, and the mirror grazing incidence angles range between 17 and 42 arcmin. The focal length is 7.5 m and the diameter of the

largest mirrors is 70 cm. One telescope with the PN camera at the focal point has a light path as shown in Figure 3.7. The two others have grating assemblies in their light paths, diffracting part of the incoming radiation onto their secondary focus (see Figure 3.8). About 44 % of the incoming light focused by the XRT is directed onto the MOS camera at the prime focus, while 40 % of the radiation is dispersed by a grating array onto a linear strip of CCDs. The remaining light is absorbed by the support structures of the RGAs.

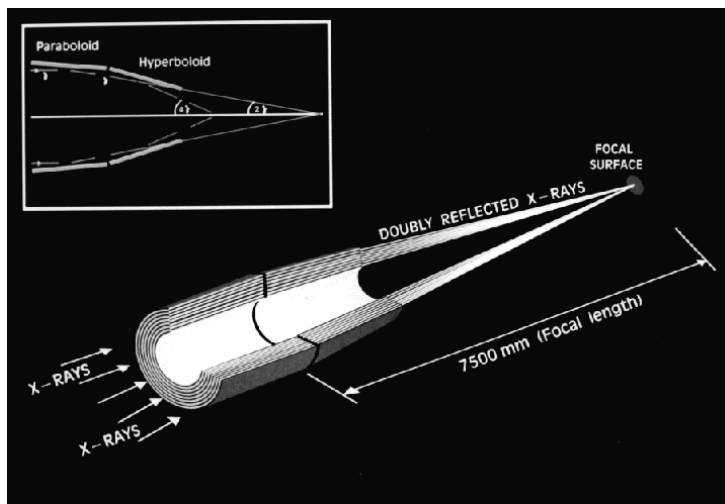


Fig. 3.7: The light path in *XMM-Newton*'s XRT with the PN camera in focus.

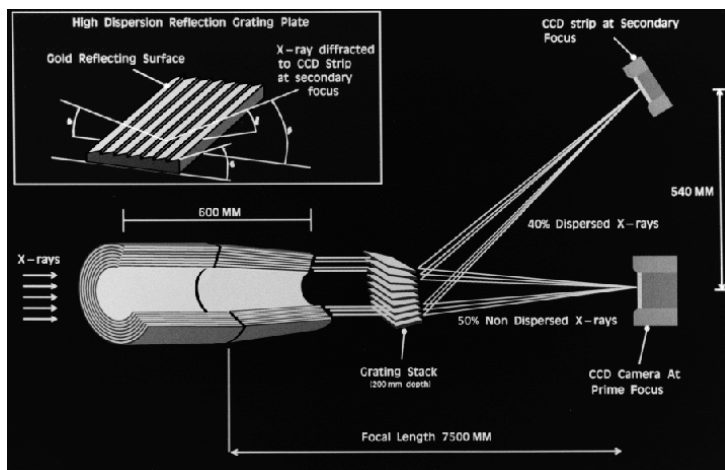


Fig. 3.8: The light path in *XMM-Newton*'s XRT with the MOS camera and RGA.

PSF for *XMM-Newton* is larger than *Chandra*. Figure 3.9 shows the in orbit on-axis images obtained by each detector. The radial substructures are caused by the spiders holding the mirror shells. Figure 3.10 displays the azimuthally averaged profile of the PSF of one XRT together with the best-fit King profile.

An effective area is an indicator of ability of collecting photons. *XMM-Newton* carries the XRT

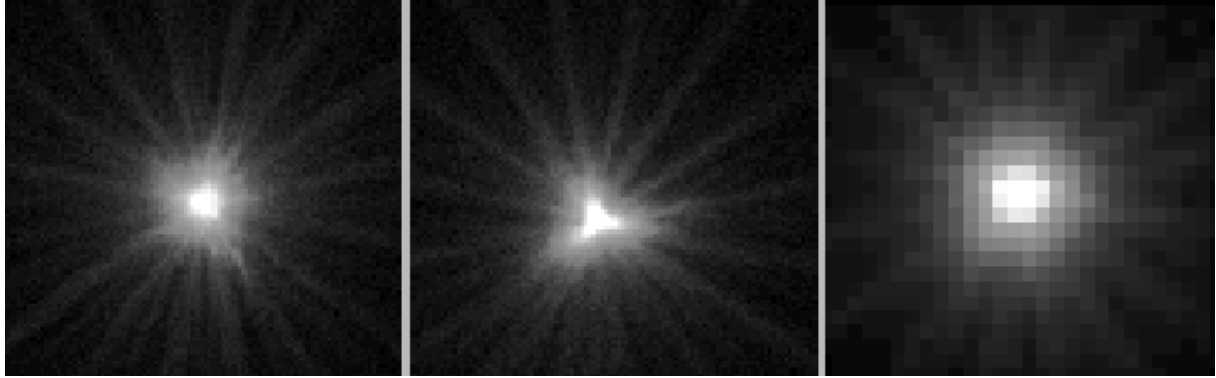


Fig. 3.9: On-axis images of the MOS1, MOS2 and PN XRTs (left to right). The images are 110 arcsec wide and a logarithmic scale has been used to visualize the wings of the point spread function.

with the largest effective area of focusing telescope ever. The total mirror geometric effective area (EA) at 1.5 keV energy is about 1,550 cm<sup>2</sup> for each telescope, i.e., 4,650 cm<sup>2</sup> in total. Figure 3.11 shows the on-axis effective area of all *XMM-Newton* XRTs. The EAs of the two MOS cameras are lower than that of the pn, because only part of the incoming radiation falls onto these detectors, which are partially obscured by the RGAs (see Figure 3.8).

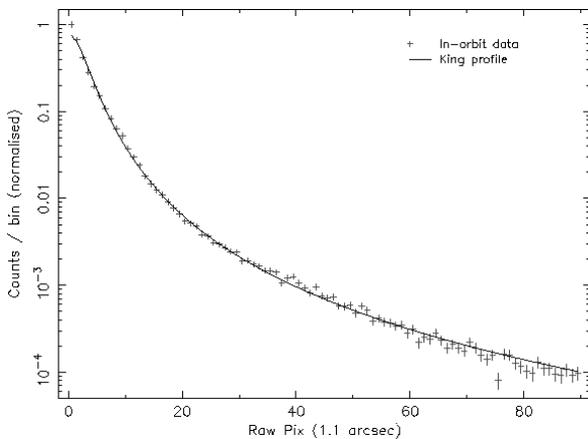


Fig. 3.10: Radial counts distribution for the on-axis PSF of the MOS1 XRT in the 0.75–2.25 keV energy range. The solid line indicates the best-fit King profile.

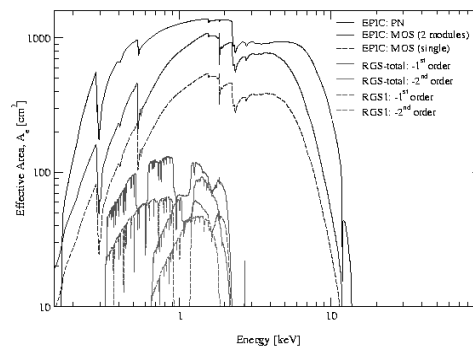


Fig. 3.11: The net effective area of all *XMM-Newton* XRT, combined with the response characteristics of the focal detectors.

### 3.2.3 European Photon Imaging Camera (EPIC)

Two of *XMM-Newton*'s X-ray telescopes are equipped with EPIC MOS (Metal Oxide Semiconductor) CCD arrays, the third carries a different CCD camera called EPIC PN. The EPIC

cameras offer the possibility to perform extremely sensitive imaging observations over a field of view of 30 arcmin and the energy range from 0.15 to 15 keV, with moderate spectral ( $E/\Delta E \sim 20\text{--}50$ ) and angular resolution (15 arcsec HEW). The detector layout and the baffled X-ray telescope FOV of both types of EPIC cameras are shown in Figure 3.12. The PN chip array is slightly offset with respect to the optical axis of its X-ray telescope so that the nominal, on-axis observing position does not fall on the central chip boundary. This ensures that more than 90 % of the energy of an on-axis point source are collected on one PN CCD chip. Two EPIC MOS cameras are rotated by  $90^\circ$  with respect to each other. The dead spaces between the MOS chips are not gaps, but unusable areas due to detector edges (the MOS chip physically overlap each other, the central one being located slightly behind the ones in the outer ring). All EPIC cameras are operated in photon counting mode with a fixed, mode dependent frame read-out frequency.

**Comparison of focal plane organisation of EPIC MOS and pn cameras**

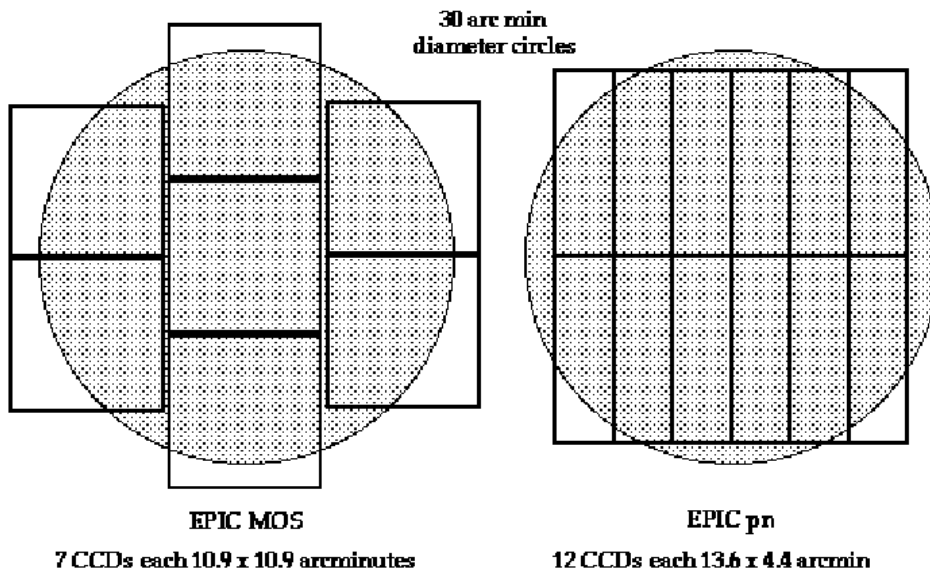


Fig. 3.12: A rough sketch of the field of view of the two types of EPIC cameras (MOS, left; PN, right). The shaded circle depicts a 30 arcmin diameter area which is equivalent with the XRT field of view.

### 3.3 Compare Chandra with XMM-Newton

*Chandra* is higher angular resolution than all the previous X-ray satellites, while *XMM-Newton* covers the wider field of view of  $r \leq 15'$  than *Chandra*, and carries the XRT with the largest effective area of focusing telescope ever as figure 3.13a. The intrinsic background of *XMM-Newton* is lower than *Chandra*, however, we need to note the energy range around the Al- $K_\alpha$  line (1.4867 keV) as shown figure 3.13b.

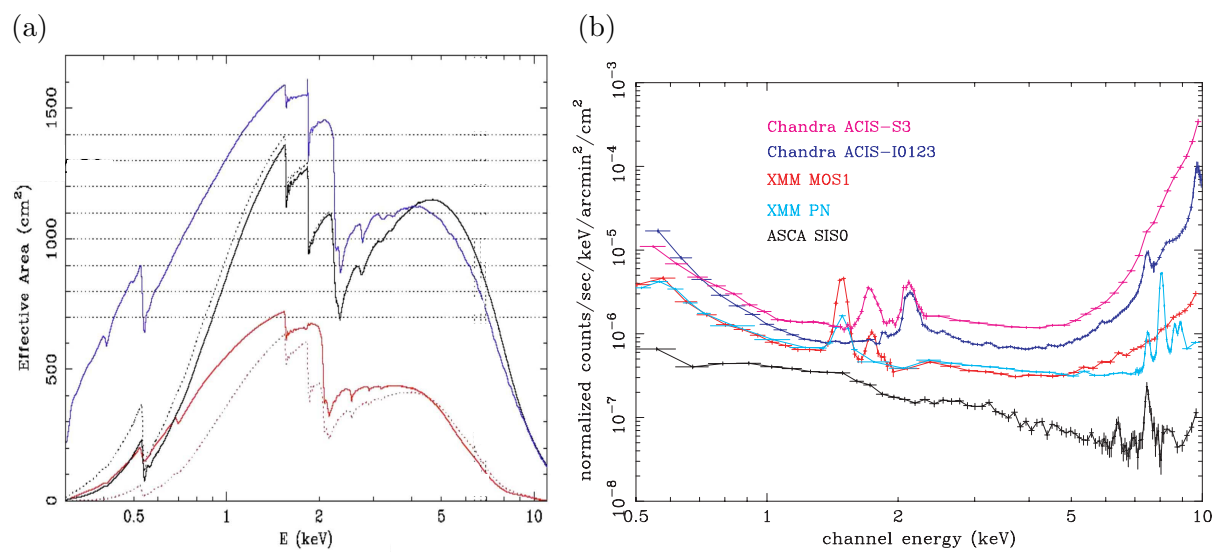


Fig. 3.13: (a) *XMM-Newton* (blue) and *Chandra* (red) effective areas. (b) *XMM-Newton* (red: MOS, cyan: pn) and *Chandra* (magenta) background spectra normalized by effective area by Katayama et al. 2004.



# Chapter 4

## HCG 80

In this section, we present a Chandra observation of a spiral-only group of galaxies, HCG 80. This is organized as follows. In the § 4.1, we describe the Chandra observation of a galaxy group, HCG 80. In the § 4.3, we describe source detection of a galaxy group, HCG 80 in the Chandra field. In § 4.4, 4.5, and 4.6, we present spatial and spectral analyses of HCG 80 member galaxies. In § 4.7, we exclude them from the group region and constrain the X-ray emission from the hot intragroup gas.

From § 4.8.1, we discuss the properties of the member galaxies and, in particular, the nature of the extended halo emission discovered in the brightest member of the group. We then discuss possible reasons for the absence of the strong X-ray emission from the intragroup gas of HCG 80. We compare the X-ray luminosity of the member galaxies to those of the optical in § 4.8.1, and further discuss the origin of the halo emission from HCG 80a in § 4.8.2. On the other hand, we found that there is no significant emission from the group region. The absence of strong X-ray emission is discussed in § 4.9.

### 4.1 Chandra Observation of HCG 80

The group of galaxies HCG 80 consists of four late-type galaxies, HCG 80a–d, as shown in table 4.1 and figure 4.1. Their optical properties are also summarized in table 4.1. We observed HCG 80 with the Chandra Advanced CCD Imaging Spectrometer (ACIS-S) detector on 2003 August 18 (PI: N. Ota). The pointing coordinates were  $15^{\text{h}}59^{\text{m}}12^{\text{s}}30$ ,  $+65^{\circ}13'33''0$  (J2000), and the target was offset from the ACIS-S nominal aim point with a Y-offset of  $-1'$ . The CCD temperature was  $-120^{\circ}\text{C}$ .

### 4.2 Data Reduction

The data reduction was performed using CIAO version 3.0.2 with CALDB version 2.25. We analyzed the light curve, and showed that there is no period of a high background level exceeding  $3\sigma$  above the mean quiescent background rates. Thus, the net exposure time is 19712 s. We did

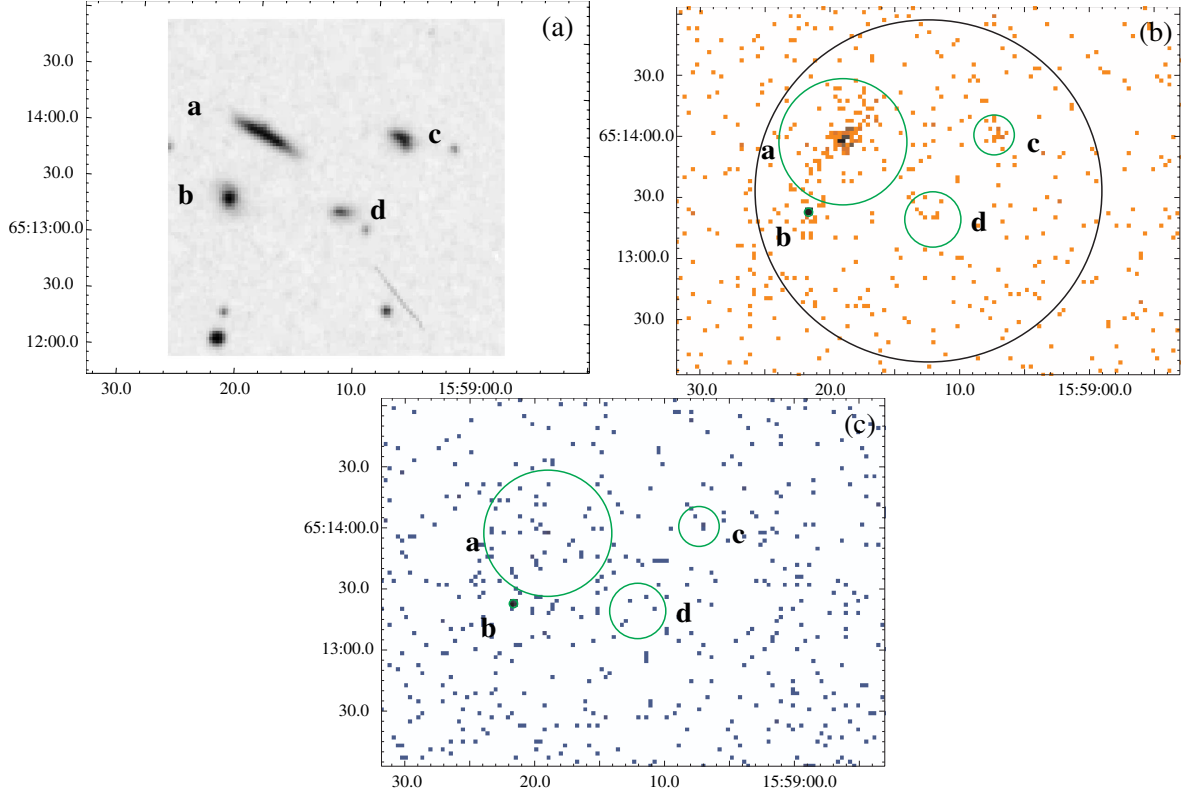


Fig. 4.1: Optical and X-ray images of the spiral-only group HCG 80. In the panel (a), the DSS image of the HCG 80 group is shown, where the four members are denoted by a–d. In panels (b) and (c), the Chandra X-ray images in the 0.5–2 keV and 2–7 keV bands are shown. The X-ray images are not smoothed, and are background inclusive. The image pixel size is  $2'' \times 2''$ . The member galaxies, HCG 80a–d, are indicated by green circles of radii  $r = 31''$ ,  $2''$ ,  $9.8''$ , and  $13.6''$ , respectively. In panel (b), the black color represents pixels with an X-ray surface brightness higher than 10 photons per image pixel. The group region used to constrain the diffuse emission in subsection 4.7 is shown with a circle of radius  $84''$ .

Table 4.1: Optical properties of member galaxies.

Object	Optical coords. (J2000) <sup>*</sup>		$z$	Diameters <sup>†</sup>	$B^{\ddagger}$ [mag]	Type
	RA	Dec.				
HCG 80	$15^{\text{h}}59^{\text{m}}12^{\text{s}}.4$	$+65^{\circ}13'33''.3$	0.02990			Group
HCG 80a	$15^{\text{h}}59^{\text{m}}19^{\text{s}}.0$	$+65^{\circ}13'57''.4$	0.02994	$50.8 \times 10.8$	15.66	Sd
HCG 80b	$15^{\text{h}}59^{\text{m}}21^{\text{s}}.5$	$+65^{\circ}13'22''.7$	0.03197	$20.4 \times 17.4$	16.37	Sa
HCG 80c	$15^{\text{h}}59^{\text{m}}07^{\text{s}}.3$	$+65^{\circ}14'00''.8$	0.03186	$19.6 \times 16.4$	16.06	Im
HCG 80d	$15^{\text{h}}59^{\text{m}}12^{\text{s}}.1$	$+65^{\circ}13'19''.3$	0.03038	$27.2 \times 10.8$	17.01	Im

<sup>\*</sup>Optical coordinates of the object from Hickson et al. (1989).

<sup>†</sup> Major axis [arcsec]  $\times$  minor axis [arcsec].

<sup>‡</sup> B magnitude.

Table 4.2: X-ray count rates, fluxes, and hardness ratios for member galaxies.

HCG	$R_{\text{spec}}[*]$	$R_{\text{max}}[\dagger]$	Soft band		Hard band		$HR[**]$
			$S[\ddagger]$	$f_{\text{X,S}}[\S]$	$H[\llbracket]$	$f_{\text{X,H}}[\#]$	
80a	25	31	$65.9 \pm 6.4$	$3.4 \pm 0.3$	$5.8 \pm 3.5$	$0.7 \pm 0.4$	$0.09 \pm 0.05$
80a, nucleus	–	2	$14.7 \pm 2.7$	$0.7 \pm 0.1$	$3.5 \pm 1.3$	$0.6 \pm 0.2$	$0.24 \pm 0.10$
80a, disk+halo	–	31 – 2	$50.3 \pm 5.8$	$2.6 \pm 0.3$	$2.9(< 6.1)$	$0.3(< 0.7)$	$0.06 \pm 0.06$
80b, nucleus	1.5	2	$107.0 \pm 7.4$	$5.3 \pm 0.4$	$34.9 \pm 4.2$	$6.2 \pm 0.7$	$0.33 \pm 0.05$
80b, disk	–	10 – 2	$6.2 \pm 1.9$	$0.2 \pm 0.1$	$0.4(< 1.4)$	$0.04(< 0.15)$	$0.06(< 0.23)$
80c	–	9.8	$5.6 \pm 1.9$	$0.2 \pm 0.1$	$0.3(< 1.3)$	$0.04(< 0.15)$	$0.06(< 0.24)$
80d	–	13.6	$1.7(< 3.2)$	$0.06(< 0.13)$	$< 2.7$	$< 0.05$	$1.6 \pm 1.4$

[\*] The spectral extraction radius in arcsec (see subsection 4.6).

[†] The maximum radius in arcsec, used to estimate the counting rate,  $S$  and  $H$ , and the hardness ratio,  $HR$ .

[‡] The X-ray counting rate in the 0.5–2 keV band,  $S$  [ $10^{-4}$  counts  $\text{s}^{-1}$ ].

[§] The X-ray flux in the 0.5–2 keV band,  $f_{\text{X,S}}$  [ $10^{-14}$  erg  $\text{s}^{-1}$   $\text{cm}^{-2}$ ].

[||] The X-ray counting rate in the 2–7 keV band,  $H$  [ $10^{-4}$  counts  $\text{s}^{-1}$ ].

[#] The X-ray flux in the 2–7 keV band,  $f_{\text{X,H}}$  [ $10^{-14}$  erg  $\text{s}^{-1}$   $\text{cm}^{-2}$ ].

[\*\*] The hardness ratio,  $HR = H/S$ .

The quoted errors are the  $1\sigma$ .

not find any astrometry offset for the data. Since the data were taken with the VFAINT mode, the particle background was reduced by screening out events with significant flux in border pixels of the  $5 \times 5$  event islands.

### 4.3 Source Detection in the ACIS-S3 Field

We searched for X-ray sources in the ACIS-S3 field of view with the wavedetect algorithm with a significance parameter of  $10^{-6}$  utilizing the 0.3–10 keV band image, and detected 20 in total, including HCG 80a and HCG 80b. We also found significant X-ray emission from the direction of HCG 80c. The counting rates of four member galaxies are summarized in table 4.2. In the following analysis, the detected point sources were excluded with a radius of 7-times the size of the Point Spread Function (PSF), which is defined as the 40% encircled energy radius at 1.5 keV at the source position.

The X-ray maximum positions of HCG 80a and b in the ACIS-S3 image are ( $15^{\text{h}}59^{\text{m}}18^{\text{s}}.9$ ,  $+65^{\circ}13'57''.3$ ) and ( $15^{\text{h}}59^{\text{m}}21^{\text{s}}.6$ ,  $+65^{\circ}13'22''.8$ ), respectively. Comparing these with the optical coordinates from Hickson et al. 1989, they are consistent within  $\lesssim 1''$ . However, due to the limited photon statistics of the present X-ray data, there are uncertainties in the X-ray positions of the galaxies. We thus assumed the optical positions from Hickson et al. 1989 as their centers in our analysis.

## 4.4 X-Ray Morphologies of Member Galaxies

As shown in table 4.2, because HCG 80a and b were detected with more than  $10\sigma$  significance, we performed detailed analyses of the surface brightness distributions and energy spectra for those two galaxies. Since the significance of the X-ray emission from HCG 80c and d are low ( $2.6\sigma$  and  $\lesssim 2\sigma$  in the soft band, respectively), we could only measure the fluxes (and luminosities under the assumptions of the spectral models). The results of flux estimations for the four member galaxies are also presented in table 4.2.

In order to constrain the spatial distribution of the X-ray emission from HCG 80a and b, we investigated the surface brightness distribution in two different ways: (1) a radial profile fitting and (2) a 1-dimensional profile fitting. In the former analysis, we compared the X-ray radial profile with the simulated PSF to constrain the emission from a nuclear source and the presence of diffuse emission. Since we found significant extended emission, particularly from HCG 80a, we studied the spatial distribution in detail in a latter analysis. We corrected the positional dependence of the telescope and the detector responses with exposure maps.

In the case of (1), we produced soft (0.5–2 keV) and hard (2–7 keV) band images and calculated the radially averaged surface brightness distributions centered at HCG 80a and b, as shown in figure 4.2. We fitted them separately with the PSF models, which were created by the HRMA PSF simulator, ChaRT, while specifying the locations of the sources and the spectral models derived from the spectral analysis (subsection 4.6). The PSF models were generated with sufficient photons so that the statistical uncertainty would be less than 10%, thus negligible compared to the Poisson error of the present data. We investigated the positional dependence of the background intensity using both the blank-sky data and the present data, to find that the background can be regarded as being constant within the statistical errors. The background intensities were then estimated from the  $84'' < r < 160''$  ring region of the present pointing data to be  $(4.73 \pm 0.20) \times 10^{-7}$  and  $(5.31 \pm 0.21) \times 10^{-7}$  counts  $\text{s}^{-1}$   $\text{arcsec}^{-2}$  in the soft and hard bands, respectively (the errors are  $1\sigma$ ), and included as fixed constants in the fits.

### 4.4.1 HCG 80a

For HCG 80a, there is clearly an extended emission, particularly in the soft energy band compared with the PSF (figure 4.2a). We then evaluated the emission using the Gaussian functions to find that the single-component Gaussian model can not sufficiently fit the data, suggesting that at least two components are necessary to describe them. Thus, in figure 4.2a, we show the best-fit model consisting of the PSF and two Gaussians, where the diffuse emission is seen out to the maximum radius of  $R_{\text{max}} \sim 31''$  above the  $2\sigma$  background level. We analyze the significance of the emission components and the properties in more detail later.

In the hard energy band, there is excess emission over the background within  $2''$  from the HCG 80a optical center. The 2–7 keV counting rate is  $(3.5 \pm 1.3) \times 10^{-4}$  counts  $\text{s}^{-1}$ . Under the current statistics, we could not constrain the spatial distribution. However, taking into

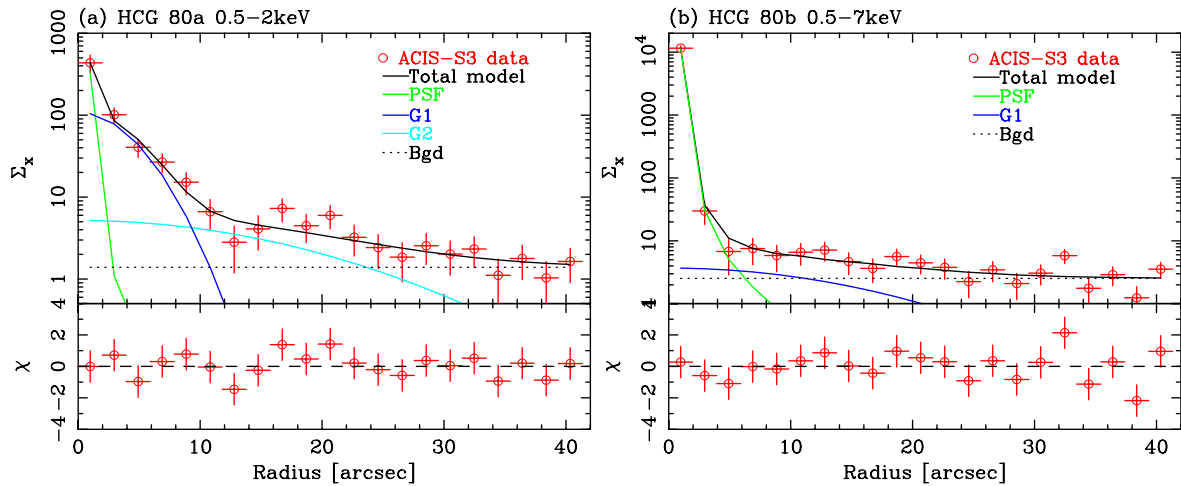


Fig. 4.2: Radial profile fitting for HCG 80a and b with the PSF and Gaussian(s) models. In panels (a) and (b), the ACIS-S3 radial surface brightness distribution for HCG 80a in the 0.5–2 keV and HCG 80b in the 0.5–7 keV are indicated by red crosses. The best-fit total model is shown with the black solid line in each panel, where the PSF and Gaussian components representing the disk and halo emissions are also indicated by the green, blue, and light-blue lines. The background intensity is indicated by the horizontal dotted line. In the upper panels  $\Sigma_X$  is in units of  $10^{-9}$  photons  $s^{-1} cm^{-2} arcsec^{-2}$ , while in the bottom panels the residuals of the fits are shown in units of  $\sigma$ .

account the spectral hardness inferred from the analysis in subsection 4.5 and the nuclear activity reported by Shimada et al. 2000a, we suggest that the hard emission may be attributed to the central AGN in HCG 80a.

In the next step, we consider the soft diffuse emission from HCG 80a, based on a 1-dimensional profile fitting. Since the galaxy has a nearly edge-on inclination of  $i = 86^\circ$ , following Rubin et al. 1982 (see also Nishiura et al. 2000), the emission from the halo region is expected to be clearly resolved. From figure 4.1b, we find that the emission extends nearly along the perpendicular direction from the galactic disk of HCG 80a, whose position angle is  $64^\circ$  Shimada et al. 2000a. We thus extracted the 1D surface brightness profile along the minor axis of the galaxy, accumulated within  $|r| < 24''$  of the major axis (figure 4.3a). The minor-axis profile was rebinned by a factor of 6; thus, each bin is  $3''$ . We carried out a  $\chi^2$  fitting with some simple models consisting of the Gaussian components for the diffuse emission and the PSF for the central emission, whose centers are fixed at the HCG 80a center position. As a result, neither the single Gaussian nor the PSF model could provide an acceptable fit; however, by adding another Gaussian component, the fit was significantly improved at the 95% level by the F-test. We show the results for the cases of Model 1 [equation (4.1)] and Model 2 [equation (4.2)] in table 4.3.

$$\Sigma_X = \Sigma_{\text{PSF}} + \Sigma_{\text{G1},0} e^{-(y-y_0)^2/\sigma_{\text{G1}}^2}, \quad (4.1)$$

$$\Sigma_X = \Sigma_{\text{G1},0} e^{-(y-y_0)^2/\sigma_{\text{G1}}^2} + \Sigma_{\text{G2},0} e^{-(y-y_0)^2/\sigma_{\text{G2}}^2}, \quad (4.2)$$

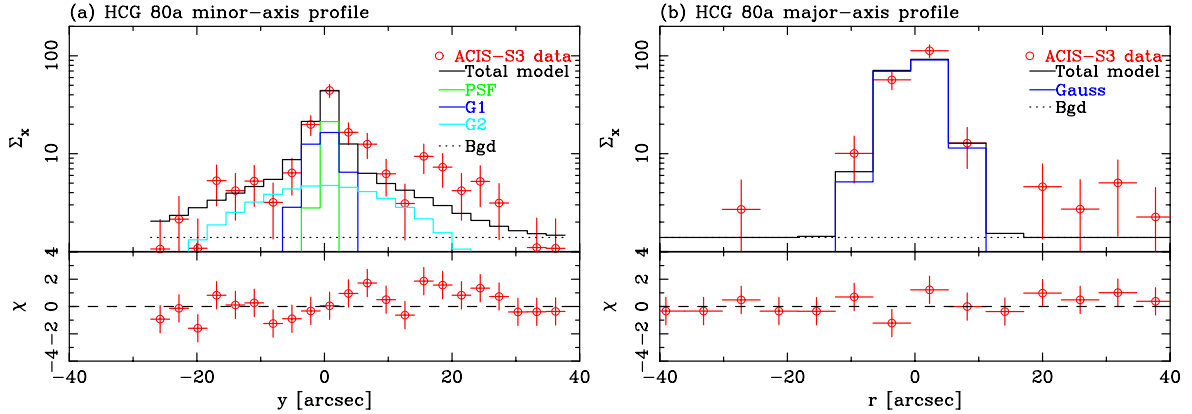


Fig. 4.3: Minor-axis and major-axis X-ray surface brightness distributions. In the panels (a) and (b), the crosses denote the observed 1-dimensional surface brightness profiles accumulated within  $|r| < 24''$  of the major axis and  $|y| < 5''$  of the minor axis in the soft band, respectively. The surface brightness,  $\Sigma_X$ , is in units of  $10^{-9}\text{photons s}^{-1}\text{cm}^{-2}\text{arcsec}^{-2}$ . In the panel (a), the solid black line shows the result of the fitting with Model 3. The PSF, narrow Gaussian, broad Gaussian, and background components are indicated by the green, blue, light-blue, and dotted black lines, respectively. In the panel (b), the solid black, blue, and dotted lines show the best-fit total model, Gaussian and the background components, respectively.

Table 4.3: Results of the 1D fitting for HCG 80a in the soft band.

Parameter	Model 1 PSF+G1	Model 2 G1+G2	Model 3 PSF+G1+G2
PSF [ $\text{photons s}^{-1}\text{cm}^{-2}$ ]	$43_{-14}^{+13} \times 10^{-9}$	–	$25(< 45) \times 10^{-9}$
$\Sigma_{G1,0}$ [ $\text{photons s}^{-1}\text{cm}^{-2}\text{arcsec}^{-2}$ ]	$7.6_{-2.8}^{+5.2} \times 10^{-9}$	$36.4_{-12.6}^{+19.5} \times 10^{-9}$	$17.2_{-12.4}^{+31.7} \times 10^{-9}$
$\sigma_{G1}$ [arcsec]	$10 \pm 4$	$2 \pm 1$	$3_{-1}^{+2}$
$\Sigma_{G2,0}$ [ $\text{photons s}^{-1}\text{cm}^{-2}\text{arcsec}^{-2}$ ]	–	$5.6_{-2.8}^{+3.8} \times 10^{-9}$	$4.7_{-2.8}^{+3.5} \times 10^{-9}$
$\sigma_{G2}$ [arcsec]	–	$12_{-4}^{+6}$	$12_{-4}^{+8}$
$\chi^2/\text{dof}$	26.2/19	22.7/18	20.6/17

$$\Sigma_X = \Sigma_{\text{PSF}} + \Sigma_{G1,0} e^{-(y-y_0)^2/\sigma_{G1}^2} + \Sigma_{G2,0} e^{-(y-y_0)^2/\sigma_{G2}^2}, \quad (4.3)$$

where  $y_0$  is fixed at the center of HCG 80a, and we assume  $\sigma_{G1} < \sigma_{G2}$ . We also fit the profile with Model 3 [equation (4.3)] and examine the significance of the emission from the central point source. Although the low photon statistics in the central emission resulted in no significant improvement over Model 2 in the F-test at the 95% confidence, we adopt Model 3 in the rest of our analysis regarding the presence of the optically identified AGN Shimada et al. 2000a and the observed high hardness ratio in subsection 4.5.

From the fitting with Model 3, the width for the narrow Gaussian component was obtained to

be  $\sigma_{G1} = 3_{-1}^{+2}$  arcsec ( $= 1.8_{-0.6}^{+1.2}$  kpc), which is very consistent with the optical scale of the galactic disk. The broad Gaussian component has a width of  $\sigma_{G2} = 12_{-4}^{+8}$  arcsec ( $= 7.2_{-2.4}^{+4.8}$  kpc), and thus largely extends compared to the disk scale. Accordingly, we refer to the narrow and broad Gaussian components, respectively, as the “disk” and “halo” components hereafter. The extent of the halo emission detected above the  $2\sigma$  background level is  $-26'' < y < 26''$ , corresponding to 31.2 kpc in total. The origin of this huge X-ray halo is discussed in section 4.8.1.

We estimated the luminosity of each component assuming the MEKAL model with an average temperature of 0.56 keV for the disk and the halo, and a power-law model with  $\Gamma = 2.0$  for the nucleus. Here, the same definitions as those of Strickland et al. 2004a are used to define the emission regions for the nuclear (N), disk (D), and halo(H) components. Namely the luminosities ( $L_{X,N}$ ,  $L_{X,D}$ , and  $L_{X,H}$ ) are accumulated from the  $r < 1$  kpc circle, a rectangular aperture oriented along the minor axis of major-axis length 28.9 kpc and extending between  $-2 \text{ kpc} < y < 2 \text{ kpc}$ , and a  $28.9 \text{ kpc} \times 39.1 \text{ kpc}$  rectangular aperture oriented along the minor axis with excluding the N and D regions. We obtained  $L_{X,D} = 2.2 \times 10^{40} \text{ erg s}^{-1}$ ,  $L_{X,H} = 3.8 \times 10^{40} \text{ erg s}^{-1}$ , and  $L_{X,N} = 1.7 \times 10^{40} \text{ erg s}^{-1}$  in the 0.5–2 keV, respectively. The results are also given in table 4.5.

We also notice that the intensity of the halo emission from the Northern hemisphere is stronger than that of the Southern by a factor of  $\sim 2.7 \pm 2.1$  if we fit the Northern and Southern halos separately with Model 3 while fixing the model parameters, except for  $\Sigma_{G2,0}$  at the best-fit values derived in the above analysis. Thus, there may be some asymmetry. However, because the current statistics is limited, we could not further constrain the spatial distribution of the halo emission.

We show the major-axis profile accumulated within  $|y| < 5''$  of the minor axis in figure 4.3b. It could be fitted by a Gaussian with  $\sigma = 4 \pm 1$  arcsec ( $= 2.4 \pm 0.6$  kpc) and a normalization for the central surface brightness of  $108_{-27}^{+49} \times 10^{-9} \text{ photons s}^{-1} \text{ cm}^{-2} \text{ arcsec}^{-2}$ . We found that the width is close to that of the narrow component in Model 3, namely  $\sigma \sim \sigma_{G1}$ . Thus, the disk emission is concentrated within about  $3.5''$  from the center, while we did not find significant emission extending over the optical scale of the galactic disk.

#### 4.4.2 HCG 80b

From a comparison to the simulated PSFs, we found that the innermost data points of the radial surface brightness distributions are well consistent with the PSFs in both the soft and hard energy bands, and resultant  $\chi^2$  values of 24.6 and 34.4 for 20 degrees of freedom. However, we found that there are systematic residuals over the PSFs in several consecutive bins around  $r \sim 10''$ , which can be attributed to the extra emission around the point source. Because the emission is found within a radius roughly corresponding to the size of the optical disk,  $\sim 10''$ , we refer to it as the disk component, while referring to the central point source as the nucleus component hereafter. The photon counts coming from the disk component in a radius range of

$2'' < r < 10''$  are  $12 \pm 4$  and  $< 3$ , in the soft and hard bands, respectively (see also table 4.2).

In order to further constrain the emission profile, we attempted to fit the 0.5–7 keV radial profile with the PSF plus Gaussian model, as shown in figure 4.2. This provided an acceptable fit with  $\chi^2/\text{dof} = 19.3/18$ , and the PSF intensity was obtained as  $(1.13 \pm 0.17) \times 10^{-5}$  photons  $\text{s}^{-1}\text{cm}^{-2}$ ; the Gaussian normalization and the width are  $3.5_{-2.6}^{+3.5} \times 10^{-9}$  photons  $\text{s}^{-1}\text{cm}^{-2}\text{arcsec}^{-2}$  and  $12_{-5}^{+7}$  arcsec ( $= 7_{-3}^{+4}$  kpc), respectively. Because the model parameters are associated with large uncertainties, the emission profile, particularly for the diffuse emission, is not well constrained, which we consider as being due to the low signal-to-noise ratios at the outer radius. We therefore decide to fix the maximum radius at the size of the optical disk,  $R_{\text{max}} = 10''$ , when evaluating the X-ray intensities for the disk emission. Within  $2''$  from the HCG 80b peak, the central nuclear component dominates the total emission, and we use the maximum radius of  $R_{\text{max}} = 2''$  for the HCG 80b nucleus. The luminosities of the nucleus ( $r < 2''$ ) and the disk ( $2'' < r < 10''$ ) were estimated to be  $(2.9 \pm 0.2) \times 10^{41}$  erg  $\text{s}^{-1}$  and  $(5.8 \pm 1.8) \times 10^{39}$  erg  $\text{s}^{-1}$  in the 0.5–7 keV band assuming a power-law model with  $\Gamma = 1.9$  (see subsection 4.6) and the MEKAL model with  $kT = 0.5$  keV and  $Z = 0.1$  solar, respectively.

## 4.5 Hardness Ratio Analysis

To provide a quantitative evaluation of the spatial variation of the X-ray spectra, the hardness ratios for the central and the surrounding disk (+ halo) regions are given in table 4.2. We define the hardness ratio as  $HR \equiv H/S$ , where  $S$  and  $H$  are the photon counts in the 0.5–2 and 2–7 keV bands, respectively. Due to the low significance of the emission from HCG 80c and d, we give the values derived for the entire galaxy regions for these two galaxies. There is an indication that the HCG 80a central emission ( $r < 2''$ ) is hard compared with the outer ( $2'' < r < 31''$ ) region. If we simply assume the spectra as being described by a power-law (or the  $Z = 0.1$  solar MEKAL) model attenuated by Galactic absorption, the power-law indices (or the gas temperature) for the nucleus and the disk + halo regions of HCG 80a correspond to  $\Gamma = 2.2 \pm 0.4$  ( $kT = 2.6 \pm 1.4$  keV) and  $\Gamma = 3.5 (> 2.8)$  ( $kT = 1.0 (< 1.4)$  keV), respectively. While the HCG 80b nucleus region ( $r < 2''$ ) shows a large  $HR$  value, corresponding to a power-law index of  $1.9 \pm 0.2$ , the  $HR$  for the outer disk region ( $2'' < r < 10''$ ) was not constrained. In the next subsection we explore the spectra from the HCG 80a “nucleus + disk + halo” and the HCG 80b “nucleus” regions based on thermal and/or non-thermal spectral modeling to constrain their origins.

Strickland et al. 2004a suggested, based on the Chandra data for ten star-forming galaxies, that the disk emission tends to be harder than the halo emission; however, we did not find any meaningful  $HR$  variation between the two regions in HCG 80a due to the poor photon statistics of the present data.

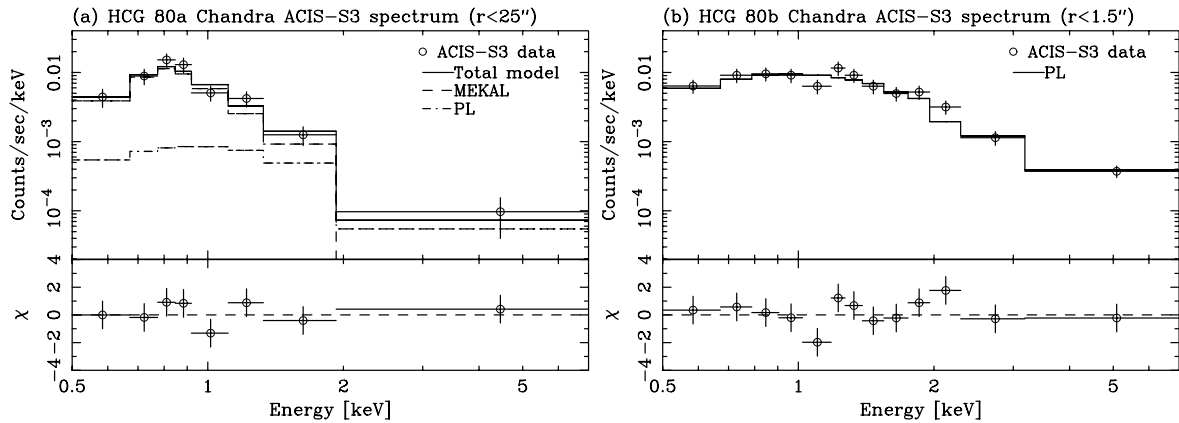


Fig. 4.4: Chandra ACIS-S3 spectra of HCG 80a (a) and HCG 80b (b). In the upper panels, the open circles denote the observed spectra and the step functions show the best-fit spectral models (the MEKAL+Power-law model for HCG 80a and the Power-law model for HCG 80b) convolved with the telescope and the detector response functions. In the lower panels, the residuals of the fit are shown.

## 4.6 X-Ray Spectra of Member Galaxies

We extracted X-ray spectra for HCG 80a and b from circular regions with radii  $R_{\text{spec}} = 25''$  and  $1.5''$ , respectively (figure 4.4). Note that  $R_{\text{spec}}$  was so chosen that about 90% of the X-ray photons from each galaxy could be accumulated and that two galaxies might not overlap each other. We fitted the spectra with the power-law model and the MEKAL thin-thermal plasma model (Mewe et al. 1985, 1986; Kaastra 1992; Liedahl et al. 1995). The absorption column density was fixed at the Galactic value,  $N_{\text{H}} = 2.5 \times 10^{20} \text{ cm}^{-2}$  Dickey & Lockman 1990.

### HCG 80a

For HCG 80a, the power-law spectral model was rejected at the 99% confidence level. On the other hand, the MEKAL model provided a good fit to the data with a  $\chi^2$  value of 5.9 for 5 degrees of freedom. We obtained the temperature and the metallicity to be  $0.59_{-0.10}^{+0.12}$  keV and  $0.07_{-0.05}^{+0.18}$  solar, respectively. Though the AGN emission was estimated to be only  $\sim 20\%$  of the total emission from the image analysis, we checked whether the temperature determination of the intragroup gas was influenced by the AGN component in the following two ways: (1) excluded the central  $r < 5''$  circular region from the HCG 80a overall spectrum, and fit it with the MEKAL model, and (2) fit the overall spectrum with the two-component model, where the power-law index and the metallicity were, respectively, fixed at 2.0 and 0.1 solar. We found that both of the analyses yielded consistent temperatures ( $\sim 0.6$  keV) within the errors. We give the results for case (2) in table 4.4. We also confirmed that the ratio of the X-ray luminosities between the AGN and the diffuse components is consistent with the result of the image analysis

Table 4.4: Results of spectral fittings for HCG 80a and HCG 80b.

Galaxy	Model	Parameter	Value (90% error)	$\chi^2/\text{dof}$	
HCG 80a ( $R_{\text{spec}} = 25''$ )	MEKAL	$kT$ [keV]	$0.59^{+0.12}_{-0.10}$		
		$Z$ [solar]	$0.07^{+0.18}_{-0.05}$		
		$z$	0.02994 (F)		
		$k_M$ [*]	$9.9^{+8.3}_{-5.7} \times 10^{-5}$	5.9/5	
	PL +MEKAL	$\Gamma$	2.0 (F)		
		$k_P$ [†]	$< 5.2 \times 10^{-6}$		
		$kT$ [keV]	$0.56^{+0.12}_{-0.17}$		
		$Z$ [solar]	0.1 (F)		
		$z$	0.02994 (F)		
		$k_M$ [*]	$7.4^{+2.9}_{-1.9} \times 10^{-5}$	4.4/5	
		$f_{X,P}$ [erg s $^{-1}$ cm $^{-2}$ ][‡]	$< 2.1 \times 10^{-14}$		
		$L_{X,P}$ [erg s $^{-1}$ ][‡]	$< 4.6 \times 10^{40}$		
		$L_{\text{bol},P}$ [erg s $^{-1}$ ][**]	$< 6.1 \times 10^{40}$		
		$f_{X,M}$ [erg s $^{-1}$ cm $^{-2}$ ][§]	$(2.8 \pm 0.5) \times 10^{-14}$		
		$L_{X,M}$ [erg s $^{-1}$ ][§]	$6.5^{+0.8}_{-1.2} \times 10^{40}$		
		$L_{\text{bol},M}$ [erg s $^{-1}$ ][#]	$7.8^{+1.2}_{-1.6} \times 10^{40}$		
HCG 80b ( $R_{\text{spec}} = 1.5''$ )	PL	$\Gamma$	$1.94^{+0.19}_{-0.18}$		
		$k_P$ [†]	$2.5^{+0.3}_{-0.3} \times 10^{-5}$	10.7/11	
		$f_{X,P}$ [erg s $^{-1}$ cm $^{-2}$ ][‡]	$10.6^{+1.6}_{-1.8} \times 10^{-14}$		
		$L_{X,P}$ [erg s $^{-1}$ ][‡]	$(2.6 \pm 0.3) \times 10^{41}$		
		$L_{\text{bol},P}$ [erg s $^{-1}$ ][**]	$(3.5 \pm 0.4) \times 10^{41}$		
		MEKAL	$kT$ [keV]	$3.5^{+1.6}_{-1.0}$	
	$Z$ [solar]		$< 0.17$		
	$z$		0.03197 (F)		
	$k_M$ [*]		$1.07^{+0.16}_{-0.14} \times 10^{-4}$	12.7/10	

[\*] Normalization factor for the MEKAL model,  $k_M = \int n_e n_H dV / 4\pi (D_A (1+z))^2 [10^{-14} \text{ cm}^{-5}]$ , where  $D_A$  is the angular diameter distance to the source.

[†] Normalization factor for the power-law (PL) model,  $k_P$  [photons keV $^{-1}$ cm $^{-2}$ s $^{-1}$ ] at 1keV.

(F) Fixed parameters.

[‡] The 0.5–7 keV X-ray flux and the 0.5–7 keV luminosity for the PL model.

[§] The 0.5–7 keV X-ray flux and the 0.5–7 keV luminosity for the MEKAL model.

[\*\*] The bolometric X-ray luminosity for the PL model.

[#] The bolometric X-ray luminosity for the MEKAL model.

under Model 3 within 10%.

## HCG 80b

We found that the HCG 80b spectrum can be fitted either by the power-law model or the MEKAL model. Even though the MEKAL temperature of  $kT \sim 3.5$  keV may be consistent with a collection of Low Mass X-ray Binaries, the observed luminosity of  $2.6 \times 10^{41}$  erg s<sup>-1</sup> is by more than 3 orders higher than the values for normal spiral galaxies. On the other hand, the power-law index of  $\Gamma = 1.94^{+0.19}_{-0.18}$ , deduced from the X-ray spectral fitting is consistent with the values of known AGNs. We also estimated the  $\alpha_{\text{OX}}$  index, which is the slope of a hypothetical power law connecting the B band and 2 keV, to be 1.9. The value is larger compared with the result of the ROSAT large quasar survey, but within the scatter of the quasars (figure 2 of Green et al. 1995). Thus, the emission from the central  $r < 1.5''$  region is most likely to originate from the AGN in the galaxy.

## 4.7 Constraints on the Hot Diffuse Emission

In order to constrain the X-ray emission from the hot intragroup medium, we defined the group region with a  $r = 84'' = 50.5$  kpc circle, whose center is the same as that of HCG 80, 15h59m12.4s, +65° 13'33.3" (Hickson et al. 1989), which encompasses the optical disks of the four member galaxies (figure 4.1b). We subtracted the background and the galaxy contributions from the total photon counts in the group region and derived the intensity of the intragroup emission. Note that we used the background intensity estimated from the outer-ring region. The source counts within  $31''$  from the brightest member, HCG 80a, were estimated based on the results of the image analysis presented in subsection 4.4.1, while for HCG 80b–d, the observed source counts within circles of radii  $R_{\text{max}} = 10'', 9.8''$  and  $13.6''$ , approximately equal to the sizes of the optical disks, were used.

Subtracting the galaxy contributions,  $130 \pm 12$ ,  $223 \pm 15$ ,  $11 \pm 3$ ,  $3 (< 5)$  counts for HCG 80a–d and the background,  $213 \pm 9$  counts from the total photon counts of  $576 \pm 24$  in the group region, we found that there is no significant emission from the hot IGM, and that the  $3\sigma$  upper limit is obtained to be 92 photons in the 0.5–2 keV band. We also confirmed that the present estimation of the IGM emission is not affected by the choice of the extraction radii,  $R_{\text{max}}$  for the galaxies b–d; if we change  $R_{\text{max}}$  by a factor of 0.5–1.5, the result changes by only  $\lesssim 10\%$ . If we further assume the temperature and the metallicity of the gas to be comparable to those derived for HCG 16,  $kT \sim 0.5$  keV and  $Z \sim 0.1$  solar (Belsole et al. 2003), the bolometric luminosity is constrained as  $L_X < 6.3 \times 10^{40}$  erg s<sup>-1</sup> ( $3\sigma$ ). We show the location of HCG 80 on the  $L_X - f_{\text{spiral}}$  plane in figure 4.5.

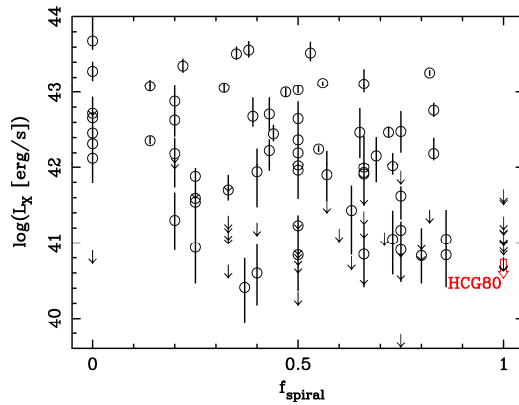


Fig. 4.5:  $L_X - f_{\text{spiral}}$  relation. The groups with constrained/unconstrained bolometric luminosity from the ROSAT PSPC survey Mulchaey et al. 2003 are plotted with open circle/arrow, as a function of the spiral fraction. The upper limit on the bolometric luminosity for the hot diffuse gas in HCG 80, obtained from the present Chandra analysis, is indicated by the red arrow.

## 4.8 Nucluous/Starburst Activities of Member Galaxies

### 4.8.1 $L_X - L_B$ relations

From a high-resolution Chandra observation of the spiral-only group HCG 80, we detected significant X-ray emission from three of the four member galaxies (HCG 80a, b, and c), and investigated the spatial distribution and the spectral features for HCG 80a and b in detail. In particular, we discovered halo emission from HCG 80a, which extends to  $\sim 30$  kpc perpendicular to the galactic disk.

We show the relation between the bolometric X-ray luminosity,  $L_X$ , and the  $B$  band luminosity,  $L_B$ , for the HCG 80 members in figure 4.6. In addition to the overall luminosities of the galaxies, the luminosities of the nucleus, disk, and halo regions are separately plotted for HCG 80a and b. The X-ray luminosities were estimated from the spectral analyses for HCG 80a and the HCG 80b nucleus. However, because the spectra for the HCG 80b disk, HCG 80c and d were not constrained, we assume the thermal emission with  $kT = 0.5$  keV and  $Z = 0.1$  solar to convert the photon counting rates in the soft band (table 4.2) to  $L_X$ . This assumption may be valid because the hardness ratios listed in table 4.2 are in agreement with the values for soft thermal emission.

Comparing with the best-fit  $L_X - L_B$  relation for the spiral galaxies in the Helsdon et al. 2001 sample, we found that the disk component of HCG 80b and the overall luminosities of HCG 80c and d are consistent with their relation if we take into account the measurement errors and the large data scatter among the other spiral galaxies. On the other hand, HCG 80a and b clearly show a higher  $L_X$  value than expected from the  $L_X - L_B$  relation from Helsdon et al. 2001. They noted that the galaxies associated with the AGN and/or the starburst activities tend to

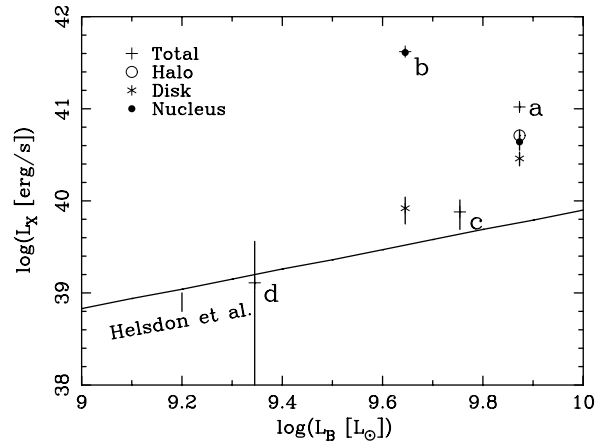


Fig. 4.6:  $L_X - L_B$  relation. The bolometric luminosity of the overall galaxy region is plotted against the B luminosity [ $L_\odot$ ] for each galaxy (cross). For HCG 80a, the nucleus, disk and halo components are also separately indicated by the solid circle, asterisk, and open circle, respectively. For HCG 80b, the nucleus and the disk components are indicated by the solid circle and asterisk, respectively. The error bars are the  $1\sigma$ . The solid line represents the best-fit  $L_X - L_B$  relation for the spiral group galaxies Helsdon et al. 2001.

lie above the best-fitting line, namely they have enhanced X-ray emission relative to the optical band. Thus considering from the thermal nature of the extended emission of HCG 80a and the hard spectrum of the point-like emission from HCG 80b found in the previous section, the higher  $L_X$  values agree with their indication.

Furthermore, starburst galaxies are often identified based on their high IR luminosity and warm FIR colors,  $f_{60}/f_{100} > 0.4$ . The FIR fluxes are available only for HCG 80a. From the IRAS 12-, 25-, 60-, and 100- $\mu\text{m}$  fluxes,  $(f_{12}, f_{25}, f_{60}, f_{100}) = (0.10, 0.16, 2.31, 5.16)$  Jy, the IR luminosity is  $L_{IR} = 12.3 \times 10^{10} L_\odot$  utilizing  $L_{IR} = 5.67 \times 10^5 D_{\text{Mpc}}^2 (13.48f_{12} + 5.16f_{25} + 2.58f_{60} + f_{100}) L_\odot$  Sanders & Mirabel 1996. This is consistent with the  $L_X - L_{IR}$  correlation for starburst galaxies (Strickland et al. 2004b; Helsdon et al. 2001).  $f_{60}/f_{100} = 0.45$ ; hence HCG 80a is ‘‘FIR warm’’. Thus, the above facts strongly support that the X-ray emission from HCG 80a is produced by starburst activity. In the next subsection, we derive some physical parameters to characterize a starburst, and compare them to the previous measurements on other starburst galaxies, in light of energy feedback from massive stars.

#### 4.8.2 Starburst Activity in HCG 80a

The huge extraplanar emission discovered in HCG 80a reminds us of the bipolar outflow in a bright starburst galaxy, such as M 82 (e.g., Lehnert et al. 1999). The X-ray luminosity from the HCG 80a halo is determined to be  $\sim 4 \times 10^{40} \text{ erg s}^{-1}$  (table 4.5), which is even larger than that reported for bright starburst galaxies. We show a detailed comparison of the luminosities derived

Table 4.5: Halo, disk, nuclear, and total luminosities.

Galaxy	$\langle kT \rangle$ [*]	Band[†]	$L_{X,H}$ [‡]	$L_{X,D}$ [§]	$L_{X,N}$ [  ]	$L_{X,tot}$ [#]	$L_B$ [**]	$L_{IR}$ [**]	$SFR_{IR}$ [††]
HCG 80a	$0.56^{+0.12}_{-0.17}$	0.5–2	$3.5 \pm 0.5$	$2.0 \pm 0.4$	$1.6 \pm 0.3$	$7.1 \pm 0.7$	0.75	12.3	21.1
HCG 80a	$0.56^{+0.12}_{-0.17}$	0.3–2	$4.5 \pm 0.7$	$2.6 \pm 0.4$	$2.1 \pm 0.4$	$9.2 \pm 0.9$	0.75	12.3	21.1
M 82[‡‡]	0.37	0.3–2	0.41	1.6	2.3	4.3	0.33	5.36	9.2
NGC 253[‡‡]	0.25	0.3–2	0.12	0.33	0.094	0.55	0.58	2.10	3.6

[\*] Emission-weighted X-ray temperature of the diffuse emission in keV.

[†] Energy band in keV used to calculate the X-ray luminosities.

[‡, §, ||] X-ray luminosities for the halo (H), the disk (D), and the nucleus (N) regions in  $10^{40} \text{erg s}^{-1}$ .

[#] Total X-ray luminosity for the H + D + N regions in  $10^{40} \text{erg s}^{-1}$ . The errors of the luminosity measurements for HCG 80a are the  $1\sigma$ .

[\*\*]  $B$  and IR luminosities in  $10^{10} L_{\odot}$ .

[††] Star-formation rate from the IR luminosity,  $SFR_{IR} = 4.5 \times 10^{-44} L_{IR} [\text{erg s}^{-1}]$  Kennicutt 1998.

[‡‡] The values were taken from Strickland et al. 2004a.

in subsection 4.4.1 and the emission-weighted X-ray temperature to the values reported for M 82 and NGC 253 Strickland et al. 2004a. We also show the star-formation rate estimated from the IR luminosity,  $SFR_{IR} = 21.1 M_{\odot} \text{yr}^{-1}$ , where  $SFR_{IR} = 4.5 \times 10^{-44} L_{IR} [\text{erg s}^{-1}]$  Kennicutt 1998.

In order to investigate the physical properties of the X-ray emitting thermal plasma in the halo, we treated the emission region as a cylinder of diameter 4 kpc and height 30 kpc, and estimated the electron density and the gas mass. Thus, the following values are meaningful only as order-of-magnitude estimates. The volume of the cylinder is  $V = 1.1 \times 10^{67} \text{cm}^3$  and the emission integral of the corresponding region is  $EI = n_e n_H V = 1.44 \times 10^{64} \text{cm}^{-3}$  based on the result of the spectral fitting. These yielded the electron density, the thermal pressure, the thermal energy, and the gas mass for an average temperature of  $T = 6.5 \times 10^6 \text{K}$ , as follows:

$$n_e = 4.0 \times 10^{-2} \text{cm}^{-3}, \quad (4.4)$$

$$P_{\text{th}}/k = n_e T = 2.6 \times 10^5 \text{K cm}^{-3}, \quad (4.5)$$

$$M_{\text{gas}} = \mu_e m_p n_e V = 4.3 \times 10^8 M_{\odot}, \quad (4.6)$$

$$E_{\text{th}} = \frac{3}{2} (n_e + n_H) k T V = 1.1 \times 10^{57} \text{erg}, \quad (4.7)$$

where we adopt  $n_H = (\mu_e/\mu_H)n_e$ ,  $\mu_e = 1.167$ , and  $\mu_H = 1.40$ . The above values are higher by about a factor of  $\gtrsim 5$  than those obtained for NGC 253 Strickland et al. 2002 if we neglect any systematic error.

The radiative cooling timescale of the gas and the mass-cooling rate are estimated to be  $t_{\text{cool}} \sim E_{\text{th}}/L_{\text{bol}} = 390 \text{Myr}$  and  $\dot{M}_{\text{gas}} \sim 1.1 M_{\odot} \text{yr}^{-1}$ . Then, supposing that the flow velocity may be approximated by the sound speed of the gas,  $v_{\text{flow}} \sim v_s = 292 \text{km s}^{-1}$ , the time necessary to travel the distance of 15 kpc (a half of the height of the cylinder) is  $t_{\text{flow}} \sim 50 \text{Myr}$ . Since  $t_{\text{cool}} \gg t_{\text{flow}}$ , the condition for maintaining halo emission seems to be satisfied.

The above calculations and the high SF rate inferred from the IR luminosity indicate that an

enormous thermal energy of  $\sim 10^{57}$  erg would be supplied through successive SN explosions and the formation of superbubbles. We will estimate the SN rate and also compare the estimated quantities with the “disk blowout” condition to test the plausibility of the present interpretation.

Assuming a Type II supernova energy input of  $10^{51}$  erg and a canonical value for the thermalization efficiency of 10%, the thermal energy contained in the hot gas requires  $\sim 10^7$  SNe. Thus, the SN rate is expected to be  $\sim 10^7/t_{\text{flow}} = 0.2 \text{ yr}^{-1}$  to keep the  $\sim 10^7$  ejecta in the halo region. Alternatively, with the IR luminosity and the relation from Heckman et al. 1990, the SN rate is  $R_{\text{SN}} = 0.2L_{\text{IR}}/10^{11}L_{\odot} \sim 0.25 \text{ yr}^{-1}$ . Then, if the successive star formation had lasted in the past for  $t_{\text{SF}} = 40 \text{ Myr}$ , and one supernova may supply thermal energy of  $10^{50} \text{ erg s}^{-1}$ , the SN rate of  $0.25 \text{ yr}^{-1}$  can account for the thermal energy in the halo of  $E_{\text{th}} \sim 10^{57}$  ergs [equation (4.7)]. The duration of  $t_{\text{SF}} = 40 \text{ Myr}$  is comparable to the timescale of the outflow,  $t_{\text{flow}}$ , and seems also to be reasonable from the point of view of the typical lifetime of massive stars,  $\sim 10 \text{ Myr}$ .

We next consider whether the gas can really escape from the galaxy potential well against the gravitational force. The escape velocity was estimated to be  $v_{\text{esc}} \sim 120 \text{ km s}^{-1}$  (or equivalently  $kT \sim 0.14 \text{ keV}$ ) utilizing a mass-to-light ratio of  $M/L_B \simeq 60h(R/0.1\text{Mpc})M_{\odot}/L_{\odot}$  for spiral galaxies Bahcall et al. 1995. Here, we assumed that the galaxy mass within  $R$  is given by  $M \sim Rv_{\text{esc}}^2/G$ , and adopted  $R = 15 \text{ kpc}$ , which corresponds to the isophotal radius,  $R_{25}$  Hickson 1993. Note that the rotation curve was measured within the central  $r \lesssim 4 \text{ kpc}$  by Nishiura et al. 2000. Though it is difficult to infer  $v_{\text{esc}}$  from their result, due to the existence of asymmetry between the approaching and receding sides of the galaxy, the average rotation velocity is roughly  $\sim 130 \text{ km s}^{-1}$ , and thus comparable to the value estimated above. Therefore, the observed temperature of  $0.6 \text{ keV}$  is sufficiently high for the gas to escape into intergalactic space.

The critical mechanical luminosity for the disk blowout [see Strickland et al. 2004b and references therein] is calculated as  $L_{\text{crit}} = 4.2 \times 10^{40} \text{ erg s}^{-1}$ . The mechanical energy injection of the halo may be given by  $L_{\text{W}} \sim L_{\text{X,H}} = 3.5 \times 10^{40} \text{ erg s}^{-1}$ . Therefore,  $L_{\text{W}} \sim L_{\text{crit}}$ . Furthermore, we compare the density of the halo region derived in equation (4.4) to a model calculation of a disk-halo interaction by Norman & Ikeuchi 1989 to find that it is within the chimney/starburst phase where the blow-out occurs.

The mass-flow rate is estimated to be  $\dot{M}_{\text{flow}} \sim M_{\text{gas}}v_{\text{flow}}/y \sim 8.5 M_{\odot}\text{yr}^{-1}$ , where  $v_{\text{flow}} = v_s$  and  $y = 15 \text{ kpc}$  are assumed. For well-known bright starburst galaxies, NGC 253 and M 82, the rates are  $\dot{M}_{\text{flow}} = 5.8(v_{\text{flow}}/1000 \text{ km s}^{-1})(y/6.35 \text{ kpc})^{-1} M_{\odot}\text{yr}^{-1}$  Strickland et al. 2002 and  $12.9(v_{\text{flow}}/600 \text{ km s}^{-1})(y/6 \text{ kpc}) M_{\odot}\text{yr}^{-1}$  Strickland et al. 1997, assuming the volume filling factor of the hot plasma to be 1 and a metal abundance of  $Z=0.05$  solar. Thus, the mass-flow rate for HCG 80a is likely to be one of the largest among known starburst galaxies. Furthermore, like the cylindrical structure of the CO molecular gas observed in M 82 Nakai et al. 1987, the outflow of cold matter undetectable in X-rays may raise the  $\dot{M}_{\text{flow}}$  value significantly if it exists. For example, if the total mass flow is ten-times larger than that estimated from the X-ray observation only,  $t_{\text{SF}} = 40 \text{ Myr}$  would result in a total mass loss of  $\sim 4 \times 10^9 M_{\odot}$ . This corresponds to about 10% of the total galaxy mass inferred from the  $M/L_B$  ratio,  $M \sim 4.7 \times 10^{10} M_{\odot}$ .

In conclusion it is highly plausible that HCG 80a is a starburst galaxy that exhibits one of the most energetic outflows powered by starburst activity known in the universe.

## 4.9 Diffuse Hot Gas in HCG 80

We obtained a severe constraint on the intensity of the diffuse emission from the HCG 80 group region,  $L_X < 6.3 \times 10^{40} \text{ erg s}^{-1}$ , which is one of the lowest among the ROSAT groups of galaxies (figure 4.5). The flux sensitivity of the present *Chandra* observation is higher by a factor of about 25 than that of the previous ROSAT/PSPC observation Ponman et al. 1996. Thus, it is clear that the current upper limit is lower by more than one order of magnitude than that expected from the  $\sigma - L_X$  relation. Compared with the X-ray luminosity of HCG 16 measured with XMM-Newton,  $L_X = 5.0 \times 10^{40} h_{70}^{-2} \text{ erg s}^{-1}$  Belsole et al. 2003, our upper limit is comparable to their result. If we further assume that the intragroup gas in HCG 80 is a 0.5 keV thermal plasma, distributed within a sphere of radius 50 kpc, the upper limits on the electron density and the total gas mass are estimated to be  $n_e < 8.4 \times 10^{-4} \text{ cm}^{-3}$  and  $M_{\text{IGM}} < 1.3 \times 10^{10} M_{\odot}$ .

If we suppose that the HCG 80 group is a virialized system, and that the velocity dispersion properly measures the potential well, the total mass is  $M_{\text{tot}} = 3\sigma_v^2 R/G \sim 3.4 \times 10^{12} M_{\odot}$ , yielding a gas mass to the total mass ratio of  $< 0.004$ . This unusually small value may be a consequence of the following possibilities: 1) HCG 80 is a chance alignment and not a real, physical system; 2) HCG 80 is a virializing, young system and the gas is yet to be heated to emit appreciable X-rays; or 3) the diffuse gas is expelled from HCG 80 by, for instance, violent activity of member galaxies.

Regarding the first possibility, the differences in the line-of-sight velocity relative to HCG 80a are  $\Delta cz = +621, +587, +145 \text{ km s}^{-1}$  for HCG 80b, c, d, respectively Arp 1997. They satisfy the criterion  $\Delta cz < 1000 \text{ km s}^{-1}$  for the accordant system applied in Arp 1997. It is admittedly difficult to judge from the  $\Delta cz$  values alone whether galaxies are indeed concentrated compared to the field sample, since the velocity dispersion of the member galaxies,  $309 \text{ km s}^{-1}$ , corresponds to a comoving separation of 4.3 Mpc. The four members of HCG 80, however, are clustered within a circle of  $r = 50.5 \text{ kpc}$  on the sky, yielding a cylindrical volume containing four galaxies of  $0.07 \text{ Mpc}^3$ . This is only 1/15 of the mean occupied volume,  $\sim 1 \text{ Mpc}^3$ , of field galaxies brighter than HCG 80d ( $B = 17$ ), based on the luminosity function in the SDSS  $b_j$  band Blanton et al. 2001. This is supportive of a significant galaxy concentration in the HCG 80 group.

We further note that an exceptionally strong activity inferred in HCG 80a may be a result of galaxy interaction in the high-density environment. Coziol et al. 2004 quantified the level of activity (star formation or AGN) using a sample of 91 galaxies in the compact groups, and suggested an evolutionary sequence that groups at their early stage of evolution tend to be rich in spiral members with high activity levels, and show a smaller velocity dispersion. Since our results show that HCG 80 contains at least two active galaxies, and that the velocity dispersion

of  $\sigma_v = 309 \text{ km s}^{-1}$  is relatively small among their sample, HCG 80 is likely to be close to their configuration “type A”, corresponding to a lower level of evolution. In addition, Verdes-Montenegro et al. 2001 showed that the groups richer in early type galaxies or more compact with larger velocity dispersion have a weak tendency to be more deficient in HI gas than expected from the optical luminosities, and proposed a scenario that the amount of HI gas would decrease further with evolution by tidal stripping and/or heating. Therefore, no significant HI deficiency in HCG 80 may also imply the lower level of evolution. In order to further confirm the reality of the system and to constrain the physical properties, it is necessary to identify the distances of the HCG 80 galaxies, and also to search for evidence of interactions.

As pointed out by Mulchaey et al. (2000) Mulchaey 2000, the hypothesis that the all spiral-only group is a mere chance alignment is unlikely given the existence of the our own spiral-only Local Group. We thus compare our result with the Local Group. Wang & McCray (1993) Wang & McCray 1993 found the soft X-ray component with temperature 0.2 keV in the soft X-ray background, which could be due to a warm intragroup medium in the Local Group. Rasmussen et al. 2003 measured the absorption-line features towards three AGNs using the XMM-Newton/RGS deep spectroscopic data, whose redshift appear to be  $z \sim 0$ , and placed limits on the electron density,  $n_e < 2 \times 10^{-4} \text{ cm}^{-3}$ , the scale length of the absorber,  $L > 140 \text{ kpc}$ , and its mass,  $M_{\text{IGM}} < 5 \times 10^{10} M_{\odot}$ , in a collisional equilibrium approximation. Thus, the upper limit on the hot IGM in the HCG 80 group from the Chandra observation is similar to that of the Local Group, suggesting that the spiral-only groups may contain very tenuous IGM.

Another interpretation may be possible within the context of the preheating models for groups (e.g., Ponman et al. (1999) Ponman et al. 1999). The model predicts that the energy input through galactic winds or outflows, powered by supernovae, should cause a more extended gas distribution, resulting in the gas density being too low to be detected in X-rays. Thus, the large halo emission discovered in HCG 80a and the low density of the intergalactic medium suggested from the analysis are not in conflict with the view of the preheating model. However, it is inconclusive because the non-detection of diffuse intragroup gas does not allow us to put any quantitative constraint on a connection between the outflowing gas and the intragroup gas. Additional follow-up observations will be meaningful to further clarify the role of spiral galaxies in the evolution of the IGM, probably at its early stage.



# Chapter 5

## HCG 62

In this section, I study the results from Chandra and XMM-Newton observations of HCG 62. This is organized as follows: In §5.1 and 5.2 we describe the Chandra and XMM-Newton observations and the data reduction. In §5.3 we give the image of HCG 62 of both Chandra and XMM-Newton, in §5.4 we describe the X-ray cavity structure using Chandra image. In §5.5 we present our results on the temperature profiles and the abundances profiles of Fe and  $\alpha$ -elements (Si, Mg, and O). From §5.6 to §5.8 we give a discussion of the obtained results.

### 5.1 Chandra and XMM-Newton Observations of HCG62

HCG 62 was observed on 25 January 2000 with the ACIS I2, I3, S2, S3, and S4 chips operated at the CCD temperature of  $-110^{\circ}\text{C}$  with a frame readout time of 3.24 s. We used the data of only the ACIS-S3 chip ( $8.4' \times 8.4'$ ) covering the central part of HCG 62 in this paper. The pointing coordinates were (12:59:05.70,  $-09^{\circ}12'20.00''$ ) (J2000) and the total exposure was 49.15 ks.

The XMM-Newton observation of HCG 62 was carried out on 15 January 2003, assigned for 12.6 ks. The EPIC cameras were operated in full-frame mode for MOS, and in extended-full-frame mode for pn. The medium filters were used for both cameras.

### 5.2 Data Reduction

#### 5.2.1 Chandra

According to the “Chandra Aspect” web page, <http://cxc.harvard.edu/cal/ASPECT/>, the astrometry offset of  $\text{RA} = -0.03''$ ,  $\text{Dec} = 0.22''$  has been corrected for in the data, providing a radius of 0.6 arcsec as the absolute position accuracy in 90% confidence. The CCD temperature of ACIS was reduced to  $-120^{\circ}\text{C}$  soon after the observation of HCG 62 in January 2000 due to the increase of charge transfer inefficiency (CTI) caused by the radiation damage in orbit (Grant et al. 2005). The data were telemetered in the Faint mode, and events with the ASCA grades of 0, 2, 3, 4, and 6 were used. Bad pixels, bad columns, and the columns next to bad columns and

to the chip node boundaries are excluded. In order to remove periods of anomalous background levels, we further filtered the events using the 0.3–10 keV band light curve of the whole ACIS-S3 chip in 200 s bin, and discarded periods which exceeded by  $3\sigma$  above the mean quiescent rate of 4.5 c/s/chip. The net exposure time after the screening was 48,013 s. The data reduction was performed using CIAO version 3.1 with CALDB version 2.29, and the spectral fitting was done by XSPEC version 11.3.0t.

All of the X-ray spectra were extracted using the pulse-height invariant (PI) values, which were recomputed using the latest gain file `acisD1999-09-16gainN0005.fits`, appropriate for the CCD temperature of  $-110^\circ\text{C}$ . In the spectral fitting, we initially generated the response matrix file (RMF) of the ACIS-S3 using the CIAO “mkrmf” task with the input FEF (FITS Embedded Function) file of `acisD1999-09-16fef_phaN0002.fits`, which was chosen by default. However, we found that the Si line of the IGM emission was significantly broader than the response ( $\sigma = 42^{+9}_{-8}$  eV), which caused the fit statistics not acceptable. In order to examine whether this broad Si line is a target specific issue or a common calibration problem, we further checked the neutral Si line,  $K_{\alpha 1} = 1739.98$  eV and  $K_{\alpha 2} = 1739.38$  eV, which is originated in the instrumental background of the CCD, using the blank-sky data obtained at  $-110^\circ\text{C}$  (figure 5.1 (a)). The fit result gave the Gaussian  $\sigma = 29 \pm 4$  eV (FWHM =  $68 \pm 9$  eV) and the line center energy of  $1753 \pm 3$  eV, which is significantly broad, too. We splitted the blank-sky spectrum into two, dividing the integration region into half, i.e. upper rows and lower rows of the CCD, although the results were similar. This result indicates that the charge transfer inefficiency (CTI) correction is working well.

We therefore concluded that the broad Si line was resulted because the generated RMF had too sharp Gaussian core. In fact, the derived Si line width for the blank-sky is consistent with a calibration document, ACIS Memo #182 by LaMarr (2000) LaMarr 2003. The FWHM of the Gaussian core for the RMF denoted in the FEF file is  $G1\_FWHM = 73$  eV for ACIS-S3 (CCD\_ID=7) at the energy of 1.8 keV, while it should be around 125 eV according to the memo. Our blank-sky data indicated  $\sqrt{73^2 + 68^2} = 100$  eV, which is slightly better than the value in the LaMarr’s memo, possibly due to the updated gain file. We therefore created a new FEF file to adopt broader Gaussian core over the whole energy range, modifying the `G1_FWHM` column into  $(16 \times \text{ENERGY} + G1\_FWHM)$ . Using the new FEF file, we generated the RMF files with the “mkrmf” task for the following analysis.

Regarding the “blank-sky” background, we adopted a series of observations compiled by Markevitch 2004 (<http://cxc.harvard.edu/contrib/maxim/acisbg/>), when the CCD temperature was  $-110^\circ\text{C}$ . The “blank-sky” background events were also screened to remove background flares in the same way as described above. The additional component due to the Galactic soft background are considered in § 5.2.3.

### 5.2.2 XMM-Newton

XMM-Newton covers the wider field of view of  $r \lesssim 15'$  than Chandra, while the angular resolution of  $15''$  half-power diameter is broader. Data reduction was performed using SAS version 6.0, and the spectral fitting was done by XSPEC version 11.3.0t. We selected events with pattern 0–12 for MOS and 0–4 for pn, and flag = 0 for both. Bad pixels and bad columns were excluded. We calculated the count rate distribution with 100 s intervals over the 0.3–10 keV range using the whole chip of each sensor, and rejected periods by requiring all the count rates to be within  $\pm 2\sigma$  around the mean. We iterated the process until the number of rejected data in a step reached less than 5% of the  $2\sigma$  compared with the previous value. Because we did not find large time variation nor flares, the net exposure time after the screening was 12.6, 12.5, and 9.2 ks for MOS1, MOS2, and pn, respectively.

To correct for the vignetting effect, the SAS “evigweight” task was applied for each event file. All the X-ray spectra were extracted using the vignetting-weighted events. The response files for spectral fittings were generated in the standard way with the SAS “rmfgen” and “arfgen” tasks at on-axes of the X-ray mirrors. The MOS1 and MOS2 spectra are summed up, and the energy range of 1.4367–1.5367 keV, where the background Al-K $_{\alpha}$  (1.4867 keV) is strong as seen in figure 5.1 (b) and (c), is ignored in the spectral fitting for both MOS and pn.

The background event dataset created by Read et al. (2003) Read & Ponman 2003 was adopted as the “blank-sky” background for the XMM-Newton observation. We applied the same selection criteria as the source events to the “blank-sky” background. The “blank-sky” background was scaled to 0.94 for MOS1, 1.00 for MOS2, and 0.84 for pn, respectively. These factors were determined by the count rate ratio within  $r < 14'$  from the central galaxy HCG 62a in 10–12 keV (MOS) or 12–14 keV (pn) band, where the instrumental background is dominant for each sensor. Katayama et al. (2004) Katayama et al. 2004 and Nevalainen et al. (2005) Nevalainen et al. 2005 have studied the background data of XMM-Newton in detail, and it is reported that the the 90% confidence background uncertainty is  $\pm 5\%$  in 4–7 keV and  $\pm 20\%$  in 0.8–1 keV. It is confirmed that our results does not change significantly within errors when this level of uncertainty is considered.

### 5.2.3 Background estimation

HCG 62 is located near the edge of the North Polar Spur (NPS), which is a large soft X-ray Galactic structure. The ROSAT All-Sky Survey (RASS) image at 3/4 keV band in this region indicates a soft X-ray excess around the position of HCG 62, although significant fraction of the excess is probably caused by HCG 62 itself. This emission looks more extended than the Chandra and XMM-Newton fields of view in the previous observations with ROSAT and ASCA. Therefore, we cannot use the events in outer region as the background, and we need to estimate the influence of the soft X-ray background to our HCG 62 data using the “blank-sky” background.

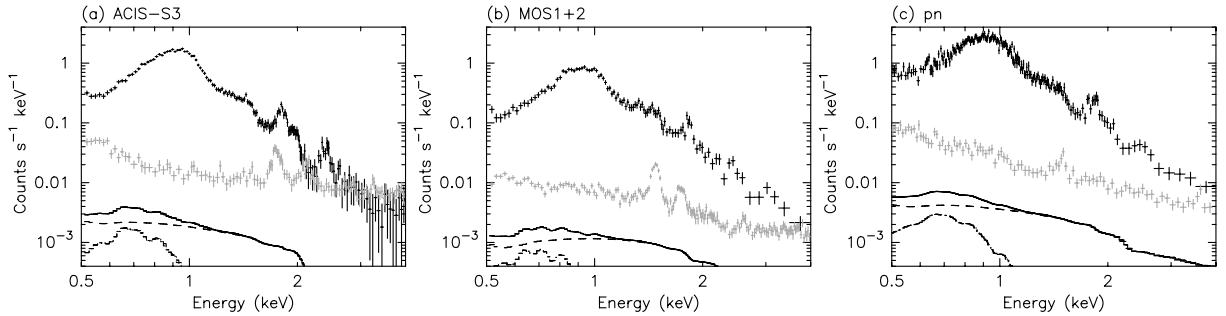


Fig. 5.1: X-ray spectra of (a) Chandra ACIS-S3, (b) XMM-Newton MOS1+2, and (c) pn, in 0.5–4 keV within  $r < 2'$  from the central galaxy HCG 62a, subtracted by the “blank-sky” background. The “blank-sky” spectra are indicated by gray lines. The additional background components of the 0.3 keV Mekal and the  $\Gamma = 1.5$  power-law models are shown by dashed black lines, and their sum is indicated by solid black lines.

There are four fields near HCG 62 already observed with Chandra, Q1246–0542, NGC 4697, NGC 4594, and NGC 4782. We found that the intensities below 2 keV in source-free regions in these fields are higher than the level of the “blank-sky” background, while the hard band intensities show no excess. By fitting the energy spectra of the soft excess component with the XSPEC Mekal model, we obtained the temperature to be  $\sim 0.3$  keV, consistent with the previous result for the Galactic soft emission from NPS Inoue et al. 1980. The surface brightness in the four nearby fields differ significantly, ranging in  $(5\text{--}10) \times 10^{-10}$  photons  $\text{cm}^{-2} \text{s}^{-1} \text{arcsec}^{-2}$  in 0.5–1 keV band, and we need to estimate the soft X-ray background component based on the data of the HCG 62 field.

We examined the radial profile at  $r < 15'$  of the XMM-Newton data in 0.5–1 keV band by fitting with a sum of a double  $\beta$  model and a constant intensity representing the soft X-ray background. In fitting the profile, parameters for the double  $\beta$  component were fixed at the ROSAT values Zabludoff & Mulchaey 2000, and only the level of the constant component was varied as a free parameter. The resultant surface brightness is  $2 \times 10^{-11}$  photons  $\text{cm}^{-2} \text{s}^{-1} \text{arcsec}^{-2}$  in 0.5–1 keV band. In the following analysis, the excess soft component is assumed to be a thermal emission with the temperature of 0.3 keV and abundance of 1 solar, with the normalization fixed at the level of the radial profile fit above. We do not apply interstellar absorption for this component, since its origin is supposed to be a nearby region in our galaxy. When the normalization of the 0.3 keV component is varied in the spectral fit, it agrees with the level derived from the radial profile, within the 90% confidence limit for both Chandra and XMM-Newton. In fact, the estimated additional soft component is much fainter than those in the four nearby fields, even less than the “blank-sky” background component. The “blank-sky” background also contains a certain fraction of the Galactic soft emission, and the HCG 62 field appears to require only the same level of soft X-ray background. We have also confirmed that our result did not

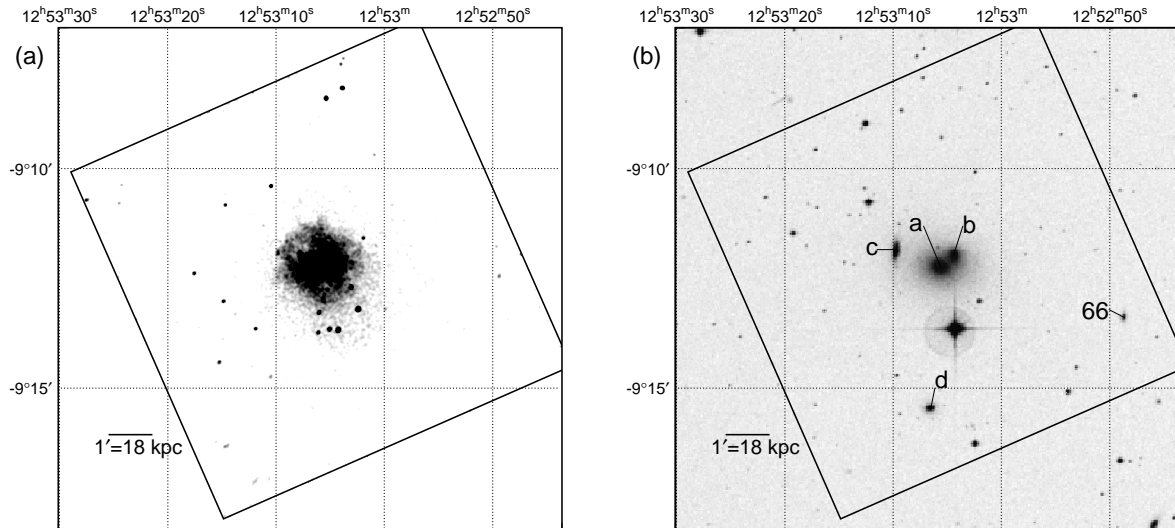


Fig. 5.2: (a) Gaussian smoothed Chandra ACIS-S3 X-ray image in the 0.5–4 keV band. The smoothing scale is  $\sigma = 1.5''$  and the image is corrected for exposure and background. (b) STScI Digitized Sky Survey (DSS) image of HCG 62. The ACIS-S3 field is indicated by a square, and the member galaxies are denoted by a, b, c, d, and 66. Coordinates of images are J2000.

change significantly within errors even doubling the intensity of the estimated soft background component.

As for the additional hard X-ray background component, we take into account the excess emission detected with ASCA Fukazawa et al. 2001. In the 2–10 keV range, the observed flux of the  $\Gamma = 1.5$  power-law component with ASCA is  $1.0 \times 10^{-12}$  ergs  $\text{cm}^{-2}$   $\text{s}^{-1}$  at the ring-like area with inner and outer radii to be  $5'$  and  $15'$ . We assumed the same power-law spectrum in our analysis, with the spatial distribution uniform over the whole HCG 62 field for both Chandra and XMM-Newton.

In the following analysis, the soft and the hard components were added as additional spectral models with fixed parameters. We however confirmed that the results did not vary significantly at the 90% confidence level, even if we did not apply these backgrounds. In figure 5.1, the soft and the hard X-ray background components as well as the “blank sky” background are compared with the IGM spectrum for each instrument.

## 5.3 X-ray Image

### 5.3.1 Chandra image

The Chandra image of HCG 62 taken with ACIS-S3 in the 0.5–4 keV energy band is shown in figure 5.2 (a). We corrected for background and exposure, and applied Gaussian smoothing. The positional dependence of the telescope and the detector responses were corrected with an

Table 5.1: Optical properties of HCG 62 and member galaxies.

Object	Optical coords. (J2000) *		$z$ *	Diameter † (arcsec)	$B$ † (mag)	Type ‡
	R.A.	Dec.				
HCG 62 .....	12 <sup>h</sup> 53 <sup>m</sup> 06 <sup>s</sup> .1	−09°12′16″.3	0.0145	—	—	Group
HCG 62a .....	12 <sup>h</sup> 53 <sup>m</sup> 05 <sup>s</sup> .6	−09°12′13″	0.0143	59.9	13.79	E3 / S0
HCG 62b .....	12 <sup>h</sup> 53 <sup>m</sup> 04 <sup>s</sup> .4	−09°11′59″	0.0119	42.9	14.21	S0 / S0
HCG 62c .....	12 <sup>h</sup> 53 <sup>m</sup> 09 <sup>s</sup> .7	−09°11′51″	0.0148	40.2	15.00	S0 / E
HCG 62d .....	12 <sup>h</sup> 53 <sup>m</sup> 06 <sup>s</sup> .6	−09°15′26″	0.0136	19.7	16.30	E2 / —
HCG 62-66 § .....	12 <sup>h</sup> 52 <sup>m</sup> 48 <sup>s</sup> .7	−09°13′22″	0.0161	—	—	— / —

\* Optical coordinates and redshift  $z$  by Mulchaey et al. (2003) for HCG 62 and by Zabludoff & Mulchaey (2000) for member galaxies.

†  $B$  band effective diameter,  $D_B = \sqrt{A_B/\pi}$ , and magnitude within  $\mu_B = 24.5$  mag arcsec<sup>−2</sup> isophote by Hickson et al. (1989).

‡ Hubble morphological type classification by Hickson et al. (1989) or Shimada et al. (2000b).

§ Because HCG 62-66 is not catalogued by Hickson et al. (1989), Diameter,  $B$ , and Type are left blank.

Table 5.2: X-ray properties of detected galaxies by Chandra ACIS-S3.

Object	X-ray position (J2000) *		Pos. diff. † (arcsec)	Obs. count ‡ (cts)	Extended Y/N
	R.A.	Dec.			
HCG 62a .....	12 <sup>h</sup> 53 <sup>m</sup> 05.63	−09°12′13″.7	0.8	4158 ± 65	Y
HCG 62b .....	12 <sup>h</sup> 53 <sup>m</sup> 04.43	−09°11′59″.4	0.6	1344 ± 37	Y
HCG 62c .....	12 <sup>h</sup> 53 <sup>m</sup> 09 <sup>s</sup> .76	−09°11′55″.7	4.8	331 ± 19	Y ?
HCG 62d § .....	—	—	—	36 ± 7	Y ?
HCG 62-66 .....	12 <sup>h</sup> 52 <sup>m</sup> 48 <sup>s</sup> .57	−09°13′25″.7	4.2	30 ± 7	Y ?

\* Detected position by the CIAO “wavdetect” task, with 90% confidence position accuracy of 0.6″ radius.

† Positional difference between X-ray and optical.

‡ Observed count within a radius of 10″ in 0.5–4 keV including IGM emission but subtracted by the “blank-sky”.

§ HCG 62d was not detected by the “wavdetect” task, so that the optical position was utilized.

exposure map. The IGM emission is clearly observed, and it is extended around the central galaxy HCG 62a. The brightest region has a radius of about 1′ from HCG 62a.

We searched for discrete X-ray sources in the ACIS-S3 field using the CIAO “wavdetect” task. Choosing a significance parameter of  $10^{-6}$  for images in the energy bands 0.5–10 keV, 0.5–2.0 keV, and 2.0–10.0 keV, we detected 50 sources in total, including HCG 62a, 62b, 62c, and 62-66. We have detected all the point sources previously identified in the SEXSI catalog Harrison et al. 2003 using the same Chandra data. Optical properties of the member galaxies within the Chandra ACIS-S3 field of view are summarized in table 5.1, and the optical image is

shown in figure 5.2 (b). The X-ray detected positions and the ACIS-S3 count are summarized in table 5.2. The X-ray position of HCG 62a and HCG 62b well agree with the optical coordinate given in Zabludoff et al. (2000) Zabludoff & Mulchaey 2000 within  $< 1''$ . However, HCG 62c and HCG 62-66 indicate different positions by about  $5''$  and  $4''$ . This is due probably to the extent of the galaxies and/or to the gas stripping, because the probability of miss-identification of background or foreground object within  $5''$  radius is calculated to be only 1.5%.

The X-ray emission of HCG 62a is dominated by the extended gas, for which we will describe the properties later. The HCG 62b galaxy was also found to be significantly more extended than the point spread function of Chandra. We have fitted the radial brightness profile,  $S(r)$ , of HCG 62b with a single  $\beta$  model,

$$S(r) = S_0 \left[ 1 + (r/R_c)^2 \right]^{-3\beta+1/2}, \quad (5.1)$$

and obtained a core radius,  $R_c = 1.5_{-0.6}^{+1.1}$  arcsec,  $\beta = 0.5_{-0.1}^{+0.2}$ , and the normalization,  $S_0 = 0.8_{-0.3}^{+0.5} \times 10^{-6}$  photons  $\text{cm}^{-2} \text{s}^{-1} \text{arcsec}^{-2}$ . There is also an indication for the HCG 62c galaxy to be extended in the Chandra image in the direction of the optical major axis (north – south), although it is not clear whether it is due to the extended IGM emission because of the poor statistics of HCG 62c. The HCG 62d galaxy was not detected by the “wavdetect” task, however, the “blank-sky” subtracted count exhibited a clear excess when integrated within  $10''$  around the optical position as shown in table 5.2. It is supposed that the extended feature of HCG 62d may have hampered the detection by “wavdetect”.

In the following analysis, the detected sources were excluded except for HCG 62a and HCG 62d. Since HCG 62a and HCG 62b are closely located, we need to separate the HCG 62b component in order to examine the IGM structure. It is notable that the redshift of HCG 62b is smaller than the group redshift of  $z = 0.0145$  by 0.0026 ( $\sim 11$  Mpc), hence HCG 62b is probably not interacting with the IGM around the group core. We produced two radial profiles in 0.5–4 keV band centered on HCG 62a and HCG 62b, and fitted them with a double  $\beta$  (HCG 62a) and a single  $\beta$  (HCG 62b) models, respectively. With these fits, we evaluated the relative intensity of HCG 62b compared with the IGM emission as a function of the distance from HCG 62b. The contamination from HCG 62b becomes less than 10% of the IGM intensity when one goes to outside of a radius of  $10''$ . Thus, we extracted a circle with  $10''$  radius around HCG 62b and carried out the analysis for the IGM emission.

The central HCG 62 image is shown in figure 5.3 (a). This image indicates surface brightness depressions in the northeast and southwest directions at  $20''$ – $30''$  from HCG 62a, the so-called cavities as reported by Vrtilik Vrtilik 2001, Vrtilik et al. 2002. We look into the properties of these cavities in § 5.4.

### 5.3.2 XMM-Newton image

A combined X-ray image taken with MOS1 and MOS2 detectors of XMM-Newton in the 0.5–4 keV energy band is shown in figure 5.3 (b). We corrected for background and exposure, and

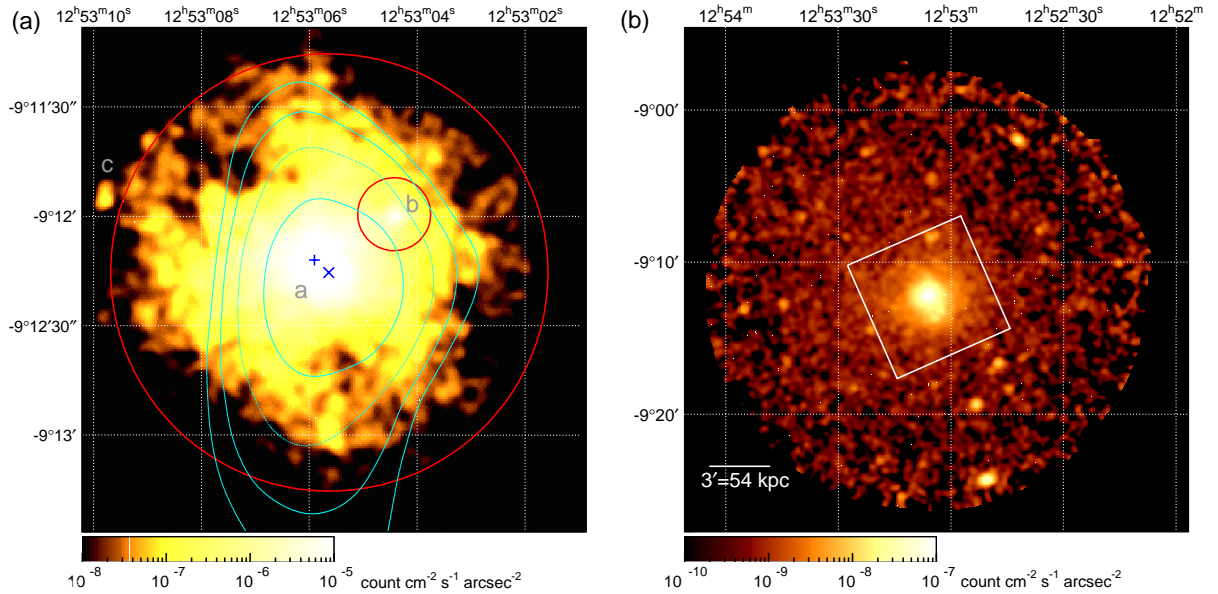


Fig. 5.3: (a) Same as figure 5.2, but the central region of HCG 62 is expanded. The detected point sources other than HCG 62a, 62b and 62c are excluded. The central positions for the 2-dimensional  $2-\beta$  fit are denoted by cross and plus corresponding to the narrower and the wider  $\beta$  components. The red circles indicate a radius of  $1'$  from HCG 62a and  $10''$  from HCG 62b, respectively. The overlaid contour represent a radio intensity map at 1.4 GHz with  $45''$  FWHM resolution, derived from the NRAO VLA Sky Survey (NVSS; Condon et al. 1998). (b) Combined image with MOS1 and MOS2 detectors in the 0.5–4 keV band (J2000). The image is Gaussian smoothed with  $\sigma = 10''$  and corrected for exposure and background. A white square represents the ACIS-S3 field.

performed Gaussian smoothing to the image. The IGM emission is very extended beyond the boundary of the Chandra ACIS-S3 chip shown by a white square. The cavities are not clearly seen because of the poorer spatial resolution. Many point sources were detected in the outer region by the SAS “edetect” task, but none of them outside of  $r = 100''$  were member galaxies of this compact group. Point sources inside of  $100''$  from HCG 62a were excluded using the Chandra data (§ 5.3.1), and the XMM-Newton data were used to mask out the sources outside of  $100''$ .

### 5.3.3 Surface brightness profile

We plot the radial surface brightness profile for the ACIS-S3 ( $r < 4'$ ) and MOS1 ( $1' < r < 14'$ ) around HCG 62a in the energy range of 0.5–4 keV in figure 5.4. In this analysis, only the MOS1 data were used for the XMM-Newton observation because of its low background and good spatial resolution. HCG 62b was excluded with a circle of  $10''$  radius. Background subtraction was carried out separately for each instrument. Mulchaey and Zabludoff (1998) Mulchaey & Zabludoff 1998 report an acceptable fit with a double  $\beta$  model for the ROSAT data. As the first

Table 5.3: Best fit parameters of the radial surface brightness profiles with ACIS-S3 ( $r < 4'$ ) and MOS1 ( $1' < r < 14'$ ) in 0.5–4 keV by the 3- $\beta$  model. First and second components were constrained to have common  $\beta$ . The parameters of  $\beta$  and  $R_c$  of the third component were fixed at the ROSAT result.

	1	2	3
$S_0$ ( $10^{-6}$ photons $\text{cm}^{-2}$ $\text{s}^{-1}$ $\text{arcsec}^{-2}$ )	$0.83^{+0.10}_{-0.08}$	$0.29 \pm 0.03$	$0.0018 \pm 0.0001$
$\beta$ .....	$0.65 \pm 0.02$	$\leftarrow$ (fixed)	$0.63$ (fixed)
$R_c$ (arcmin/kpc) .....	$0.10^{+0.02}_{-0.01}/1.7^{+0.3}_{-0.2}$	$0.48^{+0.04}_{-0.03}/8.5 \pm 0.6$	$9.00/159.08$ (fixed)
$\chi^2/\text{dof}$ .....		$755.39/570$	

Table 5.4: Best fit parameters by the 2-dimensional 2- $\beta$  model for the central region ( $r < 1'$ ) of HCG 62 with ACIS-S3 in 0.5–4 keV.

	1 (narrower)	2 (wider)
$S_0$ ( $10^{-6}$ photons $\text{cm}^{-2}$ $\text{s}^{-1}$ $\text{arcsec}^{-2}$ ) .....	$0.79^{+0.21}_{-0.16}$	$0.63 \pm 0.06$
$\beta$ .....	$0.87^{+0.86}_{-0.29}$	$0.44 \pm 0.01$
$R_c$ (arcmin/kpc) .....	$0.07^{+0.05}_{-0.03}/1.3^{+0.9}_{-0.5}$	$0.18^{+0.02}_{-0.01}/3.1 \pm 0.3$
R.A. (J2000) .....	$12^{\text{h}}53^{\text{m}}05^{\text{s}}63 \pm 0.4''$	$12^{\text{h}}53^{\text{m}}05^{\text{s}}90 \pm 0.4''$
Dec. (J2000) .....	$-09^{\circ}12'15''.5 \pm 0.4''$	$-09^{\circ}12'11''.6 \pm 0.3''$
$\chi^2/\text{dof}$ .....		$132.07/122$

attempt, we fitted the radial profile with the same ROSAT model, however, a large discrepancy was found in the central region around  $r \lesssim 1'$ . We then varied the parameters of the inner  $\beta$  component. The soft background and the hard component are included as fixed constants in the fit. The fit was still unacceptable because of a large discrepancy in the central region. Then, we fitted with a 3- $\beta$  model by adding a narrow component with its  $\beta$  parameter constrained to have the same value with the middle component, and the fit was much improved. The outermost component was fixed to the ROSAT value, because the IGM emission of HCG 62 is much extended over the XMM-Newton field of view, and we could not constrain the parameters.

The fit results are summarized in table 5.3. The derived core radius,  $R_c = 0.48^{+0.04}_{-0.03}$ , for the middle component are consistent with the value,  $R_c = 0.56^{+0.16}_{-0.16}$ , by Mulchaey and Zabludoff (1998) Mulchaey & Zabludoff 1998 with ROSAT PSPC, while their  $\beta = 0.79^{+0.10}_{-0.09}$  is steeper than ours,  $\beta = 0.65 \pm 0.02$ . This is due certainly to the narrow  $\beta$  model component we have introduced, which is required because of the superior angular resolution of Chandra ACIS-S3 than ROSAT PSPC. The obtained  $\chi^2$  value is still large, however addition of yet another (4th)  $\beta$  component does not significantly improve the fit, and the derived  $\beta$  values for the inner two components are close to 3.0 which is obviously too steep. Therefore, we conclude that it is difficult to improve the fit better than the 3- $\beta$  model case described above, due mainly to the

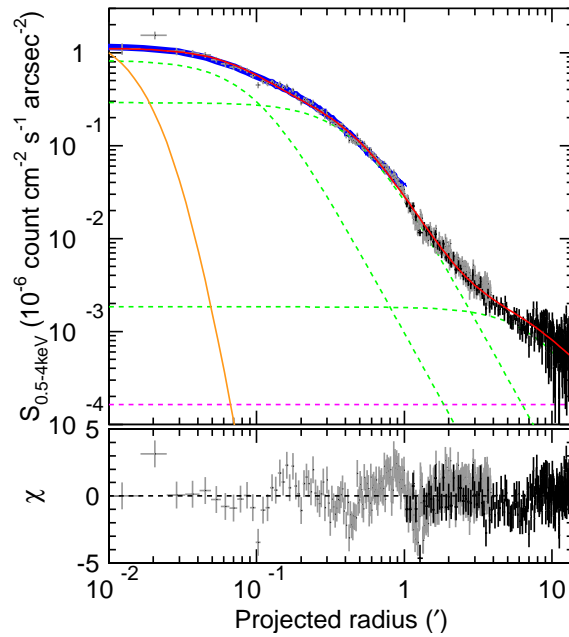


Fig. 5.4: In the upper panel, radial profiles of the surface brightness of HCG 62 in 0.5–4 keV around the central galaxy HCG 62a are plotted for ACIS-S3 ( $r < 4'$ ) and MOS1 ( $1' < r < 14'$ ), as indicated by grey and black lines, respectively. The orange solid line represents the point spread function of Chandra. The best-fit 3- $\beta$  model is shown with red solid line, and the three components are indicated with green dashed lines. For the outermost  $\beta$  component, parameters of  $\beta$  and  $R_c$  are fixed to the ROSAT result by Mulchaey and Zabludoff (1998) Mulchaey & Zabludoff 1998. Intensity for the sum of the soft Galactic and the hard emission is indicated by horizontal magenta dashed line. The blue thick line represents the projected best-fit 2-dimensional double  $\beta$  model obtained with the Chandra image for the central region ( $r < 1'$ ). In the bottom panel, the residuals of the fit are shown in unit of  $\sigma$ .

complicated spatial structure in the central region.

We next carried out a 2-dimensional fitting for the Chandra X-ray image. The ACIS-S3 image shown in figure 5.3 (a) suggests that the brightest position may be slightly offset from the center of the extended group gas. To examine this, we fitted the 2-dimensional image in 0.5–4 keV within  $r < 1'$  around HCG 62a with a 2- $\beta$  model (narrower and wider), whose centers were varied as free parameters. Due to the limited photon count in the image bin, we chose the maximum likelihood method assuming the Poisson statistics in the fitting. The “blank-sky” background were included in the model as a constant surface brightness. The data and the best fit model are projected around the common center (HCG 62a) as shown in figure 5.4. The model (blue thick line) well describes the radial profile within  $r \leq 1'$ , and gives an acceptable fit with  $\chi^2/\text{dof} = 132.07/122$ . The fit parameters are summarized in table 5.4. We find that the centers of the narrower and wider components are different by  $5.44''$  (1.6 kpc). The center of the narrower component is closer to the optical center ( $2''$  offset) than the wider component

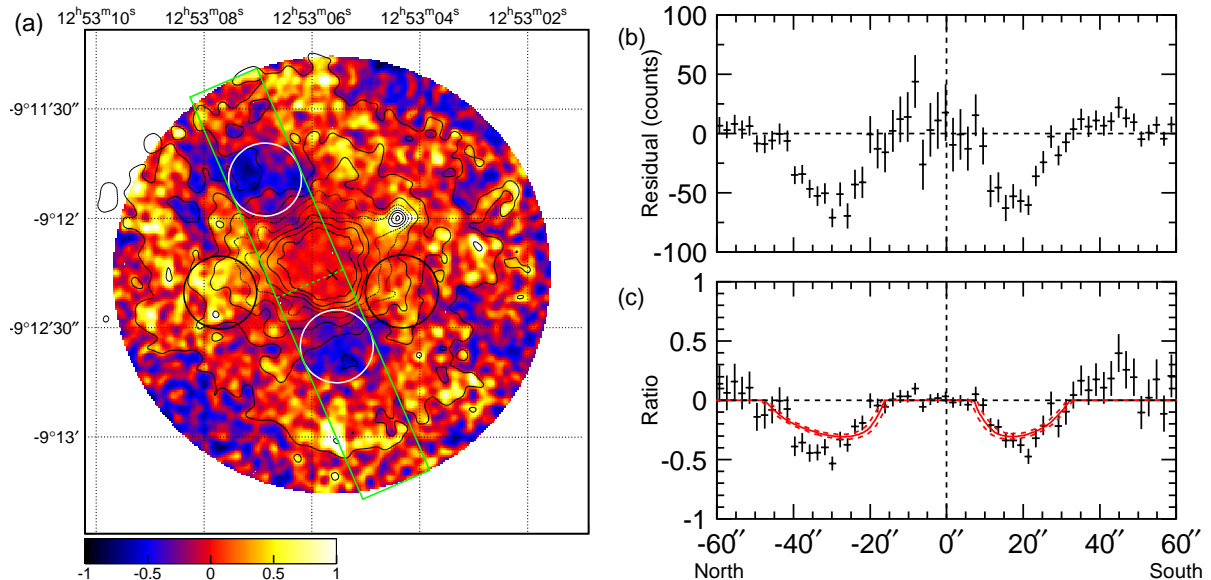


Fig. 5.5: (a) Color-coded map of the relative deviation of the flux from the best-fit  $2\text{-}\beta$  model based on the 2-dimensional fit (table 5.4) in 0.5–4 keV within a radius of  $1'$  around HCG 62a with ACIS-S3 (J2000). X-ray contours shown by thin black lines are the same in figure 5.3 (a). White and black circles with a radius of  $10''$  represent regions where energy spectra are studied. White ones are the cavities, and black ones are non-cavity regions examined for comparison. The distances from HCG 62a to the centers of the east and west light-blue circles are  $20''$  and  $30''$ , the same for the north and south cavities, respectively. (b) Residual of the observed count to the  $2\text{-}\beta$  model along the green rectangular region ( $20'' \times 120''$ ) in (a). (c) Ratio of the residual counts divided by the  $2\text{-}\beta$  model. See text § 5.4.1 for red lines.

( $5''$  offset).

## 5.4 X-ray Cavity

In this section, we look into the X-ray structure and the spectral characteristics of the cavities which are recognized in the Chandra image in figure 5.3 (a). We broadly consider two possibilities for the origin of the cavities as follows; (1) depression of the X-ray flux is resulted by absorption due to some intervening material, and (2) X-ray emitted gas is deficient, possibly being expelled by some process. We will examine the case (1) in § 5.4.2 and (2) in § 5.4.3, respectively.

### 5.4.1 Flux depression & temperature map

To quantify surface brightness depression in the cavity regions, we refer to the result of the  $2\text{-}\beta$  model fit of the 2-dimensional image in § 5.3.3. The relative deviation of the brightness from the  $2\text{-}\beta$  model is color coded and plotted in figure 5.5. Both of the cavity regions show a brightness drop by as much as 50–70% at the bottom as compared with the level of surrounding regions. If

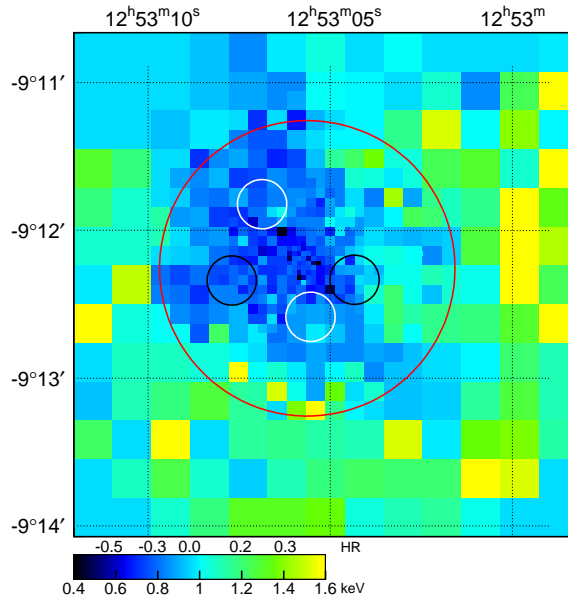


Fig. 5.6: Color coded temperature map (J2000) based on the hardness ratio,  $HR \equiv (H - S)/(H + S)$ , with ACIS-S3, where  $S$  and  $H$  correspond to the 0.5–0.95 keV and 0.95–4 keV counts, respectively. The red circle has a radius of  $1'$  around HCG 62a, and the small circles ( $10''$  in radius) are the same as those in figure 5.5. Typical 90% confidence error on temperature is  $\sim 0.2$  keV above 1 keV and  $\sim 0.1$  keV below 1 keV.

we approximate the cavity shape by a sphere, their radii are  $\sim 10''$  (3 kpc) as indicated by white circles in figure 5.5, with the north one slightly larger. This approximation is similar to the one performed in B04. The distances of the cavity centers from HCG 62a are  $\sim 30''$  (9 kpc) for the north and  $\sim 20''$  (6 kpc) for the south one, respectively. If we take the distances from the central position of the wider component of the 2- $\beta$  model, the cavities are almost symmetrical in their distances  $\sim 25''$  (7.4 kpc). The positions and the distances of both cavities are summarized in table 5.5.

Next, we look into temperature distribution using hardness ratios ( $HR$ ). After the point source and background subtractions, we produced images in two energy bands, 0.5–0.95 keV ( $S$ ) and 0.95–4 keV ( $H$ ), which give nearly the same counts in both energy bands. The  $HR$  is defined as the ratio of the counts between these bands as  $HR \equiv (H - S)/(H + S)$ . We divided the region into small cells whose sizes are determined to contain at least 50 counts in the 0.5–4.0 keV ( $H + S$ ) band, and then the  $HR$  values were calculated. The  $HR$  values were then converted to temperature based on the response matrices at the center of the field of view, assuming an absorption of  $N_H = 3.0 \times 10^{20} \text{ cm}^{-2}$  and a metal abundance of 0.5 solar. Typical 90% confidence error on  $HR$  is  $\sim 0.17$ , which corresponds to  $\sim 0.2$  keV above 1 keV and  $\sim 0.1$  keV below 1 keV. The resultant temperature map is shown in figure 5.6. A clear temperature drop down to  $\sim 0.7$  keV is seen at the central region, which is surrounded by a hotter gas with  $kT \sim 1.4$  keV at a radius greater than  $1'$  (18 kpc). The central cool region shows an irregular shape, with an

Table 5.5: Observed and calculated properties of the north and south cavities and the east and west non-cavities.

	north cavity	east non-cavity	south cavity	west non-cavity
Distance from HCG 62a * . . . . .	31.9''	31.9''	19.7''	19.8''
Distance from group core † . . . . .	26.5''	29.0''	24.1''	24.7''
$HR$ ‡ . . . . .	$-0.13 \pm 0.07$	$-0.21 \pm 0.05$	$-0.10 \pm 0.06$	$-0.12 \pm 0.05$
Integration radius § . . . . .	15.7''	←	12.6''	←
$N_c$ or $N_{nc}$    . . . . .	$2225 \pm 48$	$2857 \pm 58$	$2476 \pm 63$	$3316 \pm 75$
$F_{proj} - F_{sphere}$ or $F_{proj}$ ‡ . . . . .	50.63	64.93	48.31	63.46

\* Position of HCG 62a is assumed to be coincide with the center of the narrower component in table 5.4.

† Position of the group core is assumed to be coincide with the center of the wider component in table 5.4.

‡ Hardness ratio,  $HR \equiv (H - S)/(H + S)$ , within  $r \leq 10''$ , where  $S$  (or  $H$ ) corresponds to 0.5–0.95 (0.95–4) keV counts.

§ Integration radius is chosen to become  $N_c/N_{nc} = (F_{proj} - F_{sphere})/F_{proj}$  for each cavity and non-cavity pair.

||  $N_c$  for north and south cavities, and  $N_{nc}$  for non-cavities. Each value is corrected for background and exposure.

‡  $F_{proj} - F_{sphere}$  for north and south cavities, and  $F_{proj}$  for non-cavities in arbitrary unit.

elongation to the directions of two cavities, although the temperature structure does not simply correlate with the cavity regions.

#### 5.4.2 Spectral comparison between cavity & non-cavity regions

In order to examine the possibility that absorption may be responsible for the cavities, we look into the energy spectra in this subsection. We extracted energy spectra for the two cavity regions from the ACIS-S3 data, using circular regions with the same radius of  $10''$  (3 kpc) as shown in figure 5.5. To compare with them, we also extracted spectra for two non-cavity regions with both  $10''$  radii in the east and west at the same distance from HCG 62a to the respective cavities. Their precise locations are (12h53m06.87s, -9D11'49.4''), (12h53m05.54s, -9D12'35.1''), (12h53m07.75s, -9D12'21.1'') and (12h53m04.33s, -9D12'20.1'') (J2000) for the north, south cavities and east, west non-cavity, respectively. The non-cavity regions are indicated by black circles in figure 5.5, and their properties are summarized in table 5.5. First of all, we calculated the hardness,  $HR$ , as defined in the previous subsection, in these four regions. The derived values with 90% confidence errors were  $-0.130 \pm 0.066$  vs.  $-0.209 \pm 0.052$  for the north cavity vs. east non-cavity pair, and  $-0.099 \pm 0.058$  vs.  $-0.117 \pm 0.046$  for the south cavity vs. west non-cavity pair, respectively. There is no significant difference in the hardness for both pairs. However, both of the cavity regions suggest slightly larger hardness than the respective non-cavity regions, which is in the same sense as expected if absorption is responsible for the X-ray cavities.

To be more quantitative, we conducted a spectral fit for each spectrum. All the spectra were

Table 5.6: Results of spectral fits for the north and south cavity regions and the east and west non-cavity regions within  $r \leq 10''$  in 0.5–3 keV with a two temperature vMekal model. See text § 5.4.2 for details.

	$N_{\text{H,excess}}$ ( $10^{20} \text{ cm}^{-2}$ )	$kT_1$ (keV)	$Norm_1^*$ ( $10^{-19} \text{ cm}^{-5}$ )	$Norm_2^*$	$F_{0.5-4 \text{ keV}}$ ( $10^{-14} \text{ ergs cm}^{-2} \text{ s}^{-1}$ )	$\chi^2/\text{dof}$
phabs ( $N_{\text{H}} = 3.0 \times 10^{20} \text{ cm}^{-2}$ fixed) $\times$ 2- $T$ ( $kT_2 = 1.4 \text{ keV}$ & abundance fixed) vMekal model						
north cavity .....	—	$0.74_{-0.05}^{+0.04}$	$1.3_{-0.2}^{+0.3}$	$0.7_{-0.4}^{+0.4}$	$4.0 \pm 0.3$	18/14
east non-cavity .....	—	$0.75_{-0.05}^{+0.04}$	$2.5_{-0.4}^{+0.4}$	$0.6_{-0.5}^{+0.5}$	$6.8 \pm 0.4$	22/16
south cavity .....	—	$0.76_{-0.06}^{+0.05}$	$1.6_{-0.3}^{+0.3}$	$1.1_{-0.4}^{+0.6}$	$5.2 \pm 0.3$	18/20
west non-cavity .....	—	$0.76_{-0.05}^{+0.04}$	$2.6_{-0.4}^{+0.4}$	$1.3_{-0.7}^{+0.7}$	$8.0 \pm 0.4$	39/32
phabs ( $N_{\text{H}} = 3.0 \times 10^{20} \text{ cm}^{-2}$ fixed) $\times$ zphabs $\times$ 2- $T$ ( $kT_2 = 1.4 \text{ keV}$ & abundance fixed) vMekal model						
north cavity .....	$18.3_{-4.6}^{+5.6}$	$0.70_{-0.02}^{+0.06}$	$2.5_{-0.4}^{+0.6}$	$0.7_{-0.3}^{+0.3}$	$4.2 \pm 0.3$	} 42/31
east non-cavity .....	$2.4_{-2.4}^{+3.3}$	↑	↑	↑	$6.5_{-0.3}^{+0.4}$	
south cavity .....	$11.7_{-2.3}^{+3.6}$	$0.75_{-0.04}^{+0.03}$	$2.5_{-0.3}^{+0.4}$	$1.2_{-0.4}^{+0.4}$	$5.5 \pm 0.3$	} 76/53
west non-cavity .....	$< 2.8$	↑	↑	↑	$7.6 \pm 0.4$	

\* Normalization for the Mekal model,  $Norm = \int n_e n_H dV / (4\pi(1+z)^2 D_A^2)$ , where  $D_A$  is the angular distance to the source.

binned to contain at least 30 counts in a bin. The spectra were then fitted with a two temperature vMekal model (2- $T$  model in § 5.5) in the 0.5–3 keV band with an absorption (phabs in XSPEC) fixed to the Galactic value,  $N_{\text{H}} = 3.0 \times 10^{20} \text{ cm}^{-2}$ . Because of the limited statistics of those spectra, temperature of the hot component,  $kT_2$ , was fixed to 1.4 keV and the abundance of each element was fixed to the best-fit values for the 1- $T$  model in the annulus range of  $0.4 < r < 0.6'$  in table 5.7. See § 5.5 for details of the model. The fit results are summarized in the first four rows of table 5.6.

All of the four spectra are well fitted by the 2- $T$  model with acceptable  $\chi^2$  values at the 90% confidence limit. The obtained temperatures exhibited quite similar values of  $kT_1 = 0.74$ – $0.76 \text{ keV}$ , and we could not find any significant difference between the cavity and non-cavity spectra except for the normalizations of the cool component,  $Norm_1$ . It is interesting that the normalizations of the hot component,  $Norm_2$ , are not different between them. As described in the next section, the hot component is probably absent from the central region of the group ( $r \lesssim 0.6'$ ), so that the hot component seen in these four regions are mostly due to foreground or background emission. It is therefore suggested that the cavities lie close to the group core in our line of sight, and that only the cool component is pushed away from the cavities. The signature of hardening of  $HR$  above is due probably to this effect. As a remark, the fits are not acceptable when fitted with a one temperature vMekal model (1- $T$  model), although the obtained temperatures are also very similar among the four spectra.

Here, we evaluate how much  $N_{\text{H,excess}}$  is needed to reproduce the observed cavity feature by a simple absorption at the source redshift. For this purpose, we simultaneously fitted the cavity

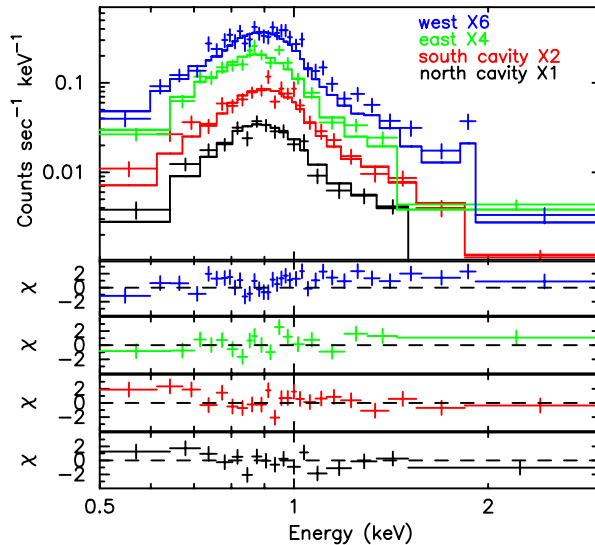


Fig. 5.7: Chandra ACIS-S3 X-ray spectra for north (black) and south (red) cavity regions, and east (green) and west (blue) non-cavity regions, respectively. Spectra of the north cavity and east non-cavity pair and the south cavity and east non-cavity pair are simultaneously fitted with common continuum parameters with individual excess absorption. The spectra and the best-fit models are scaled by 2, 4, 6 for south, east, and west regions, respectively, for clarity. The bottom four panels show the residuals of the fit.

and non-cavity spectra of each pair, by setting all the parameters of the emission spectrum to be the same including the normalization. Thus, two new parameters,  $N_{\text{H,excess}}$  for each pair, and three new constraint on  $Norm_1$ ,  $Norm_2$ , and  $kT_1$  are added, so that the degree of freedom (dof) increases by one. The pulse-height spectra and fit residuals for the four regions are shown in figure 5.7. The  $N_{\text{H,excess}}$  for the individual regions are summarized in the bottom four rows of table 5.6. The obtained  $\chi^2/\text{dof}$  were 42/31 for the north cavity and east non-cavity pair, and 76/53 for the south cavity and west non-cavity pair. Therefore both fits were not acceptable at the 90% confidence limit, although improvement of  $\chi^2$  is marginal for the former pair. The derived  $N_{\text{H,excess}}$  in cavities has to be  $\sim 3$  times larger than those in non-cavity regions for the necessary flux reduction. The required mass of neutral hydrogen for north and south cavities amount to  $1.0 \times 10^9 M_\odot$  and  $0.4 \times 10^9 M_\odot$ , respectively. These values are comparable to the observed upper limit of the  $\text{H I}$  mass,  $\sim 10^9 M_\odot$ , of the whole group including all member galaxies by Verdes-Montenegro et al. (2001) Verdes-Montenegro et al. 2001 and Stevens et al. (2004) Stevens et al. 2004. It is therefore difficult to attribute the cavities to the absorption by neutral gas.

### 5.4.3 Hollow sphere model

Since the absorption model is found to be unlikely in the previous subsection, we then consider an extreme case that a spherical cavity contains no X-ray emitting gas at all, namely, the hollow

sphere model. It is assumed that the spherical cavities exist at the same distance from us to the group core. Even with this extreme assumption, there should be a certain flux observed in the projected circular cavity region because of the foreground and background group emission. This will give us a constraint on the physical size of the cavities. For an overall X-ray structure, we assume that the 3-dimensional X-ray emissivity obeys the 3- $\beta$  model shown in table 5.3. Based on this model, we can estimate the emission from an arbitrary volume in the IGM and the emission from a column integrated along a certain line of sight. Here a single cavity is considered. The observed projected counts corrected for background and exposure at the circular cavity region is denoted by  $N_c$ , and the count in the corresponding non-cavity region by  $N_{nc}$ , respectively. The non-cavity region has the same integration radius and distance from HCG 62a as the cavity region. Then, based on the 3- $\beta$  model, we can calculate the flux,  $F_{\text{sphere}}$ , from the cavity volume which is assumed to be filled with hot gas. The model also gives us the projected flux,  $F_{\text{proj}}$ , from the line-of-sight column passing through the non-cavity region. These numbers allow us to estimate the counts purely emitted from the spherical cavity as,  $N_c - N_{nc} (F_{\text{proj}} - F_{\text{sphere}})/F_{\text{proj}}$ , which should be zero on the assumption above.

Based on the observed cavity flux, we can derive the upper and lower limits for the radius of the hollow spheres. Clearly, too small radius will give too little depression in the X-ray flux at the cavity region, and vice versa. We applied the observed intensity and position of the north and south cavities. The allowed ranges for the radii of the hollow spheres were computed as  $r = 15.7 \pm 0.9''$  and  $r = 12.6 \pm 0.8''$  for the north and south cavities, respectively. These sizes are almost consistent with the projected image as seen in figure 5.5 (a). The observed and the calculated values of  $N_c$ ,  $N_{nc}$ ,  $F_{\text{proj}} - F_{\text{sphere}}$ , and  $F_{\text{proj}}$  are summarized in table 5.5. The expected profile of the count rate deficiency with this assumption is overlaid in figure 5.5 (c) as a solid red line. The dashed red lines correspond to the radii at the  $\pm 90\%$  confidence errors. As seen in this plot, the spherical assumption of cavities gives an asymmetric shape with deeper deficiency at the near side and shallower at the far side, when projected to the 2-dimensional image. Because the observed shapes of the cavities are almost symmetrical, it is suggested that there must be an asymmetry in the shape and/or the density inside the cavities. Namely, the far-side of the cavities should be larger in size and/or weaker in the X-ray emissivity. It is also notable that even with this extreme assumption of hollow spheres at the same distance to the group core, the calculated deepness of the deficiency is nearly the same level or even slightly shallower than the observed ones. This fact implies that the shape of cavities is probably elongated in the direction of our line of sight. Another possibility is that the group gas itself has a flatter shape in the depth, although it is implausible considering the redshift distribution of the member galaxies Zabludoff & Mulchaey 2000 and that the projected X-ray image is quite symmetric.

## 5.5 Radial Profiles of Temperature & Abundance

### 5.5.1 Consistency between Chandra & XMM-Newton

In order to obtain radial profiles of temperature and abundance of the IGM, we examined energy spectra for each instrument (ACIS-S3, MOS1, MOS2, and pn) from several circular annuli from the center of HCG 62a. The center was taken from the narrower component in our 2-dimensional fit carried out in § 5.3.3. First of all, we checked the consistency between Chandra and XMM-Newton using the spectra within  $r \leq 2'$  around HCG 62a. Each spectrum was binned to contain at least 30 counts per bin to be tested with the  $\chi^2$  fit. The background data were taken from the same region in the “blank-sky” data for each instrument. The hard emission and the soft background components are also considered in the fitted model (§ 5.2.3). As for the XMM-Newton data, MOS1 and MOS2 spectra were summed up and simultaneously fitted with the pn spectrum. The energy range around the Al- $K_\alpha$  line (1.4867 keV), the instrumental background, was ignored for both MOS and pn.

We have fitted the spectra with a single temperature or two temperature vMekal model including the Galactic photoelectric absorption. Abundances of C, N, Na, and Al were fixed to be 1 solar. We grouped several elements and constrained them to have a common abundance. The first group contains O and Ne, the second group S, Ar and Ca, and the third group is for Fe and Ni. Among the other elements, abundances of Mg and Si were determined separately. In the case of the two temperature fit, we used the sum of two vMekal models in which two components were constrained to have common abundances. The actual model formula are  $\text{phabs} \times (\text{vMekal} + \text{powerlaw}) + \text{Mekal}$  (1- $T$  model) and  $\text{phabs} \times (\text{vMekal} + \text{vMekal} + \text{powerlaw}) + \text{Mekal}$  (2- $T$  model). Here, phabs represents photoelectric absorption and  $N_{\text{H}}$  is fixed at the Galactic value of  $3.0 \times 10^{20} \text{ cm}^{-2}$ . The Mekal component is the soft background described in § 5.2.3, with  $kT$  and  $Z$  both fixed at 0.3 keV and 1 solar, respectively, and with the fixed normalization. The power-law represents the hard emission described in § 5.2.3 with its photon index,  $\Gamma = 1.5$ , and normalization both fixed.

The  $r \leq 2'$  spectra are shown in figure 5.8 (a), and the fit results with 2- $T$  model are summarized in table 5.7. The 1- $T$  model was rejected at high significance with  $\chi^2/\text{dof} = 2162/425$  (combined) for this region. Three kinds of the fit results are listed in table 5.7, Chandra (ACIS-S3) only, XMM-Newton (MOS1+2, pn) only, and the combined fit of all the instruments. We have confirmed that most of the results from different instruments were consistent at the 95% confidence limit. The abundances with ACIS-S3 were slightly larger than, but mostly consistent with those with XMM-Newton, while only Si gave inconsistent values at the 95% confidence limit. This is due probably to the systematic effect by the intrinsic Si line as seen in the “blank-sky” data for both Chandra and XMM-Newton. Since the Si line is most prominent in the IGM spectrum, the good statistics result in formally inconsistent abundance values. In the annular range of 2–4', spectral fit for individual instruments (ACIS-S3, MOS1+2, and pn) gave consis-

Table 5.7: Results of the projected spectral fit for  $r \leq 2'$  region with two temperature vMekal and vAPEC models.

	$kT_1$ (keV)	$kT_2$ (keV)	O, Ne (solar)	Mg, Al (solar)	Si (solar)	S, Ar, Ca (solar)	Fe, Ni (solar)	$Norm_1^*$ ( $10^{-18} \text{ cm}^{-5}$ )	$Norm_2^*$	$\chi^2/\text{dof}$
vMekal										
Chandra	$0.72^{+0.02}_{-0.02}$	$1.32^{+0.05}_{-0.06}$	$0.36^{+0.12}_{-0.13}$	$1.20^{+0.23}_{-0.19}$	$1.23^{+0.19}_{-0.14}$	$0.86^{+0.38}_{-0.29}$	$0.89^{+0.09}_{-0.08}$	$6.6^{+1.2}_{-1.0}$	$9.3^{+1.3}_{-1.3}$	189/144
XMM	$0.77^{+0.02}_{-0.05}$	$1.41^{+0.12}_{-0.11}$	$0.23^{+0.17}_{-0.13}$	$1.01^{+0.37}_{-0.30}$	$0.76^{+0.19}_{-0.15}$	$0.67^{+0.26}_{-0.23}$	$0.81^{+0.16}_{-0.12}$	$7.2^{+1.8}_{-1.7}$	$8.5^{+2.0}_{-1.3}$	316/270
combined	$0.74^{+0.02}_{-0.03}$	$1.36^{+0.06}_{-0.06}$	$0.33^{+0.12}_{-0.10}$	$1.16^{+0.18}_{-0.16}$	$0.95^{+0.12}_{-0.10}$	$0.75^{+0.20}_{-0.19}$	$0.86^{+0.08}_{-0.07}$	$6.8^{+0.8}_{-0.7}$	$8.8^{+1.3}_{-1.3}$	821/423
vAPEC										
Chandra	$0.77^{+0.02}_{-0.02}$	$1.33^{+0.15}_{-0.07}$	$0.41^{+0.19}_{-0.13}$	$1.20^{+0.22}_{-0.19}$	$1.18^{+0.17}_{-0.15}$	$1.21^{+0.37}_{-0.34}$	$0.91^{+0.14}_{-0.08}$	$7.7^{+0.9}_{-0.9}$	$7.8^{+0.3}_{-1.1}$	158/144
XMM	$0.79^{+0.01}_{-0.01}$	$1.47^{+0.11}_{-0.11}$	$0.30^{+0.34}_{-0.22}$	$0.97^{+0.44}_{-0.32}$	$0.76^{+0.23}_{-0.17}$	$0.71^{+0.29}_{-0.25}$	$0.85^{+0.22}_{-0.16}$	$7.4^{+2.1}_{-1.9}$	$7.7^{+1.0}_{-1.0}$	311/270
combined	$0.78^{+0.01}_{-0.01}$	$1.43^{+0.07}_{-0.07}$	$0.40^{+0.15}_{-0.12}$	$1.15^{+0.10}_{-0.17}$	$0.93^{+0.12}_{-0.11}$	$0.86^{+0.21}_{-0.20}$	$0.90^{+0.09}_{-0.08}$	$7.7^{+0.7}_{-0.7}$	$7.5^{+0.5}_{-0.5}$	795/423

\* Normalization for the Mekal model,  $Norm = \int n_e n_H dV / (4\pi(1+z)^2 D_A^2)$ , where  $D_A$  is the angular distance to the source.

tent results at the 90% confidence limit, due mainly to the poorer statistics. Based on these results, data from all the instruments were simultaneously fitted in the following analysis.

### 5.5.2 Mekal vs APEC model & notes on abundance

We also summarize results when the spectra are fitted with  $\text{phabs} \times (\text{vAPEC} + \text{vAPEC} + \text{powerlaw}) + \text{Mekal}$  (2- $T$  vAPEC model) in table 5.7. The vAPEC model (v1.3.1) gives smaller  $\chi^2$  value especially for the Chandra spectrum, and indicates slightly higher temperatures by  $\Delta T \lesssim 0.05$  keV than the vMekal model. This is due probably to the better modeling of the Fe-L line complex in the vAPEC model, however it is confirmed that all the element abundances are consistent within 90% confidence errors between the two models. We therefore adopt the vMekal model in the following analysis considering comparison with previous literatures.

Table 5.8 represents a result when all the element abundances in the vMekal or vAPEC model are determined separately for the combined fit. The errors of the Ne, Al, Ar, Ca, and Ni abundances are significantly larger than those of other elements, while other parameters agree with the values in table 5.7 within 90% confidence errors. Thus abundances in table 5.7, which are linked together for (O, Ne), (Mg, Al), (S, Ar, Ca), and (Fe, Ni), are essentially representing O, Mg, S, and Fe abundances, respectively. There is an indication that the Ni abundance is higher than the Fe abundance in both vMekal and vAPEC model fits. This might be explained by the fact that the fitted spectra are not deprojected so that they contain emission from outer region in the group which exhibits higher temperature than the group core as seen in §5.5.4. On the other hand, it is known that Ni is synthesized more abundantly than Fe in SN Ia when compared in the solar unit, which will be discussed in §5.7.

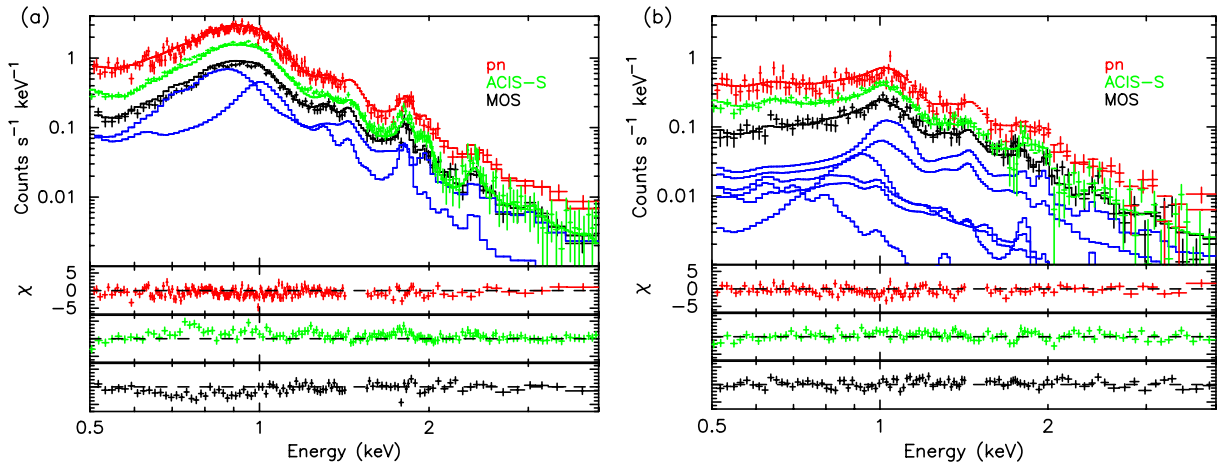


Fig. 5.8: (a) Chandra ACIS-S3 (green), MOS1+2 (black), and pn (red) spectra within  $r \leq 2'$  around HCG 62a in the 0.5–4 keV band. The three spectra are simultaneously fitted with 2- $T$  model without deprojection, and the best-fit models are indicated by solid lines. Each component of the two temperature vMekal model for MOS1+2 is indicated by blue lines. The bottom three panels show the residuals of the fit. (b) Same as (a), but in the 2–4' annulus fitted with the deprojected 2- $T$  model. The outer contributions and fitting models for MOS1+2 are indicated by blue lines.

Table 5.8: Same as table 5.7, besides the element abundances are determined separately for the combined fit.

	$kT_1$	$kT_2$	O	Mg	Si	S	Fe	$Norm_1$	$Norm_2$	$\chi^2/\text{dof}$
	(keV)	(keV)	(solar)	(solar)	(solar)	(solar)	(solar)	$(10^{-18} \text{ cm}^{-5})$		
vMekal	$0.71^{+0.02}_{-0.01}$	$1.31^{+0.14}_{-0.07}$	$0.37^{+0.11}_{-0.10}$	$1.17^{+0.21}_{-0.18}$	$1.06^{+0.16}_{-0.14}$	$1.01^{+0.28}_{-0.25}$	$0.86^{+0.08}_{-0.08}$	$6.2^{+0.8}_{-0.6}$	$8.3^{+1.0}_{-1.3}$	801/418
vAPEC	$0.78^{+0.01}_{-0.01}$	$1.44^{+0.08}_{-0.09}$	$0.42^{+0.11}_{-0.09}$	$1.13^{+0.23}_{-0.17}$	$0.95^{+0.16}_{-0.11}$	$0.98^{+0.26}_{-0.22}$	$0.83^{+0.11}_{-0.09}$	$8.1^{+1.1}_{-1.2}$	$6.9^{+0.7}_{-0.8}$	783/418
			Ne	Al	Ar	Ca	Ni			
vMekal			$0.49^{+0.50}_{-0.45}$	$2.70^{+1.38}_{-1.32}$	$0.67^{+1.02}_{-0.67}$	$0.88^{+2.12}_{-0.88}$	$2.33^{+0.77}_{-0.70}$			
vAPEC			$0.72^{+0.34}_{-0.29}$	$1.89^{+1.41}_{-1.21}$	$0.72^{+1.01}_{-0.72}$	$0.00^{+1.73}_{-0.00}$	$1.80^{+0.84}_{-0.69}$			

### 5.5.3 Deprojection analysis

We conducted a deprojection analysis using energy spectra from several circular annuli from the center of HCG 62a. The inner and outer radii of the annuli were  $r = 0-0.2'$ ,  $0.2-0.4'$ ,  $0.4-0.6'$ ,  $0.6-1'$ ,  $1-2'$ ,  $2-4'$ ,  $4-8'$ , and  $8-14'$ , in which  $r$  represents the projected radius. The Chandra ACIS-S3 data were used in the range of  $r \leq 4'$ , and the XMM-Newton data were used in  $2' \leq r \leq 14'$ . Therefore, only the annulus of 2–4' was simultaneously examined by both satellites. The spectra for  $0.2' \lesssim r \lesssim 1'$  include two cavities. Since the temperature and abundance of the two cavities are consistent with that in the non-cavity region as shown previously (§ 5.4.2), we did not exclude the cavity region and simply analyzed the annular spectra. Extraction of each spectrum and the treatment of the background are conducted in the same way as described in § 5.5.1.

Spherical symmetry was assumed in the deprojection procedure. Starting from the outermost

Table 5.9: Fractional contribution of the outer shells to the inner shells in the deprojection analysis.

	4–8′	2–4′	1–2′	0.6–1′	0–0.6′
8–14′ .....	0.373	0.075	0.018	0.004	0.002
4–8′ .....	—	0.273	0.056	0.012	0.007
2–4′ .....	—	—	0.273	0.048	0.026
1–2′ .....	—	—	—	0.238	0.109
0.6–1′ ....	—	—	—	—	0.531

region, we fitted the projected annular spectrum with 1- $T$  or 2- $T$  model. Spectrum of the neighboring inner region was then fitted with a model which contained contribution from the outer regions with fixed model parameters at their best-fit values. We repeated this procedure until the innermost region was reached. Because the outer contributions are fixed in the inner model fitting, the propagation of errors is ignored in this method. However, the inner regions are always brighter than outer regions, hence this effect is negligible. Table 5.9 summarizes the fractional contribution of the outer shells to the inner shells. For example, the spectrum of the 4–8′ annulus was fitted with adding 37.3% flux of the best-fit model in the 8–14′ annulus.

Without the deprojection, the metal abundance of the group center ( $r \lesssim 1'$ ) is underestimated by about 30%, while the temperature does not change significantly. The sample spectra in the 2–4′ annulus fitted with the deprojected 2- $T$  model are shown in figure 5.8 (b), and the fit results are summarized in table 5.10. Figures 5.9 & 5.10 show the result of the deprojection analysis, and the 1- $T$  results are quite similar to the previous ASCA result Finoguenov & Ponman 1999.

#### 5.5.4 Temperature profile

The temperature profiles obtained by both the 1- $T$  and 2- $T$  models with the deprojection analysis are shown in figure 5.9. For the radius range  $0.6 < r < 2.0'$ , the 2- $T$  model gives significantly lower  $\chi^2$  values ( $\chi^2 = 78, 68$  for 0.6–1.0′, 1.0–2.0′, respectively) than the 1- $T$  model ( $\chi^2 = 159, 126$ ). The significance was tested with the  $F$ -test, and the 2- $T$  model was preferred with a significance higher than  $5\sigma$ . Within  $r < 0.6'$ , the 2- $T$  model is preferred for the whole 0.0–0.6′ data by  $\Delta\chi^2 = 26$  (99.9% confidence with  $F$ -test), while the 1- $T$  model is also acceptable when we split the region into smaller annuli, 0.0–0.2′, 0.2–0.4′, and 0.4–0.6′. Furthermore, we have also tried the 2- $T$  model for the spectra in the range 0–0.2′ and 0.2–0.4′, but the normalization of the second component turned out to be nil. This is due probably to the poorer statistics for the smaller annuli and also to the fact that the cooler component is dominant in the central region. In the outer regions of  $r > 2'$ , the  $\chi^2$  values for the 2- $T$  model were also lower than the 1- $T$  case, but both of the fit were acceptable. For the outermost range 8–14′, the 2- $T$  model gave similar temperatures for the hotter and cooler components within errors, therefore the 1- $T$  fit turned out to be just enough. This is because the hot component dominates the surface brightness.

Table 5.10: Results of the deprojected spectral fit with 1- $T$  and 2- $T$  vMekal models. The Chandra data (ACIS-S3) are used for 0–4', and the XMM-Newton (MOS1+2, pn) data are used for 2–14'.

$r$ (arcmin)	$kT_1$ (keV)	$kT_2$ (keV)	O, Ne (solar)	Mg, Al (solar)	Si (solar)	S, Ar, Ca (solar)	Fe, Ni (solar)	$Norm_1^*$ ( $10^{-18}$ cm $^{-5}$ )	$Norm_2^*$	$\chi^2/\text{dof}$
1- $T$ vMekal model										
Chandra results										
0.0–0.6	$0.73 \pm 0.01$	—	$0.45^{+0.18}_{-0.14}$	$1.20^{+0.39}_{-0.29}$	$1.10^{+0.34}_{-0.26}$	< 0.49	$0.76^{+0.16}_{-0.10}$	$4.6^{+1.0}_{-1.2}$	—	177/96
0.0–0.2	$0.67 \pm 0.02$	—	$0.47^{+0.49}_{-0.26}$	$1.30^{+1.12}_{-0.60}$	$0.63^{+0.75}_{-0.51}$	< 1.03	$0.74^{+0.44}_{-0.20}$	$1.2^{+0.6}_{-0.7}$	—	75/57
0.2–0.4	$0.70^{+0.03}_{-0.02}$	—	$0.37^{+0.53}_{-0.26}$	$1.61^{+1.52}_{-0.70}$	$1.53^{+1.43}_{-0.73}$	< 1.47	$0.80^{+0.58}_{-0.23}$	$1.2^{+0.6}_{-0.8}$	—	96/66
0.4–0.6	$0.77 \pm 0.03$	—	$0.73^{+1.17}_{-0.49}$	$1.28^{+1.95}_{-0.97}$	$1.79^{+2.14}_{-1.03}$	1.53 †	$1.13^{+0.98}_{-0.37}$	$0.7 \pm 0.3$	—	67/67
0.6–1.0	$0.84 \pm 0.01$	—	$0.27^{+0.23}_{-0.17}$	$1.53^{+0.65}_{-0.46}$	$1.52^{+0.56}_{-0.40}$	< 0.67	$0.78^{+0.21}_{-0.13}$	$2.7^{+0.5}_{-0.5}$	—	159/92
1.0–2.0	$1.12 \pm 0.01$	—	$0.03^{+0.13}_{-0.03}$	$0.71^{+0.31}_{-0.28}$	$0.70^{+0.20}_{-0.18}$	$0.49^{+0.51}_{-0.47}$	$0.48^{+0.06}_{-0.05}$	$6.2^{+0.6}_{-0.7}$	—	126/72
2.0–4.0	$1.37^{+0.03}_{-0.04}$	—	$0.02^{+0.25}_{-0.02}$	$0.35^{+0.53}_{-0.35}$	$0.99^{+0.40}_{-0.34}$	$0.55^{+0.76}_{-0.55}$	$0.52^{+0.10}_{-0.08}$	$5.6^{+0.8}_{-1.0}$	—	128/108
XMM-Newton results										
2.0–4.0	$1.43^{+0.17}_{-0.05}$	—	< 0.67	$0.47^{+1.02}_{-0.47}$	$0.68^{+0.34}_{-0.28}$	$0.54^{+0.50}_{-0.47}$	$0.41^{+0.18}_{-0.08}$	$5.6^{+0.8}_{-1.2}$	—	241/199
4.0–8.0	$1.41^{+0.08}_{-0.07}$	—	$0.12^{+0.37}_{-0.12}$	$0.58^{+0.76}_{-0.58}$	$0.25^{+0.24}_{-0.22}$	< 0.15	$0.26^{+0.07}_{-0.06}$	$10.9^{+1.3}_{-1.4}$	—	164/156
8.0–14.0	$0.64 \pm 0.03$	—	$0.24^{+0.08}_{-0.07}$	$0.06^{+0.10}_{-0.06}$	$0.08^{+0.09}_{-0.08}$	$0.40^{+0.53}_{-0.40}$	$0.04^{+0.01}_{-0.01}$	$47.4^{+9.8}_{-8.9}$	—	188/180
combined results										
2.0–4.0	$1.39 \pm 0.03$	—	< 0.21	$0.40^{+0.49}_{-0.40}$	$0.79^{+0.27}_{-0.23}$	$0.57^{+0.45}_{-0.42}$	$0.47^{+0.08}_{-0.06}$	$5.6^{+0.4}_{-0.6}$	—	415/314
2- $T$ vMekal model										
Chandra results										
0.0–0.6	$0.66^{+0.03}_{-0.22}$	$0.92^{+0.18}_{-0.47}$	$0.39^{+0.24}_{-0.14}$	$1.21^{+0.61}_{-0.31}$	$1.18^{+0.54}_{-0.29}$	< 1.05	$0.84^{+0.31}_{-0.12}$	$3.1^{+0.7}_{-2.0}$	$1.4^{+2.8}_{-0.7}$	151/94
0.6–1.0	$0.77^{+0.04}_{-0.07}$	$1.36^{+0.47}_{-0.20}$	$0.42^{+0.56}_{-0.27}$	$1.92^{+1.45}_{-0.79}$	$2.25^{+1.37}_{-0.74}$	$1.02^{+2.09}_{-1.02}$	$1.40^{+0.75}_{-0.39}$	$1.1^{+0.5}_{-0.4}$	$1.0^{+0.5}_{-0.3}$	78/90
1.0–2.0	$0.83^{+0.06}_{-0.15}$	$1.36^{+0.19}_{-0.11}$	$0.29^{+0.33}_{-0.24}$	$1.20^{+0.76}_{-0.58}$	$1.08^{+0.52}_{-0.39}$	$1.24^{+1.14}_{-0.89}$	$0.99^{+0.31}_{-0.22}$	$0.7^{+0.5}_{-0.4}$	$2.8^{+0.8}_{-1.0}$	69/70
2.0–4.0	$0.85^{+0.29}_{-0.23}$	$1.59^{+0.69}_{-0.20}$	$0.14^{+0.57}_{-0.14}$	$1.05^{+1.25}_{-0.87}$	$2.02^{+1.16}_{-0.74}$	$1.48^{+1.71}_{-1.25}$	$1.11^{+0.54}_{-0.33}$	$0.3^{+0.9}_{-0.2}$	$3.2^{+0.8}_{-0.9}$	121/106
XMM-Newton results										
2.0–4.0	$0.90^{+0.27}_{-0.21}$	$1.83^{+0.51}_{-0.22}$	$0.16^{+1.24}_{-0.16}$	$2.13^{+3.95}_{-1.86}$	$1.57^{+1.68}_{-0.70}$	$1.07^{+1.32}_{-0.84}$	$1.02^{+1.06}_{-0.38}$	$0.3^{+0.6}_{-0.2}$	$3.2^{+1.0}_{-1.1}$	235/197
4.0–8.0	$0.24^{+0.08}_{-0.04}$	$1.40^{+0.08}_{-0.06}$	$0.13^{+0.19}_{-0.10}$	$1.04^{+0.89}_{-0.71}$	$0.39^{+0.31}_{-0.25}$	< 0.22	$0.32^{+0.11}_{-0.09}$	$3.2^{+3.3}_{-1.7}$	$10.4^{+1.7}_{-1.7}$	153/154
8.0–14.0	$0.43^{+0.51}_{-0.09}$	$0.89^{+0.13}_{-0.56}$	$0.19^{+0.10}_{-0.08}$	$0.07^{+0.17}_{-0.07}$	$0.10^{+0.12}_{-0.10}$	$0.31^{+0.52}_{-0.31}$	$0.06^{+0.05}_{-0.02}$	$23.9^{+21.5}_{-11.5}$	$22.9^{+12.4}_{-11.5}$	185/178
combined results										
2.0–4.0	$0.89^{+0.23}_{-0.12}$	$1.71^{+0.48}_{-0.15}$	$0.13^{+0.47}_{-0.13}$	$1.23^{+1.10}_{-0.82}$	$1.68^{+0.74}_{-0.52}$	$1.23^{+0.88}_{-0.70}$	$1.05^{+0.39}_{-0.26}$	$0.4^{+0.6}_{-0.1}$	$3.3^{+0.6}_{-0.7}$	402/312

\* Normalization for the vMekal model,  $Norm = \int n_e n_H dV / (4\pi(1+z)^2 D_A^2)$ , where  $D_A$  is the angular distance to the source.

† The S abundance was fixed to the best fit in calculating errors due to an unresolved problem on XSPEC for this particular fit.

For the 1- $T$  model, the temperature rises from  $kT = 0.7$  keV at the center to  $kT = 1.4$  keV at larger radii, which is consistent with the previous deprojection analysis for the ASCA data Finoguenov & Ponman 1999 and the ROSAT temperature profile by Buote (2000a) Buote 2000a. This profile in  $r < 2'$  is also seen in the temperature map calculated from the  $HR$  (figure 5.6). The temperature with the 1- $T$  model drops again at  $r > 8'$  from the intermediate level of  $kT = 1.4$  keV, as shown in figure 5.9. The temperature drop in our data is much steeper than those reported by Finoguenov & Ponman (1999) Finoguenov & Ponman 1999 with ASCA and

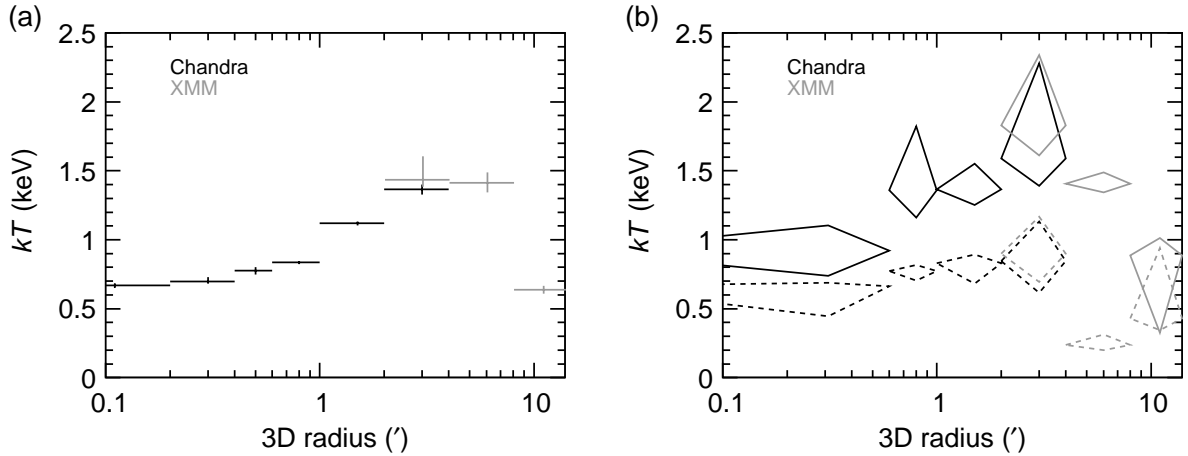


Fig. 5.9: (a) Temperature profiles with the 1- $T$  vMekal models based on the deprojected spectral fit. ACIS-S3 (black) is used for  $r < 4'$ , and MOS1, MOS2, and pn (gray) are used for  $2' < r < 14'$ . (b) Same as (a), but with the 2- $T$  vMekal models.

by Buote (2000a) Buote 2000a with ROSAT. The ROSAT temperature at  $r > 8'$  is  $kT = 0.9$ – $1.0$  keV, while ours is  $kT = 0.66 \pm 0.03$  keV. The influence of the background has been tested by changing the background level within  $\pm 5\%$ , and we found that the best fit temperature varied in  $0.64$ – $0.70$  keV. We have looked into the effects of point source contamination and the influence of hard and soft components, though none of them gives significant change in temperature.

For the 2- $T$  model, temperature of the cooler component is nearly constant at  $\sim 0.7$  keV, which is very close to the central temperature obtained with the 1- $T$  fit. Temperature of the hotter component is also nearly constant at  $\sim 1.4$  keV up to  $r \sim 8'$ . These features are consistent with the ASCA results, which indicate two temperature components at 0.7 keV and 1.4 keV based on projected spectra within  $r < 3'$  Buote 2000b. The cool component is concentrated in the center and dominant within  $1'$ , while the hot component extends out to  $\sim 4'$ . The extent of the cool component will be examined in § 5.6 more quantitatively.

### 5.5.5 Abundance profile

The metal abundances were derived from the deprojected spectra based on the 1- $T$  and 2- $T$  fits. The Fe, Si, and Mg abundances are around one solar or more in  $r < 4'$ . On the other hand, the O abundance is always lower than the solar value (table 5.10 and figure 5.10). We could poorly constrain the S abundance due to the limited statistics. The 2- $T$  fit gave significantly higher abundance than the 1- $T$  fit in the intermediate range of  $1.0' < r < 4.0'$ , while similar abundances between 1- $T$  and 2- $T$  are obtained for the inner ( $r < 1.0'$ ) and outer ( $4.0' < r$ ) regions. Such discrepancy is often seen in the spectral fit, because the abundance takes the lowest value at the temperature where the line emissivity is the highest. This situation corresponds to the case of 1- $T$  fit, and the 2- $T$  model tends to shift the temperature away from such a high emissivity position. The ASCA spectra of HGG 62 are fitted with the 1- $T$  Mekal model by Finoguenov and

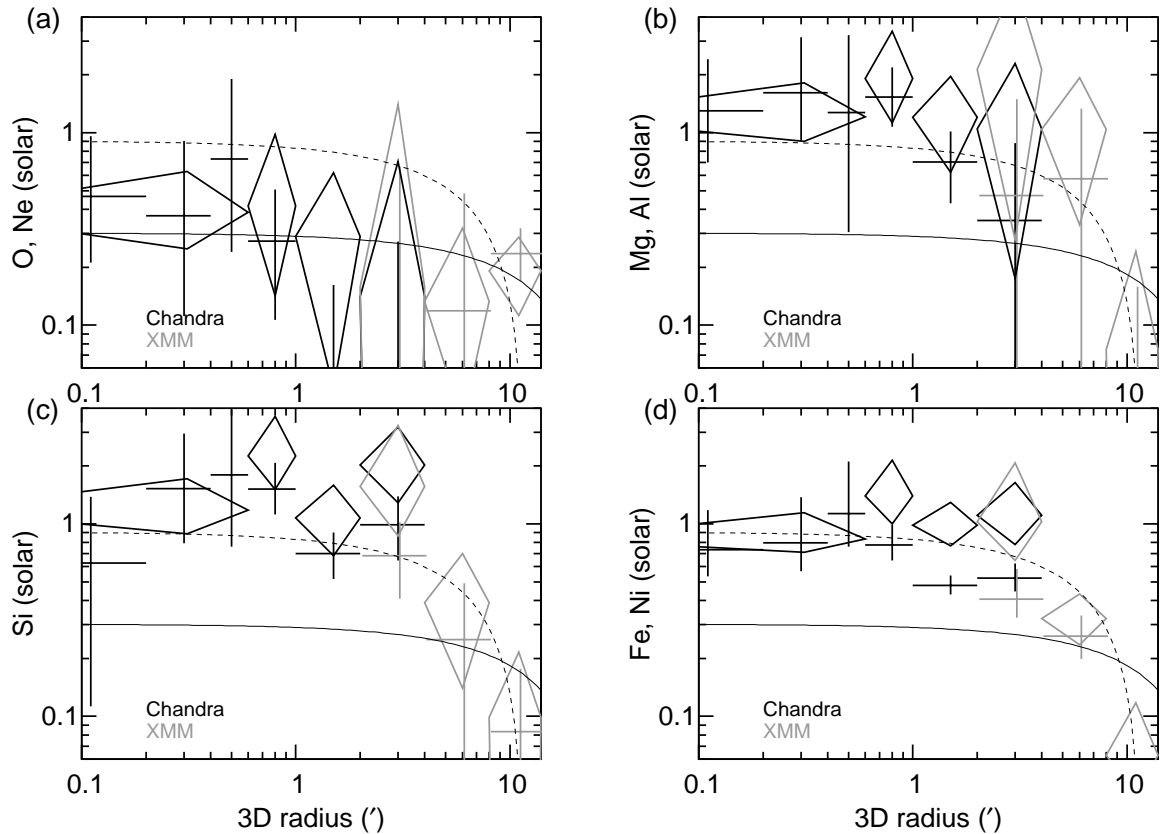


Fig. 5.10: Abundance profiles of O (with Ne) (a), Mg (b), Si (c), and Fe (with Ni) (d) using the 1- $T$  (crosses) and 2- $T$  (diamonds) vMekal models with the deprojection analysis. The ACIS-S3 (black) is used for  $r < 4'$ , and MOS1, MOS2, and pn (gray) for  $2' < r < 14'$ . The solar photospheric value of  $[\text{Fe}/\text{H}] = 4.7 \times 10^{-5}$  Anders & Grevesse 1989 is adopted for the Fe abundance. The solid and dashed lines correspond to the best fit relations of the deprojected O and Fe profile of the 2- $T$  results, respectively.

Ponman (1999) Finoguenov & Ponman 1999, and the present results for Fe, Si, and Mg with 1- $T$  fits are in good agreement with the ASCA deprojection results within the 90% confidence limit at  $r > 1'$ ,

In figure 5.10, the solid and dashed lines correspond to the best fit relations of the deprojected O (a) and Fe (d) profile of the 2- $T$  results, respectively. A simple linear model of  $Z = -a r + b$  is assumed for each profile. These best fit relations are overlaid to all the four plots for comparison. O abundance of  $\sim 0.3$  solar is significantly lower than the other elements. It also indicates a flatter profile, though significance is low due to the low abundance of oxygen. The decline of Fe, Si, and Mg abundances with radius previously reported by Finoguenov and Ponman (1999) Finoguenov & Ponman 1999 with ASCA, is also confirmed with Chandra and XMM-Newton. Our result shows that Fe, Si, and Mg abundances are 1–2 solar at the center and drop to about 0.1 solar at  $r \sim 10'$ . These abundance levels are about twice larger than the values derived with the ASCA spectra ( $\sim 0.6$  solar by Finoguenov & Ponman 1999). This is due primarily to the

much better angular resolution of the Chandra X-ray telescope ( $0.5''$ ) than ASCA ( $3'$ ) at the very central region. In addition, our  $2-T$  model gives higher abundances in the intermediate range of  $1.0' < r < 4.0'$ . As described in §5.5.4, the  $2-T$  model is significantly needed in this region, so that the ASCA abundances are likely to be underestimated. We also note that many authors recently take the solar abundance to be the value given by Grevesse & Sauval et al. (1998) Grevesse & Sauval 1998, i.e.  $[\text{Fe}/\text{H}] = 3.2 \times 10^{-5}$ , which is obtained from the measurements of solar system meteorites. The solar photospheric value of  $[\text{Fe}/\text{H}] = 4.7 \times 10^{-5}$  Anders & Grevesse 1989, which is adopted in our analysis, gives the Fe abundance approximately by a factor of 1.47 smaller. Considering this effect, all the Fe, Si, and Mg abundances have similar value around 1.2 solar at the center ( $r < 0.6'$ ).

## 5.6 Mass Profiles

### 5.6.1 Formulation of two-phase gas

Based on the radial distributions of the cool and hot components, we will derive mass distributions of gas and dark matter. Since the estimated gas mass contained in a single cavity volume, if it is filled up, is  $\sim 6\%$  of the mass in the shell of  $7'' < r < 32''$ , the assumption of the spherical symmetry gives relatively small errors. However, because two temperatures are required for each shell within the deprojected radius of  $0.6' - 4.0'$  as seen in the previous section, we need an additional assumption between the hot and cool components. Here we assume a pressure balance between the two phase, i.e.  $P_{\text{gas}} = n_1 kT_1 = n_2 kT_2$ , where  $n_1$ ,  $n_2$ ,  $T_1$  and  $T_2$  are the cool and hot gas densities and temperatures, respectively, at each 3-dimensional radius of  $R$ . Such a pressure balance is previously adopted by Ikebe et al. (1999) Ikebe et al. 1999 for the Centaurus cluster, and by Xue et al. (2004) Xue et al. 2004 for the RGH 80 galaxy group.

We also introduce a volume filling factor,  $f(R)$ , of the cool component, namely a fractional volume,  $V_1 \equiv fV$ , in the total volume,  $V$ , is filled with the cool gas, and  $V_2 \equiv (1 - f)V$  is filled with the hot gas. This means that the cool and hot gas are not completely mixed, instead the cool component is somewhat patchy or localized with rather an irregular shape. Such a hypothesis may be supported by the 2-dimensional temperature map (figure 5.6) and the existence of the cavities.

Because the normalizations of the  $2-T$  vMekal models are expressed as  $Norm_1 = C_{12} n_1^2 V_1$  and  $Norm_2 = C_{12} n_2^2 V_2$  using a certain common constant,  $C_{12}$ , the volume filling factor,  $f(R)$ , can be solved under the pressure balance as,

$$f(R) = \left[ 1 + \left( \frac{T_2}{T_1} \right)^2 \frac{Norm_2}{Norm_1} \right]^{-1}. \quad (5.2)$$

We have calculated this formula for each shell in  $0.6 - 1.0'$ ,  $1.0 - 2.0'$ ,  $2.0 - 4.0'$ , and  $4.0 - 8.0'$  using the best-fit values in table 5.10 to plot  $f(R)$  against the 3-dimensional radius  $R$  in figure 5.11 (a). This plot clearly indicates that the cool component is dominant at the central region, while it

occupies only  $\lesssim 1\%$  at  $R > 4'$ . We have fitted these four points with a 3-dimensional  $\beta$ -model function,  $f(R) = [1 + (R/R_{c,f})^2]^{-3\beta_f/2}$ , and obtained  $R_{c,f} = 0.43'_{-0.16}^{+0.19}$  and  $\beta_f = 0.60_{-0.13}^{+0.19}$ .

Considering the projection effect, we can calculate the volume occupied by the cool gas at each 2-dimensional ring of  $\theta_{\text{in}}-\theta_{\text{out}}$  in unit of radian, as

$$V_1 = f \frac{4}{3} \pi D_A^3 (\theta_{\text{out}}^3 - \theta_{\text{in}}^3) (1 - \theta_r^2)^{3/2} / (1 - \theta_r^3), \quad (5.3)$$

where  $\theta_r \equiv \theta_{\text{in}}/\theta_{\text{out}}$ , and  $D_A = 61$  Mpc is the angular diameter distance to HCG 62. Because the vMekal normalization is defined as  $Norm = \int n_e n_H dV / (4\pi(1+z)^2 D_A^2)$ , the electron density of the cool gas,  $n_{e1}$ , is computed as

$$n_{e1} = \sqrt{1.2 \times 4\pi (1+z)^2 D_A^2 / V_1}, \quad (5.4)$$

assuming  $n_e = 1.2 n_H$  for a fully ionized gas with hydrogen and helium mass fraction of  $X = 0.7$  and  $Y = 0.28$ . The electron density of the hot gas,  $n_{e2}$ , is similarly derived by replacing  $f$  into  $(1-f)$ . The ion density including helium is  $n_i = 0.92 n_e$ , therefore the gas pressure is calculated as

$$P_{\text{gas}} = 1.92 n_{e1} kT_1 = 1.92 n_{e2} kT_2. \quad (5.5)$$

The derived gas pressure  $P_{\text{gas}}$ , cool or hot gas temperature  $kT_1$  or  $kT_2$ , and cool or hot electron density  $n_{e1}$  or  $n_{e2}$  are plotted in figures 5.11 (b)–(d). The 2- $T$  fit results are adopted for points in the range of 0.6–4' and the 1- $T$  fit results for others. The systematic errors when the background level is increased or decreased by  $\pm 5\%$  are considered in the error bars for the outermost two points. It is supposed that blue points belongs to the cool component and red points to the hot one.

We must be careful in dealing with these plots because data points are not independent with each other. We first fitted the gas pressure plot by combining both the cool and hot data points, with a 3-dimensional double  $\beta$ -model,  $P_{\text{gas}} = P_1 [1 + (R/R_{c,P_1})^2]^{-3\beta_{P_1}/2} + P_2 [1 + (R/R_{c,P_2})^2]^{-3\beta_{P_2}/2}$ . Due to the small number of data points, we have fixed  $R_{c,P_1} = 0.1'$  and  $\beta_{P_1} = 0.65$  using the best-fit values in table 5.3 obtained with the radial surface brightness profile fit. The fitted parameters are  $P_1 = 58 \pm 130$  eV cm $^{-3}$ ,  $P_2 = 18 \pm 32$  eV cm $^{-3}$ ,  $R_{c,P_2} = 0.60 \pm 1.44'$ , and  $\beta_{P_2} = 0.38 \pm 0.23$ . The best-fit model is indicated by a dashed line in figure 5.11 (c). The green curves represent each component of the double  $\beta$ -model.

We then fitted the cool gas temperature with a power-law model,  $kT_1(R) = a R^b$ , and the hot gas electron density with a 3-dimensional  $\beta$ -model and a constant,  $n_{e2}(R) = n_{e2,0} [1 + (R/R_{c,n_{e2}})^2]^{-3\beta_{n_{e2}}/2} + C_{n_{e2}}$ . The best-fit values are  $a = 0.80 \pm 0.17$  keV,  $b = 0.09 \pm 0.20$ ,  $n_{e2,0} = 0.007 \pm 0.020$  cm $^{-3}$ ,  $R_{c,n_{e2}} = 1.4 \pm 7.2'$ ,  $\beta_{n_{e2}} = 1.2 \pm 5.8$ , and  $C_{n_{e2}} = (0.49 \pm 0.48) \times 10^{-3}$  cm $^{-3}$ . The best-fit models for  $kT_1$  and  $n_{e2}$  are drawn by dashed lines. The model functions for  $kT_2$  and  $n_{e1}$  are derived using the relation  $kT_2 = P_{\text{gas}}/n_{e2}$  and  $n_{e1} = P_{\text{gas}}/(kT_2)$ , which are indicated by another dashed line in each panel. Although errors of these parameters are quite large, these functions can reproduce the observed properties of the cool and hot gases fairly well.

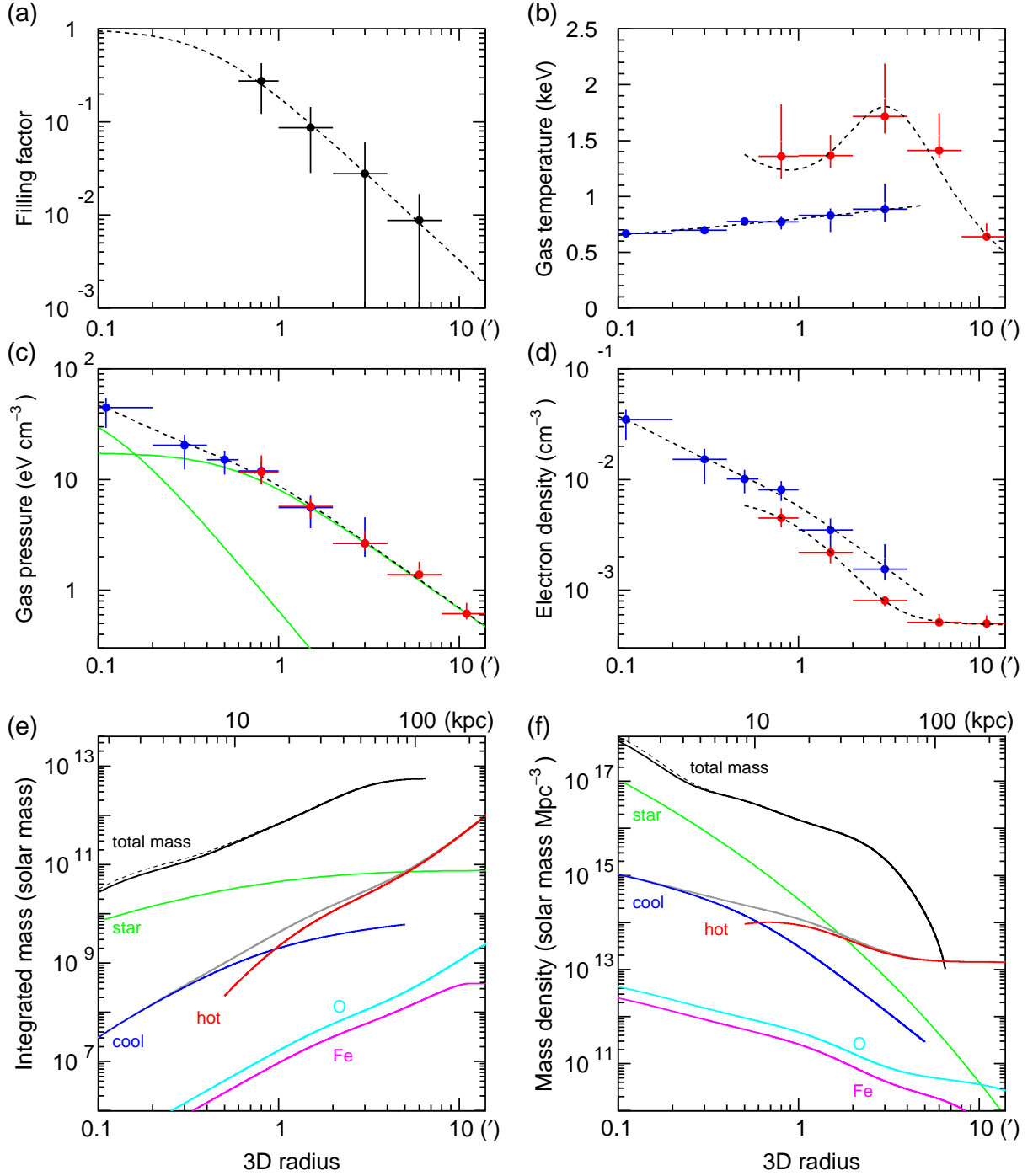


Fig. 5.11: (a) Volume filling factor  $f(R)$  of the cool component, (b) cool or hot gas temperature  $kT_1$  or  $kT_2$ , and (c) gas pressure  $P_{\text{gas}}$ , (d) cool or hot electron density  $n_{e1}$  or  $n_{e2}$ , plotted against the 3-dimensional radius  $R$ . Blue points represent the cool component and red points the hot. In panels (b)–(d), 2- $T$  fit results are adopted in the range of 0.6–4' and 1- $T$  fit results for others. The systematic errors when the background level is increased or decreased by  $\pm 5\%$  are considered in the error bars for the outermost two points. The dashed lines in panels (a)–(d) and green curves in panel (b) represent the best fit models. See text in details. (e) A black line indicates the total integrated gravitational mass,  $M_{<R}$ , estimated from the best fit models. The solid line is calculated by eq. (5.7), and dashed line is by eq. (5.9). Red and blue lines represent the gas mass of the hot and cool components, respectively. The O and Fe mass contained in either of the gas is plotted by cyan and pink lines. The stellar mass estimated from the  $R$  band photometry of the HCG 62a galaxy by Tran et al. (2001) Tran et al. 2001 is indicated by a green line. See text for details. (f) Same as (e), but for the differential mass density profiles.

### 5.6.2 Dark matter and gas mass

The gas mass density  $\rho_{\text{gas}}$  is expressed as

$$\rho_{\text{gas}} = 1.92 \mu m_{\text{p}} [f n_{\text{e}1} + (1 - f) n_{\text{e}2}], \quad (5.6)$$

where  $\mu = 0.62$  is the mean molecular weight, and  $m_{\text{p}}$  is the proton mass. Assuming the hydrostatic equilibrium, the total integrated gravitational mass,  $M_{<R}$ , within the 3-dimensional radius of  $R$  is given by

$$M_{<R} = -\frac{R^2}{\rho_{\text{gas}} G} \frac{dP_{\text{gas}}}{dR}, \quad (5.7)$$

in which  $G$  is the gravitational constant. The differential mass density,  $M(R)$ , is given by

$$M(R) = \frac{1}{4\pi R^2} \frac{dM_{<R}}{dR}. \quad (5.8)$$

Figures 5.11 (e) and (f) show the integrated and differential mass profiles (black lines) as a function of the 3-dimensional radius in unit of arcmin or kpc. We also overlaid the gas mass (gray) for the hot (red) and cool (blue) components in the same panels, by integrating the gas density,  $\rho_{\text{gas}}$ .

However, in the two-phase model under the pressure balance, the hot gas is lighter in mass density than the cool gas, and becomes buoyant. The hot gas would escape from the group core if it is not enclosed by other mechanisms (see § 5.8 in detail). In such a case, hydrostatic equilibrium may have been broken, hence we have also calculated the integrated gravitational mass by treating the hot and cool components separately. Namely,

$$\begin{aligned} M_{1,<R} &= -\frac{R^2}{\rho_1 G} \frac{dP_{\text{gas}}}{dR}, & \rho_1 &= 1.92 \mu m_{\text{p}} n_{\text{e}1}, \\ M_{2,<R} &= -\frac{R^2}{\rho_2 G} \frac{dP_{\text{gas}}}{dR}, & \rho_2 &= 1.92 \mu m_{\text{p}} n_{\text{e}2}, \\ M_{<R} &= f M_{1,<R} + (1 - f) M_{2,<R}. \end{aligned} \quad (5.9)$$

The gravitational mass indicated by dashed lines in figures 5.11 (e) and (f) are calculated using eq. (5.9). There are only small differences between the two at the group center; the latter is larger by about 15% at  $R = 0.1'$  (1.8 kpc).

We have encountered one severe problem in these plots. The integrated total mass saturates at  $R \sim 6'$  (100 kpc), and the differential mass becomes even smaller than the gas mass. This is physically unrealistic, suggesting that some presumption(s) we have supposed might not be realized around this radius. The direct source of the problem is caused by the fact that the hot gas temperature,  $kT_2$ , drops very steeply from  $\sim 1.5$  keV to 0.64 keV in this radial range. Therefore, the electron density,  $n_{\text{e}}$ , almost saturates, while the gas pressure,  $P_{\text{gas}}$ , decreases monotonously. This might in part be affected by the smaller field of view in our observations than the extended group emission. We cannot deproject the outermost shell in 8–14', so that X-ray flux in this shell is slightly overestimated. Nevertheless, the major origin of the problem

is due to the steep temperature drop. It should be examined more precisely by the Suzaku satellite, which has lower and more stable background than XMM-Newton, and much superior low-energy sensitivity than ASCA.

Another possibility, which is astrophysically more interesting, is that the hydrostatic equilibrium is not reached there. The flattening of the electron density suggests an outflow of the hot gas. The steep temperature drop can be reversely recognized as the temperature rise in the boundary region between the cool and hot gas. This suggests a shock heating of accreting ICM, and/or remnants of past lifted cavities (see § 5.8). The apparent inconsistency in the total mass may therefore indicate traces of the dynamical evolution.

Aside from the above problem, the derived gravitational mass is about  $M_{<R} = 5 \times 10^{12} M_{\odot}$  within 100 kpc, close to the value given by Pildis et al. (1995) Pildis et al. 1995,  $M_{\text{tot}} = 2.9 \times 10^{13} M_{\odot}$  within  $r < 15'$  (270 kpc) with the ROSAT PSPC observation assuming a single-phase gas model. We also plot the O (cyan) and Fe (pink) mass contained in the whole gas. The simple linear fit plotted in figure 5.10 is adopted to calculate the O and Fe mass. The derived gas and Fe masses of  $M_{\text{gas}<R} = 1.6 \times 10^{12} M_{\odot}$  and  $M_{\text{Fe}<R} = 4 \times 10^8 M_{\odot}$  within  $r < 300$  kpc are consistent with the result from ASCA and ROSAT by Finoguenov and Ponman et al. (1999) Finoguenov & Ponman 1999 of  $M_{\text{gas}<R} = (1.7 \pm 0.1) \times 10^{12} M_{\odot}$  and  $M_{\text{Fe}<R} = (3.8 \pm 2.0) \times 10^8 M_{\odot}$ . However, our values are based on the extrapolation out to the XMM-Newton field of view, so that they have larger errors by a factor of  $\sim 2$ .

### 5.6.3 Stellar mass

The stellar mass in figures 5.11 (e) and (f) indicated by green lines is estimated from the  $R$  band photometry of the HCG 62a galaxy by Tran et al. (2001) Tran et al. 2001, assuming the spherical symmetry and the surface brightness profile obeying the de Vaucouleurs  $r^{1/4}$  law,

$$\Sigma(r) \propto 10^{-3.33071 [(r/r_{\text{eff}})^{1/4} - 1]}, \quad (5.10)$$

where  $r_{\text{eff}} = 32''$  is the effective radius, or the half light radius. Because the  $r^{1/4}$  law is for the surface brightness, deprojection for the 3-dimensional radius must be performed. We utilized a numerical table computed by Young et al. (1976) Young 1976. The mass-to-light ratio,  $M_{\text{star}}/L_B = 8 (M_{\odot}/L_{B,\odot})$ , is assumed, and we use  $B - R = 2.0$  mag by Hickson et al. (1989) Hickson et al. 1989, and  $A_B = 0.224$  and  $A_R = 0.139$  after NASA/IPAC Extragalactic Database (NED) to calculate the  $B$  band absolute magnitude,  $L_B = L_R + (B - R) - A_B + A_R = -19.46$  mag. Using the value  $L_{B,\odot} = 5.48$  mag, the stellar mass of the HCG 62a galaxy is calculated as  $M_{\text{star}} = 7.6 \times 10^{10} M_{\odot}$ .

The  $B$  magnitude within the effective diameter of  $59.90''$  isophotes (table 5.1) is also given by Hickson et al. (1989) Hickson et al. 1989, however, we found that  $M_{\text{star}}$  calculated from this value was by about a factor of four larger than the value calculated above, if we assume that  $r_{\text{eff}}$  is the same for both bands. Then, the stellar mass would significantly exceed the total gravitational mass at the central region. We therefore have adopted the stellar mass based on

the  $R$  band photometry. Tran et al. (2001) also report that there is 19% of disk component which can be fitted by  $\Sigma(r) \propto \exp(-r/r_d)$  for HCG 62a. This gives asymmetric image residual flux  $R_A = 19\%$ , and the total residual fraction of light  $R_T = 18\%$ . Therefore, uncertainty on the stellar mass estimation is at least  $\sim 20\%$ .

We notice several features in the mass profiles. The gas mass of the cool component is taken over by the hot component at  $\sim 1'$  (18 kpc). The stellar mass is overcome by the gas mass at  $\sim 2.5'$  (45 kpc), indicating that the cool component is very concentrated in the group center. The region of high metal abundance almost coincides with the volume dominated by the stellar mass, which supports the natural view that stars are responsible for the production of excess iron and silicon around the group center.

## 5.7 ICM properties

The temperature structure in HCG 62 can be characterized by a mixture of hot ( $\sim 1.4$  keV) and cool ( $\sim 0.7$  keV) components. As shown in figure 5.11, the cool component is dominant within  $r < 0.8'$  and then a cool and hot mixture appears in  $r = 0.8-4'$ . The hot component is dominant in the outer region. The two-phase nature seems to be preferred than the single-phase structure such as that seen in M 87 Matsushita et al. 2002. However, this apparent two-phase does not necessarily mean that the cool and hot gas co-exist at the intermediate region, instead it probably represents that they are patchy and/or have irregular shapes. As seen in figure 5.6, the cool region is elongated from northeast to southwest, roughly corresponding to the direction of the two cavities. In this sense, HCG 62 group is different from NGC 1399, NGC 5044 and RGH 80 galaxy groups Buote 2002; Buote et al. 2003a; Xue et al. 2004, in which strong evidence for a multi-phase gas is suggested at the central region. On the other hand,  $T_{\text{cool}}$  is similar to these groups, and  $T_{\text{cool}} \simeq T_{\text{hot}}/2$  is recognized among them. It is claimed that the temperatures of the cool component seen in these three groups are close to the kinetic temperature of the stars, although the stellar velocity dispersion is not known for the HCG 62a galaxy.

Mass density of the cool component exceeds the hot-component density within about 10 kpc, in which the stellar mass density is orders of magnitude higher. This again implies that the cool component is probably connected with the stars concentrated around the central galaxy HCG 62a. We also note that the cool component mass density is always smaller than the stellar mass density. On the other hand, the hot component exceeds the stellar mass density around  $r \sim 2'$  (30 kpc), indicating that the gravitational potential of the galaxy group is traced by the hot component. Its temperature (1.4 keV) is also typical for groups of galaxies.

In the outer region ( $r > 8'$ ), the temperature of the hot component drops fairly sharply. The radius corresponds to about  $0.15 r_{\text{vir}}$ , with  $r_{\text{vir}} \approx 1.1 (T/1.5 \text{ keV})^{1/2}$  Mpc. This causes a peak in the temperature profile at  $r \approx 5'$  (90 kpc). Similar temperature profiles have been observed in other galaxy groups such as RGH 80, NGC 2563, and NGC 5044 (Xue et al. 2004, Mushotzky et al. 2003, Buote et al. 2003a). The drop of temperature suggests either that the dark matter

is confined within this small radius or that the gas is yet to be heated in this region. In either case, there is a certain boundary of the group around  $0.2r_{\text{vir}}$ , and it is suggested that these groups are young and forming systems.

The heavy elements are enriched by SN Ia and SN II Tsujimoto et al. 1995. The former process dominantly yields Fe group Iwamoto et al. 1999, and the latter produces lighter elements like O, Ne and Mg Thielemann et al. 1996; Nomoto et al. 2006. Both supernova contribute to Si and S. Since O is produced mainly by SN II, the flatter O abundance profile compared with those of Si and Fe implies enhanced contribution of SN Ia in the central region and/or that the shallow potential of HCG 62 is unable to confine SN II products which should have been supplied to the intracluster space in the form of galactic winds. The products of SN Ia, on the other hand, are considered to be brought in to ICM by gas stripping.

The ratio, Mg/O, is  $3.3 \pm 2.2$  times solar within  $1'$  (18 kpc) based on the  $2-T$  fit. Though the error is large, this value is similar or somewhat larger than those in other groups:  $2.5 \pm 0.4$  solar for NGC 5044 Xu et al. 2002,  $1.3 \pm 0.2$  for NGC 4636 Tamura et al. 2003, both measured with RGS, and  $\sim 2$  solar in RGH 80 Xue et al. 2004. In M 87, this ratio is  $1.3 \pm 0.1$  solar within 20 kpc Matsushita et al. 2003. Since both O and Mg are mainly produced by SN II, the marginally high Mg/O value may reflect the difference in the stellar initial mass function (IMF). Theoretical calculations Nomoto et al. 2006; Thielemann et al. 1996 predict that a lighter-mass progenitor of SN II synthesizes enhanced Mg compared with O, therefore HCG 62 might have had the stellar IMF with smaller number of massive stars ( $M \gtrsim 20M_{\odot}$ ) than our galaxy and other groups above. However, the dependence of the Mg/O ratio on the progenitor mass is typically  $\sim 20\%$  at most, so that we have to think about other possibilities for the Mg/O ratio greater than  $\sim 1.2$ .

If excess Fe in the center is caused by SN Ia activity of HCG 62a, it should be more extended at least than the extent of the central cool component which is the gas directly bound by the central galaxy. The possible enhancement of the Ni/Fe ratio at  $r < 2'$  as seen in § 5.5.1 supports this scenario. For example, the CDD2 model in Iwamoto et al. (1999) Iwamoto et al. 1999 predicts the Ni/Fe ratio of 1.8 solar. The region of high metal abundance almost covers the volume dominated by the stellar mass, which supports the natural view that stars are responsible for the production of excess Fe and Si around the group center. It seems to range even to the 3D radius of  $\sim 6'$  (100 kpc) in figure 5.10, where the hot gas mass exceeds the stellar mass as seen in figure 5.11 (f). This suggests either that the Fe production has occurred in a wider region than the present location of the galaxy or that there have been an outflow of Fe. The presence of cavities in HCG 62 suggests that part of the central metal-rich gas may have been lifted from the galaxy.

The observed abundance gradients indicate that there have been no strong mixing occurred in the core region. We also note that there is no significant change of temperature or abundance across the cavity regions. These features imply that the process of cavity creation causes mild, subsonic gas motion occurring in a fairly limited volume. This implication is consistent with the

result by Brüggén and Kaiser (2002) who showed that mixing by buoyant bubbles gave relatively weak impact on the metallicity gradients based on numerical simulations.

## 5.8 Supporting mechanisms of X-ray cavities

B04 have systematically studied 16 clusters, 1 group (HCG 62), and 1 galaxy (M84), in which prominent X-ray surface brightness depressions (cavities or bubbles) are observed. They find that a mechanical (kinetic) luminosity seems to correlate with the 1.4 GHz synchrotron luminosity. However, its ratio ranges widely between a few and several thousand, and they have concluded that the radio luminosity is an unreliable gauge of the mechanical power of the AGN jets. Dunn & Fabian(2004) Dunn & Fabian 2004 and D05 have studied 21 clusters, 3 galaxies, in which HCG 62 is not included, and find that the ratio of an energy factor,  $\mathcal{K}$ , to a volume filling factor,  $\mathcal{F}$ , shows a large scatter,  $1 \lesssim \mathcal{K}/\mathcal{F} \lesssim 1000$ , for active cavities associated with radio lobes, and that it becomes even larger for ghost cavities. The factor,  $\mathcal{K}$ , accounts for the additional energy from relativistic particles accompanying the electrons (e.g., protons). The parameter of  $\mathcal{F}$  represents the volume filling factor of the relativistic particles, and is supposed not to vary far from unity. Typical value of  $\mathcal{K}$  in literature is  $\mathcal{K} = 100$ , according to the measurements of cosmic-rays around the solar system. However, there is no direct evidence indicating that such a high energy density is really carried by protons. The reason why  $\mathcal{K}/\mathcal{F}$  varies so largely from cluster to cluster is a mystery, which might imply that there are several ways in supporting mechanism and/or formation of the X-ray cavities.

In this section, we examine whether this non-thermal pressure support scenario is realistic or not for HCG 62. In §5.8.1, we summarize our X-ray results, as well as optical and radio observations. In §5.8.2–5.8.4, standard indices of cavities are calculated for HCG 62, and difficulties in the non-thermal support scenario is considered in §5.8.5. In §5.8.6 and §5.8.7, other possibilities of the supporting mechanism and formation of cavities are investigated.

### 5.8.1 Characteristics in X-ray, optical, and radio

We have confirmed the X-ray cavities reported by Vrtilek Vrtilek 2001, Vrtilek et al. 2002 in the northeast and southwest regions of HCG 62 in the Chandra image as shown in figures 5.3 (a) and 5.5. As described in §5.4.2, absorption is unlikely to be the origin of cavities. There are no significant spectral differences between cavity and non-cavity regions, nor any traces of the shock-heated gas around the cavities, as seen in the temperature map (figure 5.6). According to our hollow sphere model analysis (§5.4.3), both the cavities should be aligned side by side with the group core to a fairly good degree, namely, the projected distances to the group core are close to their real ones. It is also suggested that the shape of cavities is probably elongated in the direction of our line of sight, and that the side of the cavities which is farther from the core should be larger in size and/or weaker in the X-ray emissivity.

With regard to the central HCG 62a galaxy, we found no evidence for the AGN activity in the X-ray data. The best-fit spectrum of HCG 62a is a thermal emission rather than a power-law one. No point sources were recognized at the center of HCG 62a in both soft and hard bands. The upper limit of the AGN emission can be placed around  $L_X \lesssim 10^{39}$  erg s<sup>-1</sup> (0.5–4 keV). We also found that the location of HCG 62a was slightly shifted from the group core by about 5'' (1.5 kpc) on the projected sky image (table 5.4). This positional shift may imply the effect of gas stripping and/or the dynamical motion of the galaxy.

The ASCA has detected a spatially extended ( $\sim 10'$ ) excess hard X-ray emission above  $\sim 4$  keV in the HCG 62 group Fukazawa et al. 2001, which is supposed to be due to the relativistic electrons with Lorentz factor  $\gamma \sim 10^3$ – $10^4$  and/or sub-relativistic particles. This may also have some relation to the X-ray cavity, however, we could not confirm nor reject this result due to the higher non X-ray background of Chandra and XMM-Newton than ASCA.

In the optical band, Coziol et al. (2004) Coziol et al. 1998 and Shimada et al. (2000) Shimada et al. 2000b have detected weak [NII] and [OI] emission lines in the spectrum of HCG 62a, and classified it as a low luminosity AGN (LLAGN). On the other hand, Coziol et al. (2004) Coziol et al. 2004 have assigned the lowest activity index of  $-5$  (quiescent, intermediate and old stellar populations) to HCG 62a, according to the equivalent width measurement of the H $\alpha$  absorption lines. They have also distinguished HCG 62 group among 27 compact groups of galaxies as type C, which comprises groups with high velocity dispersions and are dominated by elliptical galaxies with no activity, presumably corresponding to the later stage of the evolution.

In the radio band, as shown in figure 5.3 (a), weak radio emission at 1.4 GHz is detected around HCG 62a, however its luminosity is as small as  $L_{\text{radio}} = 1.8 \times 10^{38}$  erg s<sup>-1</sup> (10 MHz–5 GHz), smallest in table 1 of B04. The radio emission does not show a clear association with the cavities, though the angular resolution of 45'' FWHM is not sufficient to see detailed structures.

### 5.8.2 Gas pressure & non-thermal pressure

We take the distances to both cavities from the group core to be  $R_{\text{cav}} = 25''$  (7.4 kpc) and their radii to be  $r_{\text{cav}} = 13.5''$  (4.0 kpc) for simplicity. This approximation can be justified by the similarity between north and south cavities measured from the group core (table 5.5) with the center position determined from the center of the wider component in 2-dimensional 2- $\beta$  fit (table 5.4). Assuming those parameters, the ICM gas pressure at  $R_{\text{cav}}$  is calculated to be  $P_{\text{gas}} = 17$  eV cm<sup>-3</sup>, from eq. (5.5).

The non-thermal pressure of relativistic particles can be estimated from the radio intensity. Here, we assume that half of the radio flux comes from a single cavity, namely,  $L_{\text{radio}} = 9 \times 10^{37}$  erg s<sup>-1</sup> (10 MHz–5 GHz) according to B04. Assuming that the radio emission is due to synchrotron radiation by relativistic electrons, the total non-thermal pressure can be calculated as  $P_{\text{tot}} = \mathcal{K}P_e + \mathcal{F}P_B$ , where  $P_e$  is a pressure of the relativistic electrons, and  $P_B$  is a pressure of the magnetic field, following the convention adopted by D05.

The relativistic electron pressure is calculated to be  $P_e = C_e L_{\text{radio}} B^{-3/2} / V$  (e.g., Govoni & Fertti (2005) Govoni 2005), where  $B$  is a magnetic flux density,  $V \equiv \frac{4}{3} \pi r_{\text{cav}}^3$  is the volume of the cavity, and  $C_e$  is a constant depending on the spectral index  $\alpha$  of the radio emission, as  $C_e = \sqrt{27 m_e^5 c^9 / (2 \pi e^7)} (\nu_1^{-1/2} - \nu_2^{-1/2}) / (\log \nu_2 - \log \nu_1) = 1.4 \times 10^8$  [cgs] for  $\alpha = 1$ ,  $\nu_1 = 10$  MHz, and  $\nu_2 = 5$  GHz. Therefore,

$$\mathcal{K} P_e = 3.3 \times \left( \frac{\mathcal{K}}{100} \right) \left( \frac{L_{\text{radio}}}{9 \times 10^{37} \text{ cgs}} \right) \left( \frac{r_{\text{cav}}}{4 \text{ kpc}} \right)^{-3} \left( \frac{B}{10 \mu\text{G}} \right)^{-\frac{3}{2}} \text{ eV cm}^{-3}.$$

On the other hand, the magnetic pressure is

$$\mathcal{F} P_B = \mathcal{F} \frac{B^2}{8\pi} = 2.5 \left( \frac{\mathcal{F}}{1} \right) \left( \frac{B}{10 \mu\text{G}} \right)^2 \text{ eV cm}^{-3}.$$

Therefore, the total non-thermal pressure,  $P_T \equiv \mathcal{K} P_e + \mathcal{F} P_B$ , takes the minimum at a certain value of  $B = B_{\text{eq}}$ , the so-called equipartition condition, which is calculated as

$$B_{\text{eq}} = 11 \left( \frac{\mathcal{K}/\mathcal{F}}{100} \right)^{\frac{2}{7}} \left( \frac{L_{\text{radio}}}{9 \times 10^{37} \text{ cgs}} \right)^{\frac{2}{7}} \left( \frac{r_{\text{cav}}}{4 \text{ kpc}} \right)^{-\frac{6}{7}} \mu\text{G},$$

$$P_{T,\text{eq}} = \frac{7}{4} P_{e,\text{eq}} = \frac{7}{3} P_{B,\text{eq}} = 5.8 \times \left( \frac{\mathcal{K}/\mathcal{F}}{100} \right)^{\frac{4}{7}} \left( \frac{L_{\text{radio}}}{9 \times 10^{37} \text{ cgs}} \right)^{\frac{4}{7}} \left( \frac{r_{\text{cav}}}{4 \text{ kpc}} \right)^{-\frac{12}{7}} \text{ eV cm}^{-3}.$$

Thus the derived pressure at the equipartition condition is less than half of the ICM gas pressure, while the required equipartition magnetic flux density is typical for radio lobes of radio-loud AGNs Kataoka & Stawarz 2005. They have also found that the equipartition condition is achieved at least for the radio lobes of 40 radio galaxies. The discrepancy between  $P_{T,\text{eq}}$  and  $P_{\text{gas}}$  may be explained by the underestimation of  $\mathcal{K}/\mathcal{F} \sim 100$  or  $L_{\text{radio}} \sim 9 \times 10^{37}$  erg s<sup>-1</sup>, or by non-equilibrium situation. To make a balance between them,  $\mathcal{K}/\mathcal{F} = 690$  is needed. This value is consistent with those obtained by D05 for active bubbles in other clusters. It is also plausible that the radio intensity is getting dimmer in time due to the synchrotron cooling of relativistic electrons. We also note that the  $L_{\text{radio}}$  value used for the calculation is probably overestimated, because the observed radio intensity is likely to include emission from the core regions. Radio observation with higher angular resolution is desired.

### 5.8.3 Time scales

For discussion of cooling and non-equilibrium effects, comparison of several time scales is important. First of all, synchrotron electron ( $\gamma_e \gtrsim 10^4$ ) must be long-lived since the cavity is not fueled now from the central AGN. The synchrotron cooling time is calculated as

$$t_{\text{sync}} = \frac{9 m_e^3 c^5}{4 e^4 B^2 \gamma_e} = 25 \left( \frac{B}{10 \mu\text{G}} \right)^{-2} \left( \frac{\gamma_e}{10^4} \right)^{-1} \text{ Myr}.$$

Since rims of the cavities have not been shock heated, the cavities are supposed to have expanded at a velocity less than the sound speed,  $v_s = \sqrt{\gamma k T / (\mu m_p)} = 425 \text{ km s}^{-1}$ , where we have taken

$kT = 0.7$  keV,  $\gamma = 5/3$  and  $\mu = 0.62$ . Therefore, age of the cavities must be longer than the expansion time of

$$t_s = \frac{r_{\text{cav}}}{v_s} = 9.2 \left( \frac{r_{\text{cav}}}{4 \text{ kpc}} \right) \text{ Myr},$$

which is shorter than  $t_{\text{sync}}$ . If we assume  $\mathcal{K}/\mathcal{F} = 690$ ,  $t_{\text{sync}}$  can be shortened by a factor of  $(\mathcal{K}/\mathcal{F}/100)^{-4/7} = 0.33$ , and becomes comparable to  $t_s$ . The time scale for the cavities to collapse when internal pressure has disappeared is also considered to be about  $t_s$ . Such hollow cavities are buoyant and rise up outwards, even when pressure balance between inside and outside of the cavities is conserved. Coziol et al. (1998) Churazov et al. 2001 have given the terminal velocity as  $v_t = \sqrt{2gV/SC}$ , where  $S \equiv \pi r_{\text{cav}}^2$  is the cross section of the bubble,  $g \equiv GM_{<R_{\text{cav}}}/R_{\text{cav}}^2$  is the gravity at the bubble, and  $C = 0.75$  is the drag coefficient. The travel time of the cavities to the current position is estimated to be

$$t_{\text{buoy}} = R_{\text{cav}}/v_t = 15 \times \left( \frac{R_{\text{cav}}}{7.4 \text{ kpc}} \right)^2 \left( \frac{r_{\text{cav}}}{4 \text{ kpc}} \right)^{-1/2} \left( \frac{M_{<R_{\text{cav}}}}{2 \times 10^{11} M_{\odot}} \right)^{-1/2} \text{ Myr},$$

which is comparable to or somewhat longer than  $t_{\text{sync}} = 8$  Myr with  $\mathcal{K}/\mathcal{F} = 690$ . The refill time of the cavity is also given by McNamara et al. (2000) McNamara et al. 2000 as,

$$t_{\text{refill}} = 2R_{\text{cav}} \sqrt{r_{\text{cav}}/(GM_{<R_{\text{cav}}})} = 31 \times \left( \frac{R_{\text{cav}}}{7.4 \text{ kpc}} \right) \left( \frac{r_{\text{cav}}}{4 \text{ kpc}} \right)^{1/2} \left( \frac{M_{<R_{\text{cav}}}}{2 \times 10^{11} M_{\odot}} \right)^{-1/2} \text{ Myr}.$$

These considerations indicate that the cavity age of  $t_s$  or  $t_{\text{buoy}} \sim 10$  Myr is much shorter than the group age of  $\sim$  Gyr. Our time scales are consistent with B04, but in which they use  $R_{\text{cav}}$  instead of  $r_{\text{cav}}$ .

#### 5.8.4 Energetics

On the assumption that past AGN activity has produced the two cavities in about  $(t_{\text{buoy}}/2)$ , we can estimate the required mechanical (kinetic) power of the AGN jets. A work to generate two cavities,  $W_{\text{mech}} \equiv 2P_{\text{gas}}V$ , divided by  $(t_{\text{buoy}}/2)$  is called the mechanical luminosity (B04), and calculated to be

$$L_{\text{mech}} = 4P_{\text{gas}}V/t_{\text{buoy}} = 1.8 \times 10^{42} \times \left( \frac{R_{\text{cav}}}{7.4 \text{ kpc}} \right)^{-2} \left( \frac{r_{\text{cav}}}{4 \text{ kpc}} \right)^{7/2} \left( \frac{M_{<R_{\text{cav}}}}{2 \times 10^{11} M_{\odot}} \right)^{1/2} \text{ erg s}^{-1}.$$

It is supposed that this level of the AGN activity must continue for about  $-t_{\text{buoy}} < t < -0.5 t_{\text{buoy}}$ , and that it became inactive since  $-0.5 t_{\text{buoy}} < t$ . This value is comparable to the X-ray emission typically observed for LLAGN, although our upper limit on the X-ray luminosity is much lower,  $L_X \lesssim 10^{39} \text{ erg s}^{-1}$  (0.5–4 keV). The observed radio emission around HCG 62a,  $L_{\text{radio}} = 1.8 \times 10^{38} \text{ erg cm}^{-1}$ , is also much lower than  $L_{\text{mech}}$ , as pointed out by B04.

Because there are no evidence for the strong AGN activity at present time, the central AGN, if exists, should have made a final outburst of total energy  $\sim 10^{57}$  erg within  $\sim 20$  Myr ago. Clearly, a single supernovae cannot account for this size of energy. Such an absence of strong X-ray or radio emission at the core is also noticed in NGC 4636 ( $L_{\text{radio}} = 1.4 \times 10^{38}$  erg s $^{-1}$ ;  $L_X < 2.7 \times 10^{38}$  erg s $^{-1}$ ; Ohto et al. 2003; O’Sullivan et al. 2005), which shows a disturbed X-ray halo containing cavities associated with small-size jets. This might suggest that the AGN activity continues only for a short time scale, which is difficult to understand within the popular paradigm of AGN with a steady accretion disk. Formation of ghost cavities with an impulsively episodic activity of  $\ll 10^5$  yr is discussed by Wang & Hu (2005) Wang & Hu 2005. Considering captures of red giant stars by a super massive black hole ( $M_{\text{BH}} > 2 \times 10^8 M_{\odot}$ ), its feedback energy can amount to  $2.4 \times 10^{52}$  erg with a frequency of a few  $10^{-5}$  yr $^{-1}$ , which is too small to supply sufficient energy for the formation of cavities. It is probably true that HCG 62a also contains a massive black hole of  $M_{\text{BH}} \sim 10^8 M_{\odot}$ , because observations of the centers of nearby early-type galaxies show almost all have massive black hole Tremaine et al. 2002. However, we have to consider switching (on  $\rightarrow$  off) of the AGN activity.

### 5.8.5 Difficulties in non-thermal pressure support by jets

In §5.8.2–5.8.4, we have examined the properties of the cavities and the central AGN from the point of view that the non-thermal pressure of relativistic particles were provided through symmetrical jets of the past AGN activity. However there are several difficulties in this scenario.

As seen in §5.8.2,  $\mathcal{K}/\mathcal{F} = 690$  is needed to balance the ambient gas pressure with the internal non-thermal pressure at the equipartition condition. This value is in proportion to the inverse of  $L_{\text{radio}}$ , which is probably overestimated because significant fraction of  $L_{\text{radio}}$  should be attributed to the core region instead of the radio robes (figure 5.3 (a)). Then  $\mathcal{K}/\mathcal{F} = 690$  becomes still larger, which is probably unrealistic. One possibility is that the relativistic electrons are fading due to the synchrotron loss, which may be justified by the fact that  $t_{\text{sync}}$  under the equipartition magnetic field of  $B_{\text{eq}} = 17 \mu\text{G}$  ( $\mathcal{K}/\mathcal{F} = 690$ ) is comparable to the estimated cavity age of  $t_{\text{buoy}}$ . The relativistic electrons have much shorter synchrotron cooling time than that of protons, hence apparently large  $\mathcal{K}/\mathcal{F}$  might have been attained. In this case, the cavities are starting to collapse and losing the internal pressure support.

It is notable that both the two cavities observed in HCG 62 are pretty circular when projected in the sky (figure 5.3 (a)). The relative deviation image of figure 5.5 is remarkably smooth around the group core, and there are no obvious trails toward the cavities. This fact is quite difficult to understand considering the scenario that a pair of radio robes produced by symmetrical jets from the AGN has pushed away the IGM. In practice, clusters or galaxies hosting cavities usually show irregular or filamentary structures around the cluster core and cavities. The most prominent example is those of M 87 Churazov et al. 2001; Young et al. 2002, in which the “trails” of the rising two radio bubbles are clearly seen in the X-ray image. Furthermore, our hollow

sphere analysis suggests that the shape of cavities is probably elongated in the direction of our line of sight. It appears to be difficult for the symmetrical jets to make an elongation in such direction. We also note that shock heating is unlikely to be the origin of the cavities, because there is no significant evidence of heating at the edge of the cavities.

These considerations indicate that there might exist another supporting mechanism and/or formation scenario of the X-ray cavities, at least for HCG 62. In the following subsections, we consider these possibilities.

### 5.8.6 Another supporting mechanism — hot gas clump —

One possible supporting mechanism is a clump of hotter gas than the surrounding ICM ( $kT = 0.7$  keV). For example, if we assume that the temperatures in the cavities are higher than that of ICM by three times, namely  $T_{\text{hc}} = 3T$ , the required density,  $n_{\text{e,hc}}$ , is three times smaller. The emitted X-ray is roughly in proportion to  $n_{\text{e,hc}}^2 \sqrt{T_{\text{hc}}} = 0.2 n_{\text{e}}^2 \sqrt{T}$ , hence the observed X-ray intensity can be as low as 20%. Since we could have detected such hot emission if its flux were  $\sim 20\%$  of the  $F_{\text{sphere}}$  in table 5.5, we can derive the lower limit of the hot clump temperature, as  $T_{\text{hc}} \gtrsim 3T$ .

Schmidt et al. (2002) Schmidt et al. 2002 have done a similar discussion and ruled out volume-filling X-ray gas with temperature below 11 keV for a cavity in the Perseus cluster. With regard to the origin of the hot gas clump, it is suggested that the jets may intrinsically contain protons, or that they may have captured ambient thermal protons possibly shock-heated in the very initial phase of the cavity formation (D05). If we observe in higher energy band, such hot emission can be detected as a hard tail of the spectrum. The hard  $\Gamma = 1.5$  power-law component observed with ASCA Fukazawa et al. 2001 might originate from this kind of hot thermal emission, although the detected sky area of the power-law component is much more extended than the cavities.

If such a hot clump really exists, it undergoes a cooling by thermal conduction. Assuming  $kT_{\text{hc}} = 3 kT \simeq 2$  keV and  $n_{\text{e,hc}} = n_{\text{e}}/3 \simeq 10^{-3} \text{ cm}^{-3}$ , the thermal conductivity for a non-magnetized plasma is given by Spitzer (1962) Spitzer 1962 as,

$$\kappa_{\text{S}} = 10^{30} \left( \frac{kT_{\text{hc}}}{2 \text{ keV}} \right)^{\frac{5}{2}} \left( \frac{n_{\text{e,hc}}}{10^{-3} \text{ cm}^{-3}} \right)^{-1} \left( \frac{\ln \Lambda}{36} \right)^{-1} \text{ cm}^2 \text{ s}^{-1},$$

where  $\ln \Lambda$  is the Coulomb logarithm. Therefore, the cooling time of the cavities is roughly calculated to be

$$t_{\text{cond}} \simeq \frac{r_{\text{cav}}^2}{\kappa_{\text{S}}} = 0.5 \times \left( \frac{r_{\text{cav}}}{4 \text{ kpc}} \right)^2 \left( \frac{kT_{\text{hc}}}{2 \text{ keV}} \right)^{-\frac{5}{2}} \left( \frac{n_{\text{e,hc}}}{10^{-3} \text{ cm}^{-3}} \right) \text{ Myr},$$

which is much shorter than the estimated cavity life span of  $t_{\text{buoy}}$ .

It is claimed that the thermal conductivity may become 5–10 times smaller than the Spitzer value under the turbulent magnetic fields (e.g., Chandran & Maron(2004) Chandran & Maron

2004), although  $t_{\text{cond}}$  seems to be still smaller considering this effect. On the other hand, from the observational point of view, we do see this kind of temperature variations in clusters. The most prominent example is the “cold front”, first reported by Markevitch (2000) Markevitch et al. 2000 for A2142. Ettore & Fabian(2000) Ettore & Fabian 2000 have pointed out that it requires the classical Spitzer thermal conductivity to be reduced at least by a factor of 250–2500. Markevitch (2000) Markevitch et al. 2003 also find that  $\sim 40$  times reduction is needed for A754. For the magnetic field expected in the radio robe ( $B \sim 10 \mu\text{G}$ ), the electron and proton gyro radii are by 11–12 orders of magnitude smaller than their Coulomb mean free paths, therefore the effective conductivity strongly depends on the topology of the field. If the magnetic field encloses the hot clump like a cage, the hot clump may survive for more than  $\sim 20$  Myr.

### 5.8.7 Another formation scenario — galaxy motion —

As we found in §5.3.3 with the 2-dimensional  $2-\beta$  model fit, the location of HCG 62a (narrower component) is slightly offset from the group core (wider component) by about  $5''$  (1.5 kpc) on the projected sky image. This fact inevitably leads to the idea that the HCG 62a galaxy is moving around the group core. It is natural to consider that HCG 62a is performing a pseudo-Kepler motion, gradually decreasing its distance to the group core by a dragging force. From this point of view, the two cavities might be a piece of the trail of the HCG 62a orbit. Here, we assume that the orbital plane of HCG 62a is nearly in parallel to our line of sight, with a circular orbit. and that its orbital radius is close to the distance,  $R_{\text{cav}}$ , of the two cavities to the group core.

It is interesting that the two cavities are located almost at the same distance from the group core, whereas the south cavity is by 1.6 times closer to HCG 62a than the north cavity. As indicated by a cross in figure 5.3 (a), HCG 62a is shifted from the group core indicated by a plus mark (center of the wider component) roughly toward the direction of the south cavity. These two facts support the assumption above. The measured redshift of HCG 62a is consistent with that of the group (table 5.1). On this assumption, the rotation speed is calculated to be  $v_{\text{rot}} = \sqrt{GM_{<R_{\text{cav}}}/R_{\text{cav}}} = 340 \text{ km s}^{-1}$ , which is comparable to the sound speed,  $v_s = 425 \text{ km s}^{-1}$ . The period of rotation is

$$t_{\text{rot}} = \frac{2\pi R_{\text{cav}}}{v_{\text{rot}}} = 133 \left( \frac{R_{\text{cav}}}{7.4 \text{ kpc}} \right)^{\frac{3}{2}} \left( \frac{M_{<R_{\text{cav}}}}{2 \times 10^{11} M_{\odot}} \right)^{-\frac{1}{2}} \text{ Myr.}$$

Even though it is at least shorter than the group age, is much longer than other time scales, and the “tunnel” seems to be filled relatively quickly. In this scenario, the ICM gas would have experienced the encounter with the HCG 62a galaxy several times periodically. If some processes, e.g., freezing the plasma with magnetic field or the pressure support with hotter gas, have slowed the collapse of the cavities, this effect may be worthwhile consideration. In terms of the energetics, the kinetic energy of the galaxy motion amounts to  $\sim 10^{59}$  erg, therefore it can supply sufficient energy to produce the cavities by depositing 7% of the kinetic energy per orbit. Such a motion of the galaxy also would have played an important role on the mixing and the metal enrichment of the ICM, which has been discussed in the previous section.



## Chapter 6

# Summary and Conclusion

### 6.1 HCG 80

- With high-sensitivity Chandra observations, we searched for diffuse X-ray emission from the intragroup medium (IGM); however, no significant emission was detected. We place a severe upper limit on the luminosity of the diffuse gas as  $L_X < 6 \times 10^{40}$  erg s<sup>-1</sup>.
- On the other hand, significant emission from three of the four members were detected. In particular, we discovered huge halo emission from HCG 80a that extends on a scale of  $\sim 30$  kpc perpendicular to the galactic disk, whose X-ray temperature and luminosity were measured to be  $\sim 0.6$  keV and  $\sim 4 \times 10^{40}$  erg s<sup>-1</sup> in the 0.5–2 keV band, respectively. It is most likely to be an outflow powered by intense starburst activity.

### 6.2 HCG 62

- There are two cavities at about 30'' northeast and 20'' southwest of the central galaxy in the Chandra image. The size of spherical hollow cavities are constrained from the surface brightness structure to be 12''–17''. The agreement with the observed angular size suggests that the gas density in the cavity is very low, less than 1/3 and consistent with zero.
- The energy spectrum shows no significant change in the cavity compared with that in the surrounding region.
- We studied radial distributions of temperature and metal abundance with joint spectral fit for the Chandra and XMM-Newton data, and two temperatures: 0.7 keV and 1.4 keV were required in the inner  $r < 2'$  (35 kpc) region.
- The mass profiles were obtained for the gas and stars. The hot component is much more extended than the stars, and thought to trace the gravitational potential of the galaxy group.

- Abundance of O is  $\sim 0.3$  solar,  $\sim 3$  times less abundant than Fe and Si, and shows a flatter profile.
- Abundances of Fe and Si show concentration in the central region, and a high Ni/Fe ratio is suggested.

### 6.3 Hot Gas in Groups of Galaxies

By this analysis, I confirm that X-ray diffuse gas was extremely weak in spiral dominant group, on the other hand, elliptical dominant group was strong. It means that structure formation process and evolution for the both systems are fundamentally different. Based on the HCG 80 results, we discuss possible reasons for the absence of diffuse X-ray emission in the HCG 80 group, suggesting that the system is subject to galaxy interactions, and is possibly at an early stage of IGM evolution. Based on the HCG 62 results, I conclude that diffuse gas is mainly provide from elliptical galaxy by the starburst activity. For elliptical dominant group, we found that the cavity was also made by AGN activity or galaxy motion for central elliptical galaxy. Therefore, elliptical galaxies in the center of group play very important roles about mixing of ICM and the metal production and enrichment processes.

For metal distribution in the intragroup medium, observed metal distribution supports the view that iron and silicon are produced by type Ia supernova in the central galaxy, while galactic winds by type II supernova have caused wide distribution of oxygen. The shallow potential of HCG 62 is unable to confine the SN II products which should have been escaped in the form of galactic winds. The marginally higher Mg/O ratio of  $3.3 \pm 2.2$  implies steeper IMF. The results for concentration of Fe and Ni in the center are consistent with that they are synthesized by SN Ia in the central galaxy.

X-ray cavities for HCG 62 implies that the non-gravitational energy input in groups of galaxies. The supporting mechanism of the cavity is discussed, and pressure for the sum of electrons and magnetic field is too low to displace the hot group gas. The non-thermal energy density by high energy protons necessary to support the cavity implies  $\mathcal{K}/\mathcal{F} = 690$ , namely almost 700 times larger energy than that of electrons needs to be contained the cavity. This leaves the origin of the cavities a puzzle, and we discuss other possible origins of the cavities. We looked into alternative scenarios for the cavity creation. A clump of very hot gas and fast motion of the central galaxy were considered, but more observational evidences are necessary to perform a quantitative evaluation.

Moreover, for the outer region of group, the gravitational mass density drops steeply at about  $5'$  from the center for HCG 62. This is caused by the observed sharp drop of the temperature. There is a possibility that these regions are not in the hydrostatic equilibrium.

# Appendix A

## Energy spectra for HCG 62

### A.1 $1-T$ results

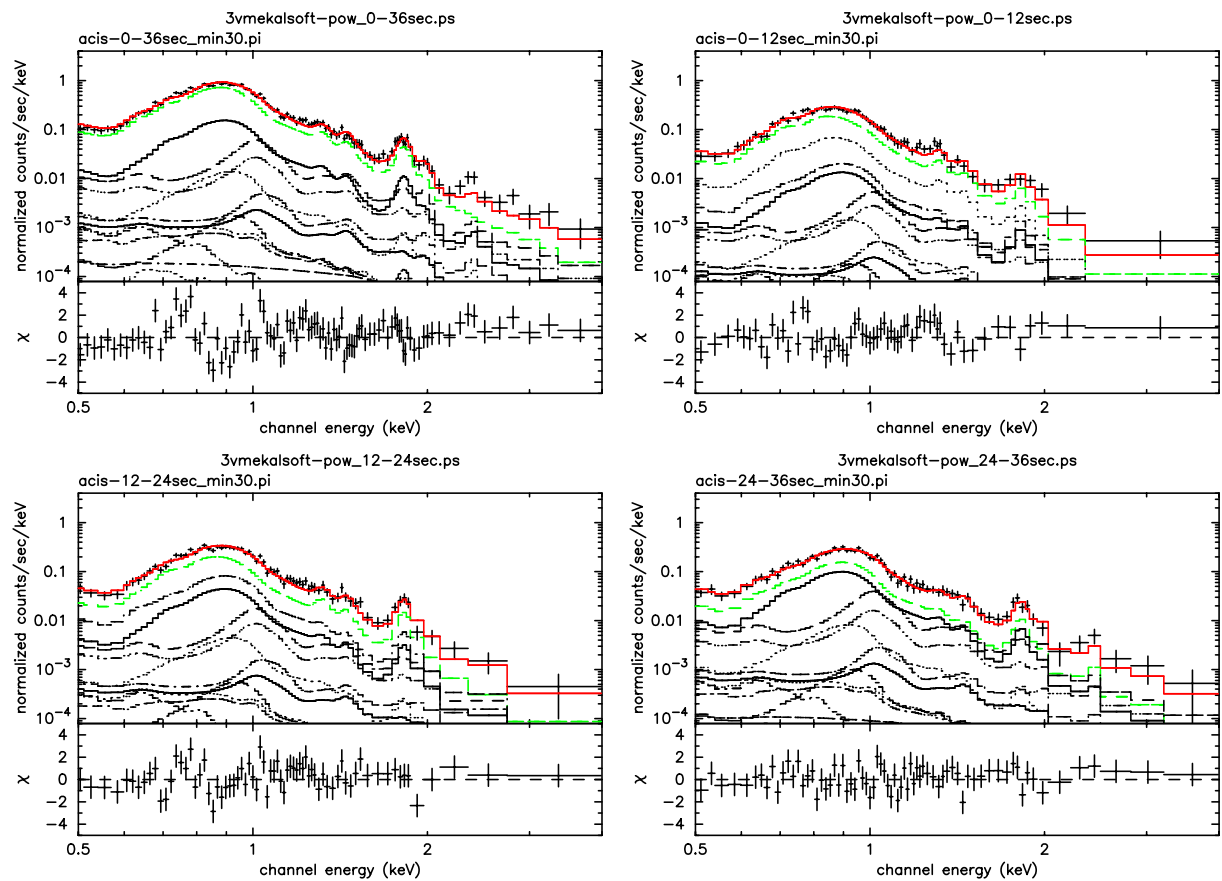


Fig. A.1: Chandra ACIS-S3 spectra in the 0-0.6', 0-0.2', 0.2-0.4', and 0.4-0.6' annulus fitted with the deprojected  $1-T$  model

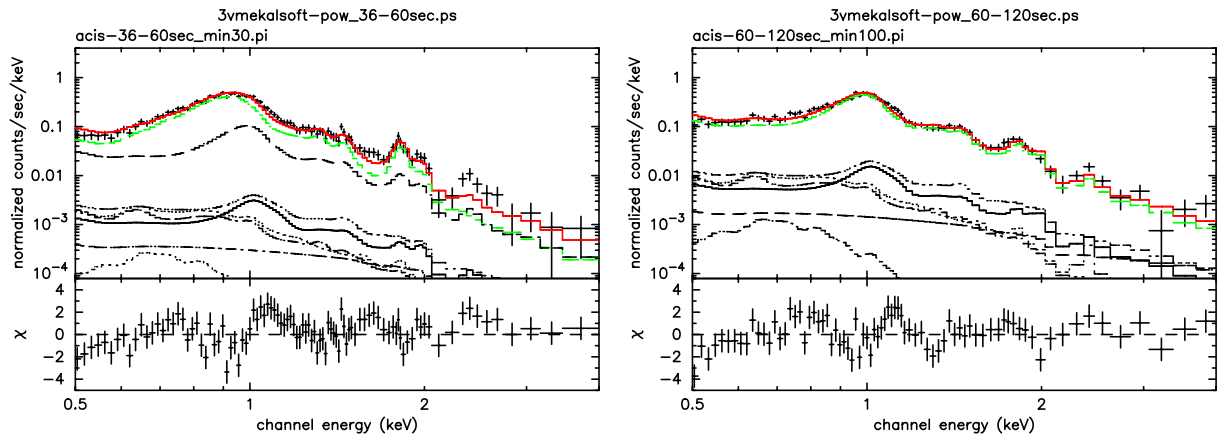


Fig. A.2: Chandra ACIS-S3 spectra in the 0.6-1.0' and 1.0-2.0' annulus fitted with the deprojected 1- $T$  model

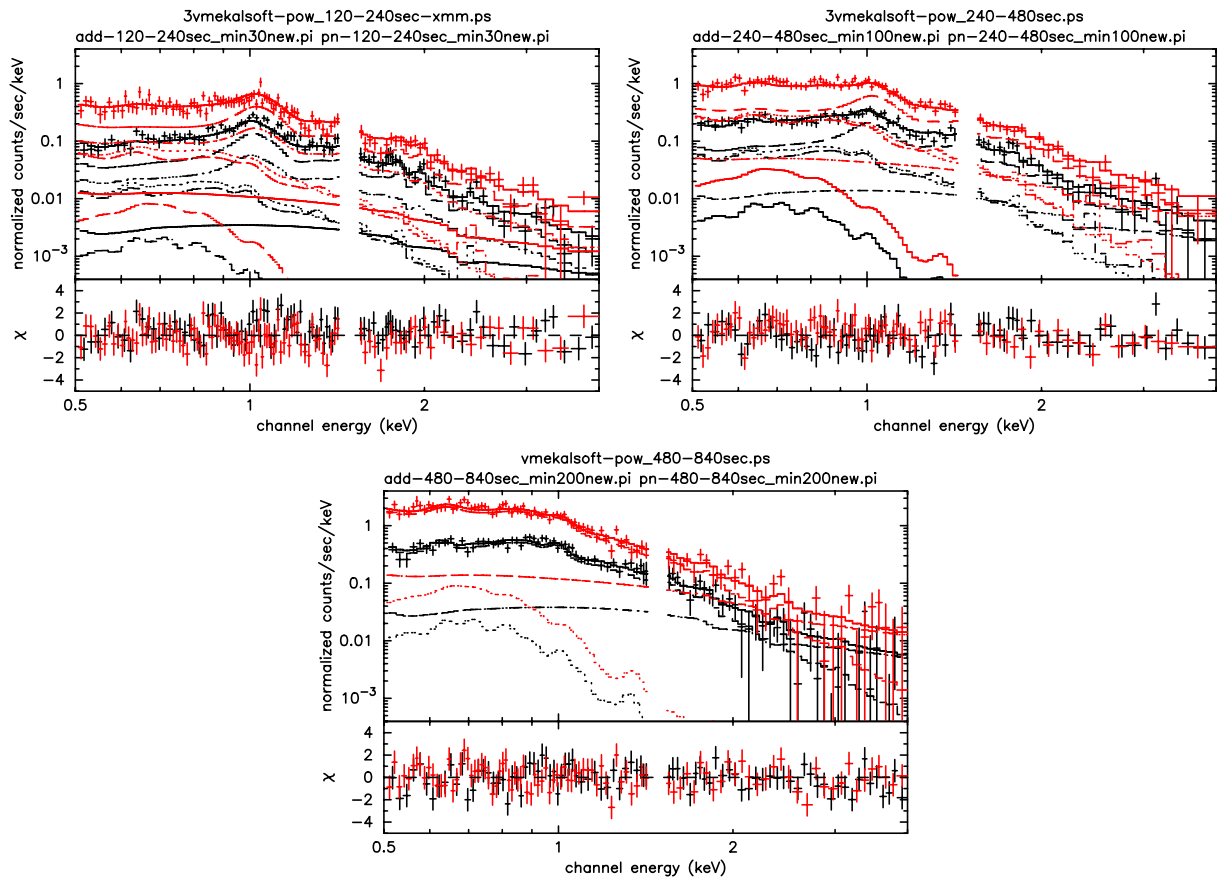


Fig. A.3: MOS1+2 (black) and pn (red) spectra in the 2.0-4.0' and 4.0-8.0' annulus fitted with the deprojected 1- $T$  model. In the 8.0-14.0' annulus fitted with the projected model.

## A.2 2-T results

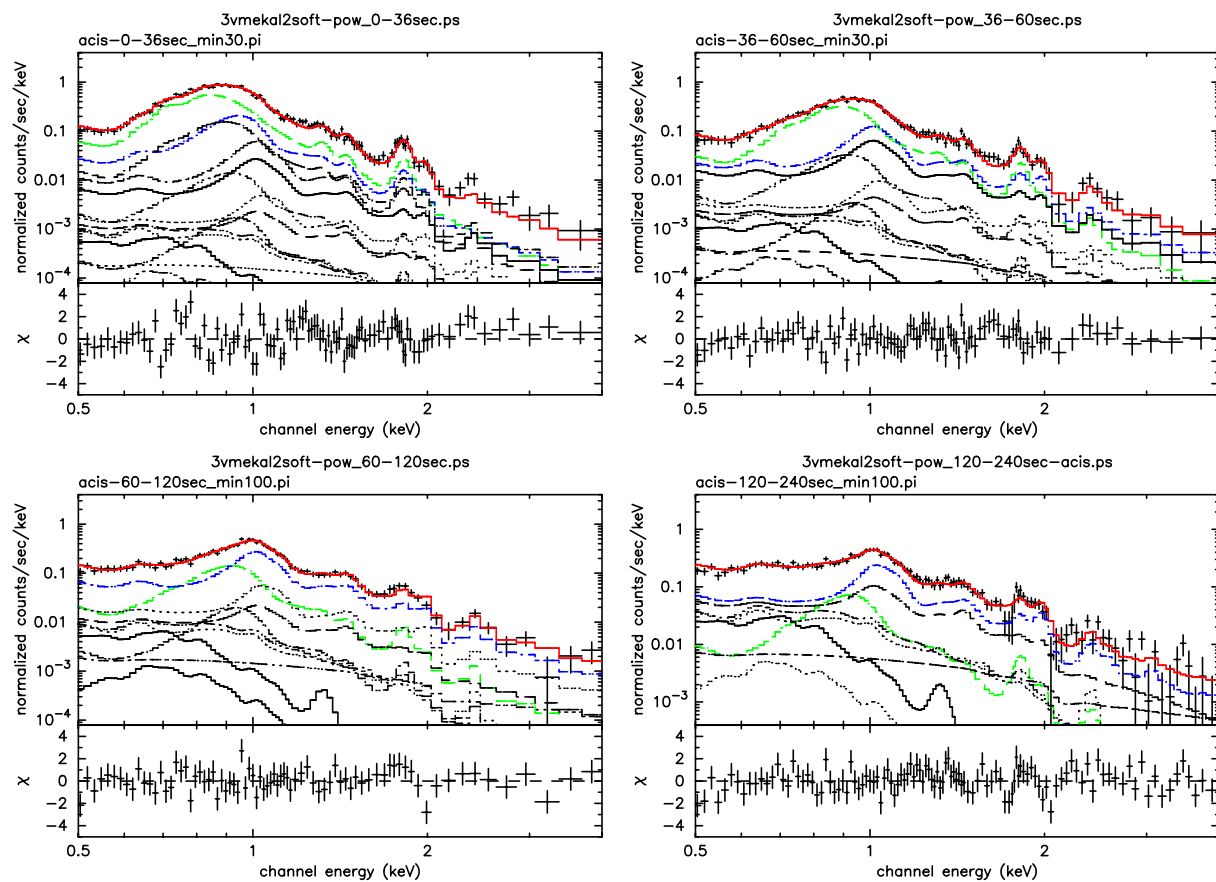


Fig. A.4: Chandra ACIS-S3 spectra in the 0-0.6', 0.6-1.0', 1.0-2.0' and 2.0-4.0' annulus fitted with the deprojected 2-T model

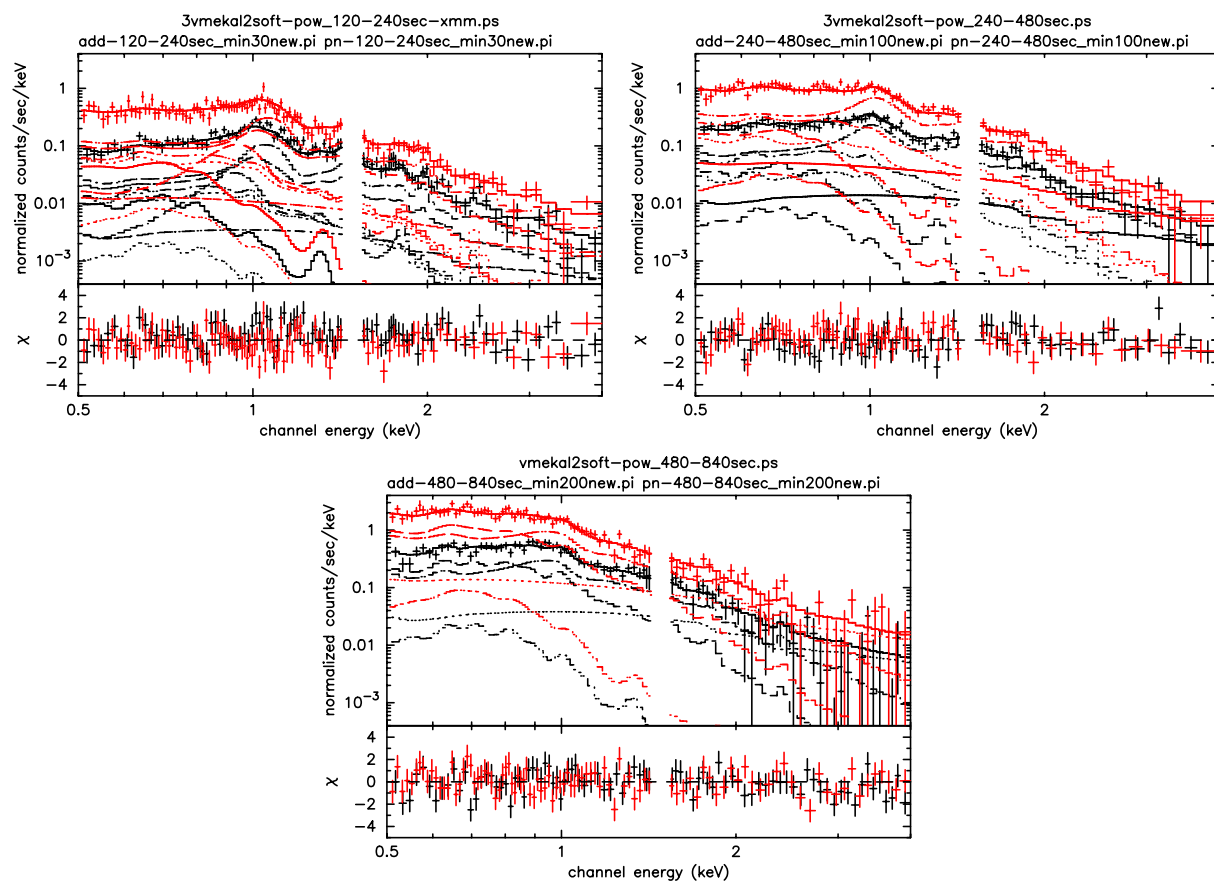


Fig. A.5: MOS1+2 (black) and pn (red) spectra in the 2.0-4.0' and 4.0-8.0' annulus fitted with the deprojected 2- $T$  model. In the 8.0-14.0' annulus fitted with the projected model.

## Appendix B

# Soft background estimation

Table B.1: Observation log checked on soft background for sources around HCG 62a. Optical coordinates and exposure by Observation Viewer of WebChaSeR.  $n_{\text{H}}$  was estimated by “HEAsoft calculate nH”. NGC4782/3 was observed with VFAINT mode.

Name	obsID	date	exposure (ks)	R.A.	Dec.
HCG62	921	2000/01/25	49.15	12h53m05.63s	-09D12'15.46"
NGC4697	784	2000/02/08	39.76	12h48m35.00s	-05D47'21.00"
Q1246-0542	821	2000/01/15	5.55	12h49m13.80s	-05D59'19.20"
NGC4594	1586	2001/05/31	18.75	12h39m59.00s	-11D37'28.00"
NGC4782/3	3220	2002/06/16	49.96	12h54m36.00s	-12D33'50.00"
	l	b	$n_{\text{H}}$ ( $10^{20} \text{ cm}^{-2}$ )		
	303.621626	53.665237	3.0		
	301.625562	57.075341	2.2		
	301.927204	56.878774	2.1		
	298.457928	51.147772	3.8		
	304.139914	50.300443	3.6		

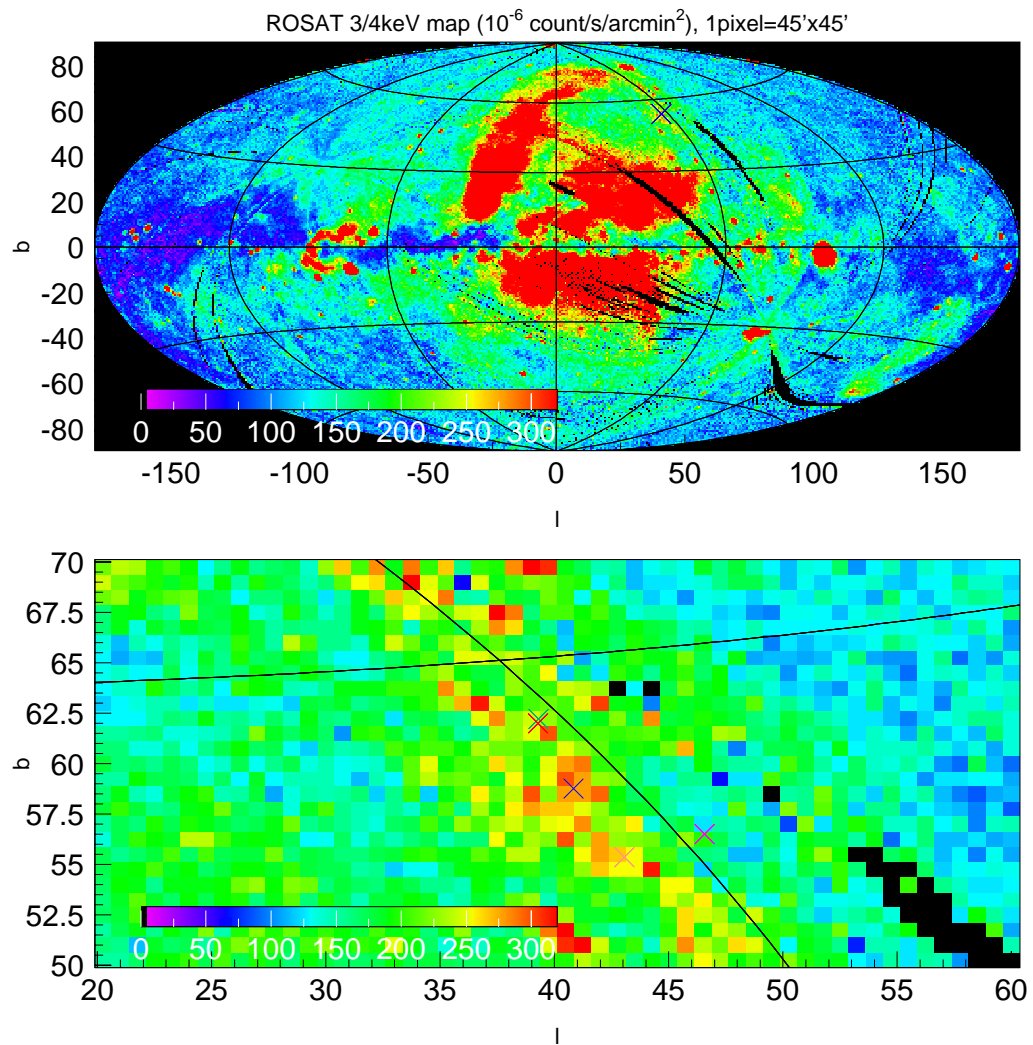


Fig. B.1: ROSAT 3/4keV map. HCG 62, ngc4697, q1246-0542, ngc4782 and ngc4594 indicated by blue, green, red, yellow and mazenta crosses, respectively.

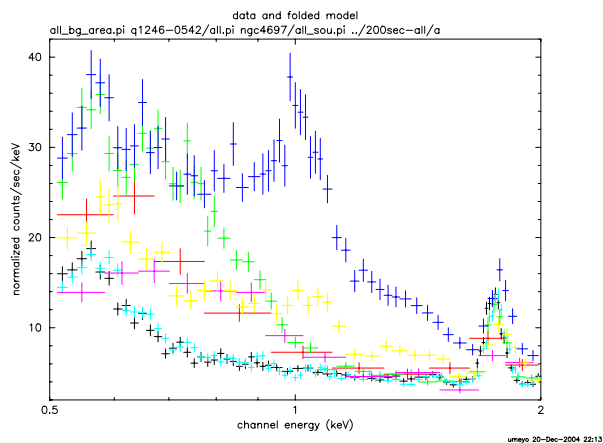
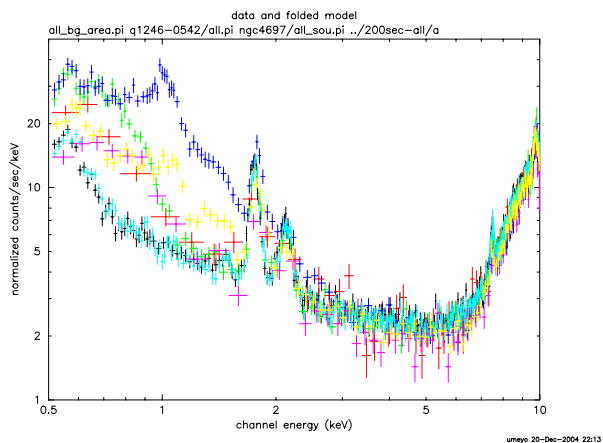


Fig. B.2: Background energy spectra around HCG 62a by Chandra. HCG 62 ( $r > 200''$ ), ngc4697 ( $r > 95''$ ), q1246-0542 (over the chip), ngc4782 ( $r > 180''$ ), ngc4594 ( $r > 180''$ ), using Blank-sky (over the chip) and the newest Blank-sky (over the chip) indicated by blue, green, red, yellow, magenta, black and cyan crosses, respectively. Point source were excluded.

Fig. B.3: Same as figure B.2, but in the 0.5-2keV band.



## Appendix C

# Deprojection

In figure C.1, the volume,  $V_N$ , is calculated as,

$$V_N = \frac{4}{3}\pi \left( r_N^2 - r_{N-1}^2 \right)^{\frac{3}{2}}, \quad (\text{C.1})$$

and the volume,  $V_N^m$ , for  $m < N$  is

$$V_N^m = \frac{4}{3}\pi \left\{ (r_N^2 - r_{m-1}^2)^{\frac{3}{2}} - (r_N^2 - r_m^2)^{\frac{3}{2}} - (r_{N-1}^2 - r_{m-1}^2)^{\frac{3}{2}} + (r_{N-1}^2 - r_m^2)^{\frac{3}{2}} \right\}. \quad (\text{C.2})$$

The observed flux  $F_m^{\text{obs}}$  in the projected  $r_{m-1} < r < r_m$  annulus is the sum of flux from the volumes,  $V_m, V_{m+1}^m, \dots, V_N^m$ . If we define the flux from the volume  $V_i$  as  $f_i$ ,

$$F_m^{\text{obs}} = f_m + \frac{V_{m+1}^m}{V_{m+1}} f_{m+1} + \dots + \frac{V_N^m}{V_N} f_N = \sum_{i=m}^N \frac{V_i^m}{V_i} f_i, \quad (\text{C.3})$$

assuming the spherical symmetry and  $V_i^i \equiv V_i$ . Because the volume of the  $r_{m-1} < r < r_m$  crust is  $W_m = \frac{4}{3}\pi (r_m^3 - r_{m-1}^3)$ , the flux contribution in the 3-dimensional range of  $r_{m-1} < r < r_m$  is

$$F_m^{\text{3D}} = \frac{W_m}{V_m} f_m = \frac{r_m^3 - r_{m-1}^3}{(r_m^2 - r_{m-1}^2)^{3/2}} f_m. \quad (\text{C.4})$$

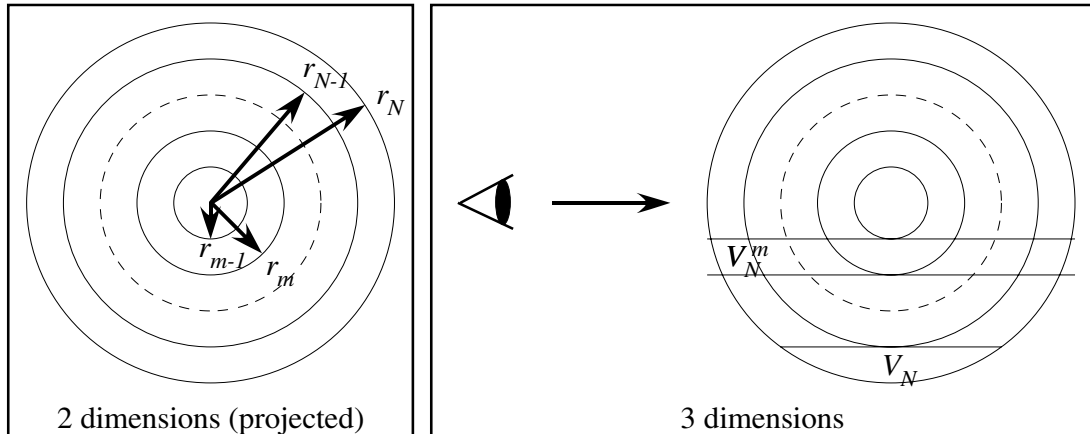


Fig. C.1: deprojection image



## Appendix D

### The ratio of Si abundance

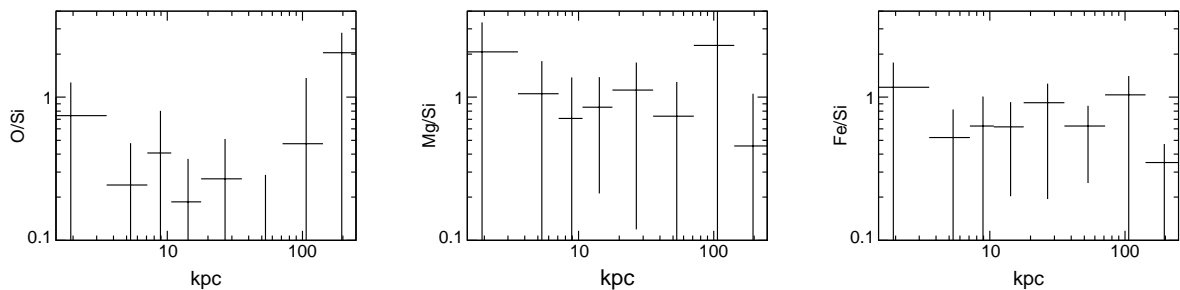


Fig. D.1: The ratio of Si to O, Mg, and Fe abundances.

The ratio,  $\text{Mg}/\text{O}$ , is  $4.0 \pm 2.5$  times solar within 20 kpc ( $1'$ ) based on the  $2-T$  fit. This value is similar or somewhat larger than those in other groups:  $2.5 \pm 0.4$  solar for NGC 5044 (Xu et al. 2002),  $1.3 \pm 0.2$  for NGC 4636 (Tamura et al. 2003), both measured with RGS, and  $\sim 2$  solar in RGH 80 (Xue et al. 2004). In M87, this ratio is  $1.3 \pm 0.1$  solar within 20 kpc. We note that in HCG 62 the radial profile of Mg abundance is close to the Si profile, implying that Mg may have the similar origin as Si, i.e. a mixture of SN II and SN Ia products. Considering that oxygen is the pure product of SN II, the marginally high  $\text{Mg}/\text{O}$  value suggests that the shallow potential of HCG 62 is unable to confine SN II products which should have been supplied in the form of galactic winds.

If excess Fe in the center is produced by enhanced SN Ia activity of HCG 62a, it should be related with the central cool component which is the gas directly bound by the central galaxy. The region of high metal abundance almost coincides with the volume dominated by the stellar mass, which supports the natural view that stars are responsible for the production of excess iron and silicon around the group center. This suggests either that the Fe production has occurred in a wider region than the galaxy itself or that there have been an outflow of Fe. The presence of cavities in HCG 62 suggests that part of the central metal-rich gas may have been lifted from the galaxy.



# Bibliography

- Anders, E., & Grevesse, N. 1989, *Geochim. Cosmochim. Acta*, 53, 197
- Arnaud, M., Rothenflug, R., Boulade, O., Vigroux, L., & Vangioni-Flam, E. 1992, *A&A*, 254, 49
- Arp, H. 1997, *ApJ*, 474, 74
- Bahcall, N. A., Lubin, L. M., & Dorman, V. 1995, *ApJL*, 447, L81+
- Belsole, E., Sauvageot, J.-L., Ponman, T. J., & Bourdin, H. 2003, *A&A*, 398, 1
- Bîrzan, L., Rafferty, D. A., McNamara, B. R., Wise, M. W., & Nulsen, P. E. J. 2004, *ApJ*, 607, 800
- Blanton, E. L., Gregg, M. D., Helfand, D. J., Becker, R. H., & Leighly, K. M. 2001, *AJ*, 121, 2915
- Boehringer, H., Voges, W., Fabian, A. C., Edge, A. C., & Neumann, D. M. 1993, *MNRAS*, 264, L25
- Buote, D. A. 2000a, *ApJ*, 539, 172
- . 2000b, *MNRAS*, 311, 176
- . 2002, *ApJL*, 574, L135
- Buote, D. A., Lewis, A. D., Brighenti, F., & Mathews, W. G. 2003a, *ApJ*, 594, 741
- . 2003b, *ApJ*, 595, 151
- Chandran, B. D. G., & Maron, J. L. 2004, *ApJ*, 602, 170
- Churazov, E., Brüggen, M., Kaiser, C. R., Böhringer, H., & Forman, W. 2001, *ApJ*, 554, 261
- Condon, J. J., Cotton, W. D., Greisen, E. W., Yin, Q. F., Perley, R. A., Taylor, G. B., & Broderick, J. J. 1998, *AJ*, 115, 1693
- Coziol, R., Brinks, E., & Bravo-Alfaro, H. 2004, *AJ*, 128, 68
- Coziol, R., Ribeiro, A. L. B., de Carvalho, R. R., & Capelato, H. V. 1998, *ApJ*, 493, 563
- De Grandi, S., Etti, S., Longhetti, M., & Molendi, S. 2004, *A&A*, 419, 7
- Diaferio, A., Geller, M. J., & Ramella, M. 1994, *AJ*, 107, 868
- Dickey, J. M., & Lockman, F. J. 1990, *ARA&A*, 28, 215

- Dunn, R. J. H., & Fabian, A. C. 2004, *MNRAS*, 355, 862
- Dunn, R. J. H., Fabian, A. C., & Taylor, G. B. 2005, *MNRAS*, 364, 1343
- Ettori, S., & Fabian, A. C. 2000, *MNRAS*, 317, L57
- Fabian, A. C., Celotti, A., Blundell, K. M., Kassim, N. E., & Perley, R. A. 2002, *MNRAS*, 331, 369
- Fabian, A. C., Sanders, J. S., Ettori, S., Taylor, G. B., Allen, S. W., Crawford, C. S., Iwasawa, K., Johnstone, R. M., & Ogle, P. M. 2000, *MNRAS*, 318, L65
- Finoguenov, A., & Jones, C. 2001, *ApJL*, 547, L107
- Finoguenov, A., & Ponman, T. J. 1999, *MNRAS*, 305, 325
- Forman, W., & Jones, C. 1982, *ARA&A*, 20, 547
- Fukazawa, Y., Kawano, N., Ohta, A., & Mizusawa, H. 2002, *PASJ*, 54, 527
- Fukazawa, Y., Makishima, K., Matsushita, K., Yamasaki, N., Ohashi, T., Mushotzky, R. F., Sakima, Y., Tsusaka, Y., & Yamashita, K. 1996, *PASJ*, 48, 395
- Fukazawa, Y., Nakazawa, K., Isobe, N., Makishima, K., Matsushita, K., Ohashi, T., & Kamae, T. 2001, *ApJL*, 546, L87
- Fukugita, M., Hogan, C. J., & Peebles, P. J. E. 1998, *ApJ*, 503, 518
- Fusco-Femiano, R., dal Fiume, D., Feretti, L., Giovannini, G., Grandi, P., Matt, G., Molendi, S., & Santangelo, A. 1999, *ApJL*, 513, L21
- Governato, F., Tozzi, P., & Cavaliere, A. 1996, *ApJ*, 458, 18
- Govoni, F. & Fertti, L. 2005, *IJM Phys D*
- Grant, C. E., Bautz, M. W., Kissel, S. M., LaMarr, B., & Prigozhin, G. Y. 2005, in *UV, X-Ray, and Gamma-Ray Space Instrumentation for Astronomy XIV*. Edited by Siegmund, Oswald H. W. *Proceedings of the SPIE*, Volume 5898, pp. 201-211 (2005)., ed. O. H. W. Siegmund, 201–211
- Green, P. J., Schartel, N., Anderson, S. F., Hewett, P. C., Foltz, C. B., Brinkmann, W., Fink, H., Truemper, J., & Margon, B. 1995, *ApJ*, 450, 51
- Grevesse, N., & Sauval, A. J. 1998, *Space Science Reviews*, 85, 161
- Harrison, F. A., Eckart, M. E., Mao, P. H., Helfand, D. J., & Stern, D. 2003, *ApJ*, 596, 944
- Heckman, T. M., Armus, L., & Miley, G. K. 1990, *ApJS*, 74, 833
- Helsdon, S. F., & Ponman, T. J. 2000, *MNRAS*, 319, 933
- . 2003, *MNRAS*, 340, 485
- Helsdon, S. F., Ponman, T. J., O'Sullivan, E., & Forbes, D. A. 2001, *MNRAS*, 325, 693
- Hickson, P. 1982, *ApJ*, 255, 382

- . 1993, *Astrophysical Letters Communications*, 29, 1
- . 1997, *ARA&A*, 35, 357
- Hickson, P., Kindl, E., & Auman, J. R. 1989, *ApJS*, 70, 687
- Ikebe, Y., Ezawa, H., Fukazawa, Y., Hirayama, M., Izhisaki, Y., Kikuchi, K., Kubo, H., Makishima, K., Matsushita, K., Ohashi, T., Takahashi, T., & Tamura, T. 1996, *Nature*, 379, 427
- Ikebe, Y., Makishima, K., Fukazawa, Y., Tamura, T., Xu, H., Ohashi, T., & Matsushita, K. 1999, *ApJ*, 525, 58
- Inoue, H., Koyama, K., Matsuoka, M., Ohashi, T., Tanaka, Y., & Tsunemi, H. 1980, *ApJ*, 238, 886
- Iwamoto, K., Brachwitz, F., Nomoto, K., Kishimoto, N., Umeda, H., Hix, W. R., & Thielemann, F.-K. 1999, *ApJS*, 125, 439
- Jansen, F., Lumb, D., Altieri, B., Clavel, J., Ehle, M., Erd, C., Gabriel, C., Guainazzi, M., Gondoin, P., Much, R., Munoz, R., Santos, M., Schartel, N., Texier, D., & Vacanti, G. 2001, *A&A*, 365, L1
- Jones, C., & Forman, W. 1984, *ApJ*, 276, 38
- Kaastra, J. S. 1992, Internal SRON-Leiden Report, updated version 2.0
- Kaastra, J. S., & Mewe, R. 1993, *A&AS*, 97, 443
- Kataoka, J., & Stawarz, L. 2005, *ApJ*, 622, 797
- Katayama, H., Takahashi, I., Ikebe, Y., Matsushita, K., & Freyberg, M. J. 2004, *A&A*, 414, 767
- Kennicutt, Jr., R. C. 1998, *ARA&A*, 36, 189
- LaMarr, B. 2003, ACIS Memo #181
- Lehnert, M. D., Heckman, T. M., & Weaver, K. A. 1999, *ApJ*, 523, 575
- Liedahl, D. A., Osterheld, A. L., & Goldstein, W. H. 1995, *ApJL*, 438, L115
- Makishima, K., Ishida, M., Ohashi, T., Dotani, T., Inoue, H., Mitsuda, K., Tanaka, Y., Turner, M. J. L., & Hoshi, R. 1989, *PASJ*, 41, 531
- Mamon, G. A. 1986, *ApJ*, 307, 426
- Markevitch, M. 2004, <http://cxc.harvard.edu/contrib/maxim/acisbg/>
- Markevitch, M., Mazzotta, P., Vikhlinin, A., Burke, D., Butt, Y., David, L., Donnelly, H., Forman, W. R., Harris, D., Kim, D.-W., Virani, S., & Vrtilik, J. 2003, *ApJL*, 586, L19
- Markevitch, M., Ponman, T. J., Nulsen, P. E. J., Bautz, M. W., Burke, D. J., David, L. P., Davis, D., Donnelly, R. H., Forman, W. R., Jones, C., Kaastra, J., Kellogg, E., Kim, D.-W., Kolodziejczak, J., Mazzotta, P., Pagliaro, A., Patel, S., Van Speybroeck, L., Vikhlinin, A., Vrtilik, J., Wise, M., & Zhao, P. 2000, *ApJ*, 541, 542

- Matsumoto, H., Koyama, K., Awaki, H., Tsuru, T., Loewenstein, M., & Matsushita, K. 1997, *ApJ*, 482, 133
- Matsushita, K. 1998, Ph. D thesis, The University of Tokyo
- Matsushita, K., Belsole, E., Finoguenov, A., & Böhringer, H. 2002, *A&A*, 386, 77
- Matsushita, K., Finoguenov, A., & Böhringer, H. 2003, *A&A*, 401, 443
- Matsushita, K., Makishima, K., Awaki, H., Canizares, C. R., Fabian, A. C., Fukazawa, Y., Loewenstein, M., Matsumoto, H., Mihara, T., Mushotzky, R. F., Ohashi, T., Ricker, G. R., Serlemitsos, P. J., Tsuru, T., Tsusaka, Y., & Yamazaki, T. 1994, *ApJL*, 436, L41
- Matsushita, K., Ohashi, T., & Makishima, K. 2000, *PASJ*, 52, 685
- Mazzotta, P., Kaastra, J. S., Paerels, F. B., Ferrigno, C., Colafrancesco, S., Mewe, R., & Forman, W. R. 2002, *ApJL*, 567, L37
- McNamara, B. R., Wise, M., Nulsen, P. E. J., David, L. P., Sarazin, C. L., Bautz, M., Markevitch, M., Vikhlinin, A., Forman, W. R., Jones, C., & Harris, D. E. 2000, *ApJL*, 534, L135
- McNamara, B. R., Wise, M. W., Nulsen, P. E. J., David, L. P., Carilli, C. L., Sarazin, C. L., O’Dea, C. P., Houck, J., Donahue, M., Baum, S., Voit, M., O’Connell, R. W., & Koekemoer, A. 2001, *ApJL*, 562, L149
- Mewe, R., Gronenschild, E. H. B. M., & van den Oord, G. H. J. 1985, *A&AS*, 62, 197
- Mewe, R., Lemen, J. R., & van den Oord, G. H. J. 1986, *A&AS*, 65, 511
- Mulchaey, J. S. 2000, *ARA&A*, 38, 289
- Mulchaey, J. S., Davis, D. S., Mushotzky, R. F., & Burstein, D. 1996, *ApJ*, 456, 80
- . 2003, *ApJS*, 145, 39
- Mulchaey, J. S., & Zabludoff, A. I. 1998, *ApJ*, 496, 73
- Mushotzky, R., Figueroa-Feliciano, E., Loewenstein, M., & Snowden, S. L. 2003, *ArXiv Astrophysics e-prints*
- Nakai, N., Hayashi, M., Handa, T., Sofue, Y., Hasegawa, T., & Sasaki, M. 1987, *PASJ*, 39, 685
- Navarro, J. F., Frenk, C. S., & White, S. D. M. 1996, *ApJ*, 462, 563
- . 1997, *ApJ*, 490, 493
- Nevalainen, J., Markevitch, M., & Lumb, D. 2005, *ApJ*, 629, 172
- Nishiura, S., Shimada, M., Ohyama, Y., Murayama, T., & Taniguchi, Y. 2000, *AJ*, 120, 1691
- Nomoto, K., Tominaga, N., Umeda, H., Kobayashi, C., & Maeda, K. 2006, *Nuclear Physics A*, 777, 424
- Norman, C. A., & Ikeuchi, S. 1989, *ApJ*, 345, 372

- Ohto, A., Kawano, N., & Fukazawa, Y. 2003, PASJ, 55, 819
- Oshima, T. 2003, Ph. D thesis, The University of Tokyo
- Osmond, J. P. F., & Ponman, T. J. 2004, MNRAS, 350, 1511
- O’Sullivan, E., Vrtilik, J. M., & Kempner, J. C. 2005, ApJL, 624, L77
- Pildis, R. A., Bregman, J. N., & Evrard, A. E. 1995, ApJ, 443, 514
- Ponman, T. J., & Bertram, D. 1993, Nature, 363, 51
- Ponman, T. J., Bourner, P. D. J., Ebeling, H., & Bohringer, H. 1996, MNRAS, 283, 690
- Ponman, T. J., Cannon, D. B., & Navarro, J. F. 1999, Nature, 397, 135
- Rasmussen, A., Kahn, S. M., & Paerels, F. 2003, in *The IGM/Galaxy Connection: The Distribution of Baryons at  $z=0$* , ed. J. L. Rosenberg & M. E. Putman (Dordrecht: Kluwer Academic Publishers), 109
- Read, A. M., & Ponman, T. J. 2003, A&A, 409, 395
- Rephaeli, Y., Gruber, D., & Blanco, P. 1999, ApJL, 511, L21
- Rubin, V. C., Ford, Jr., W. K., Thonnard, N., & Burstein, D. 1982, ApJ, 261, 439
- Rybicki, G. B., & Lightman, A. P. 1979, *Radiative processes in astrophysics* (New York, Wiley-Interscience, 1979. 393 p.)
- Sanders, D. B., & Mirabel, I. F. 1996, ARA&A, 34, 749
- Sarazin, C. L. 1988, S&T, 76, 639
- Schmidt, R. W., Fabian, A. C., & Sanders, J. S. 2002, MNRAS, 337, 71
- Shimada, M., Ohyama, Y., Nishiura, S., Murayama, T., & Taniguchi, Y. 2000a, AJ, 119, 2664
- . 2000b, AJ, 119, 2664
- Spitzer, L. 1962, *Physics of Fully Ionized Gases* (Physics of Fully Ionized Gases, New York: Interscience (2nd edition), 1962)
- Stevens, J. B., Webster, R. L., Barnes, D. G., Pisano, D. J., & Drinkwater, M. J. 2004, *Publications of the Astronomical Society of Australia*, 21, 318
- Strickland, D. K., Heckman, T. M., Colbert, E. J. M., Hoopes, C. G., & Weaver, K. A. 2004a, ApJS, 151, 193
- . 2004b, ApJ, 606, 829
- Strickland, D. K., Heckman, T. M., Weaver, K. A., Hoopes, C. G., & Dahlem, M. 2002, ApJ, 568, 689
- Strickland, D. K., Ponman, T. J., & Stevens, I. R. 1997, A&A, 320, 378
- Sulentic, J. W. 1997, ApJ, 482, 640
- Tamura, T., Kaastra, J. S., Makishima, K., & Takahashi, I. 2003, A&A, 399, 497

- Thielemann, F.-K., Nomoto, K., & Hashimoto, M.-A. 1996, *ApJ*, 460, 408
- Tran, K.-V. H., Simard, L., Zabludoff, A. I., & Mulchaey, J. S. 2001, *ApJ*, 549, 172
- Tremaine, S., Gebhardt, K., Bender, R., Bower, G., Dressler, A., Faber, S. M., Filippenko, A. V., Green, R., Grillmair, C., Ho, L. C., Kormendy, J., Lauer, T. R., Magorrian, J., Pinkney, J., & Richstone, D. 2002, *ApJ*, 574, 740
- Tsujimoto, T., Nomoto, K., Yoshii, Y., Hashimoto, M., Yanagida, S., & Thielemann, F.-K. 1995, *MNRAS*, 277, 945
- Tully, R. B. 1987, *ApJ*, 323, 1
- Verdes-Montenegro, L., Yun, M. S., Williams, B. A., Huchtmeier, W. K., Del Olmo, A., & Perea, J. 2001, *A&A*, 377, 812
- Vrtilek, J. e. a. 2001, *Chandra News Releases*, 08
- Vrtilek, J. M., Grego, L., David, L. P., Ponman, T. J., Forman, W., Jones, C., & Harris, D. E. 2002, *APS Meeting Abstracts*, 17107
- Walke, D. G., & Mamon, G. A. 1989, *A&A*, 225, 291
- Wang, J.-M., & Hu, C. 2005, *ApJL*, 630, L125
- Wang, Q. D., & McCray, R. 1993, *ApJL*, 409, L37
- Xu, H., Kahn, S. M., Peterson, J. R., Behar, E., Paerels, F. B. S., Mushotzky, R. F., Jernigan, J. G., Brinkman, A. C., & Makishima, K. 2002, *ApJ*, 579, 600
- Xue, Y.-J., Böhringer, H., & Matsushita, K. 2004, *A&A*, 420, 833
- Young, A. J., Wilson, A. S., & Mundell, C. G. 2002, *ApJ*, 579, 560
- Young, P. J. 1976, *AJ*, 81, 807
- Zabludoff, A. I., & Mulchaey, J. S. 2000, *ApJ*, 539, 136

# List of Figures

2.1	Hubble tuning-fork diagram. . . . .	11
2.2	Calculated X-ray spectra from optically thin hot plasma with various temperatures. . . . .	14
2.3	The relation between the spiral fraction $f_{\text{sp}}$ and the X-ray luminosity $L_X$ . . . . .	15
2.4	X-ray contours of the HCG 57 overlaid on the optical image. . . . .	16
2.5	Left: Iron mass in the cluster hot gas against the optical luminosities for the clusters. Right: BCG optical magnitude as a function of iron mass excess. . . . .	18
2.6	the energy spectra of NGC 4636. . . . .	18
2.7	$L_X - kT$ relation . . . . .	20
2.8	Left: The energy spectrum of the Coma Cluster. Right: ASCA image of HCG 62 in hard band. . . . .	21
2.9	M 82 and NGC 253 images . . . . .	23
2.10	HydraA image . . . . .	23
2.11	X-ray image of Perseus cluster. . . . .	24
2.12	Galaxy distribution of HCG 62. HCG 62a, HCG 62b and HCG 62c are indicated in red, green and blue, respectively. . . . .	28
3.1	The schematic view of the <i>Chandra</i> satellite . . . . .	29
3.2	HRMA mirrors . . . . .	30
3.3	Effective area vs. X-ray energy and off-axis angle . . . . .	31
3.4	Simulated on-axis images . . . . .	32
3.5	Encircled energy radius of HRMA . . . . .	32
3.6	The quantum efficiency of the ACIS CCDs . . . . .	33
3.7	The light path in <i>XMM-Newton</i> 's XRT with the PN camera in focus . . . . .	34
3.8	The light path in <i>XMM-Newton</i> 's XRT with the MOS and RGA . . . . .	34
3.9	On-axis images of the MOS1, MOS2 and PN XRTs (left to right). . . . .	35
3.10	Radial counts distribution for the on-axis PSF of the MOS1 XRT in the 0.75–2.25 keV energy range. . . . .	35
3.11	The net effective area of all <i>XMM-Newton</i> XRT, combined with the response characteristics of the focal detectors. . . . .	35

3.12	A rough sketch of the field of view of the two types of EPIC cameras (MOS, left; PN, right). . . . .	36
3.13	(a)effective areas, (b)background spectra . . . . .	37
4.1	Optical and X-ray images of the spiral-only group HCG 80. . . . .	40
4.2	Radial profile fitting for HCG 80a and b with the PSF and Gaussian(s) models. . . . .	43
4.3	Minor-axis and major-axis X-ray surface brightness distributions. . . . .	44
4.4	Chandra ACIS-S3 spectra of HCG 80a and HCG 80b. . . . .	47
4.5	$L_X - f_{\text{spiral}}$ relation. . . . .	50
4.6	$L_X - L_B$ relation. . . . .	51
5.1	X-ray spectra of Chandra ACIS-S3, XMM-Newton MOS1+2, and pn, in 0.5–4 keV within $r < 2'$ . . . . .	60
5.2	(a) Gaussian smoothed Chandra ACIS-S3 X-ray image. (b) STScI Digitized Sky Survey (DSS) image of HCG 62. . . . .	61
5.3	(a) Same as figure 5.2, but the central region of HCG 62 is expanded. (b) Combined image with MOS1 and MOS2 detectors. . . . .	64
5.4	The radial profiles of the surface brightness of HCG 62 in 0.5–4 keV around the central galaxy HCG 62a . . . . .	66
5.5	(a) Color-coded map of the relative deviation of the flux from the best-fit 2- $\beta$ model based on the 2-dimensional fit. (b) Residual of the observed count to the 2- $\beta$ model. (c) Ratio of the residual counts divided by the 2- $\beta$ model. . . . .	67
5.6	Color coded temperature map (J2000) based on the hardness ratio. . . . .	68
5.7	Chandra ACIS-S3 X-ray spectra for cavity regions and non-cavity regions. . . . .	71
5.8	(a) Chandra ACIS-S3 (green), MOS1+2 (black), and pn (red) spectra within $r \leq 2'$ around HCG 62a. (b) Same as (a), but in the 2–4' annulus fitted with the deprojected 2- $T$ model. . . . .	75
5.9	(a) Temperature profiles with the 1- $T$ vMekal models based on the deprojected spectral fit. (b) Same as (a), but with the 2- $T$ vMekal models. . . . .	78
5.10	Abundance profiles of O, Mg, Si, and Fe using the 1- $T$ (crosses) and 2- $T$ (diamonds) vMekal models. . . . .	79
5.11	(a) Volume filling factor $f(R)$ of the cool component, (b) cool or hot gas temperature $kT_1$ or $kT_2$ , and (c) gas pressure $P_{\text{gas}}$ , (d) cool or hot electron density. (e) A black line indicates the total integrated gravitational mass, $M_{<R}$ , estimated from the best fit models. (f) Same as (e), but for the differential mass density profiles. . . . .	82
A.1	Chandra ACIS-S3 spectra with the 1- $T$ model (1) . . . . .	97
A.2	Chandra ACIS-S3 spectra with the 1- $T$ model (2) . . . . .	98
A.3	MOS1+2 and pn spectra with the 1- $T$ model . . . . .	98
A.4	Chandra ACIS-S3 spectra with the 2- $T$ model . . . . .	99

A.5	MOS1+2 and pn spectra with the $2-T$ model . . . . .	100
B.1	ROSAT 3/4keV map. . . . .	102
B.2	Energy spectra around HCG 62a . . . . .	103
B.3	Same as figure B.2, but in the 0.5-2keV band. . . . .	103
C.1	deprojection image . . . . .	105
D.1	The ratio of Si to O, Mg, Fe abundances. . . . .	107



# List of Tables

1.1	Properties of four well-studied spiral dominant group: $kT$ indicates approximate temperature when a thermal spectrum is assumed, and $L_X$ is the bolometric luminosity of the diffuse emission only. . . . .	6
2.1	Definitions of the solar abundances by number (Anders & Grevesse 1989). . . . .	14
3.1	Basic performance of the EPIC detectors . . . . .	33
4.1	Optical properties of member galaxies. . . . .	40
4.2	X-ray count rates, fluxes, and hardness ratios for member galaxies. . . . .	41
4.3	Results of the 1D fitting for HCG 80a in the soft band. . . . .	44
4.4	Results of spectral fittings for HCG 80a and HCG 80b. . . . .	48
4.5	Halo, disk, nuclear, and total luminosities. . . . .	52
5.1	Optical properties of HCG 62 and member galaxies. . . . .	62
5.2	X-ray properties of detected galaxies by Chandra ACIS-S3. . . . .	62
5.3	Best fit parameters of the radial surface brightness profiles with ACIS-S3 ( $r < 4'$ ) and MOS1 ( $1' < r < 14'$ ) in 0.5–4 keV by the 3- $\beta$ model. . . . .	65
5.4	Best fit parameters by the 2-dimensional 2- $\beta$ model for the central region ( $r < 1'$ ) of HCG 62 with ACIS-S3 in 0.5–4 keV. . . . .	65
5.5	Observed and calculated properties of the north and south cavities and the east and west non-cavities. . . . .	69
5.6	Results of spectral fits for the north and south cavity regions and the east and west non-cavity regions within $r \leq 10''$ in 0.5–3 keV with a two temperature vMekal model. . . . .	70
5.7	Results of the projected spectral fit for $r \leq 2'$ region with two temperature vMekal and vAPEC models. . . . .	74
5.8	Same as table 5.7, besides the element abundances are determined separately for the combined fit. . . . .	75
5.9	Fractional contribution of the outer shells to the inner shells in the deprojection analysis. . . . .	76

5.10 Results of the deprojected spectral fit with 1- $T$ and 2- $T$ vMekal models. . . . .	77
B.1 Observation log . . . . .	101

# Acknowledgement

First of all, I am deeply grateful to Prof. T.Ohashi for his continuous support, leading and encouragement throughout the five years of my graduate course. I also appreciate Dr. Y. Ishisaki for his powerful support on technical process, data analysis and experiments. I also express my gratitude to Dr. N. Ota for your useful comments and technical support. I owe the finish in this thesis entirely to them.

I am so much obliged to Prof. N. Y. Yamasaki, Prof. M. Ishida, Prof. K. Masai, and Dr. T. Oshima for valuable comments and discussions.

I wish to thank all members of our laboratory. I particularly appreciate Dr. K. Shinozaki, Dr. A. Hayakawa and Mr. K. Sato for their hearty support and useful comments and discussions on data analysis and experiments. I am also grateful to Mr. T. Inoue, Mr. Y. Yamakawa, Mr. A. Hoshino, Dr. A. Kushino, Dr. T. Furusho, Ms. A. Takashima and Ms. Y. Kawakami.

Finally, I thank my parent and my sister for their hearty support and encouragement.

Part of this work was financially supported by a Research Fellowship for Young Scientists and a Grant-in-Aid for Scientific Research (No. 15·8941) from the Japan Society for the Promotion of Science, and also by Grant-in-Aid of the Ministry of Education, Culture, Sports, Science and Technology (14079103, 16340077).